

University of Alberta

Surface Spectroscopies For Evaluating Protein Binding

By

Francis Nsiah ©

A thesis submitted to the Faculty of Graduate Studies and Research in
partial fulfillment of the requirements for the degree of
Doctor of Philosophy

Department of Chemistry

Edmonton, Alberta

Fall 2007



Library and
Archives Canada

Bibliothèque et
Archives Canada

Published Heritage
Branch

Direction du
Patrimoine de l'édition

395 Wellington Street
Ottawa ON K1A 0N4
Canada

395, rue Wellington
Ottawa ON K1A 0N4
Canada

Your file *Votre référence*
ISBN: 978-0-494-33039-5
Our file *Notre référence*
ISBN: 978-0-494-33039-5

NOTICE:

The author has granted a non-exclusive license allowing Library and Archives Canada to reproduce, publish, archive, preserve, conserve, communicate to the public by telecommunication or on the Internet, loan, distribute and sell theses worldwide, for commercial or non-commercial purposes, in microform, paper, electronic and/or any other formats.

The author retains copyright ownership and moral rights in this thesis. Neither the thesis nor substantial extracts from it may be printed or otherwise reproduced without the author's permission.

AVIS:

L'auteur a accordé une licence non exclusive permettant à la Bibliothèque et Archives Canada de reproduire, publier, archiver, sauvegarder, conserver, transmettre au public par télécommunication ou par l'Internet, prêter, distribuer et vendre des thèses partout dans le monde, à des fins commerciales ou autres, sur support microforme, papier, électronique et/ou autres formats.

L'auteur conserve la propriété du droit d'auteur et des droits moraux qui protègent cette thèse. Ni la thèse ni des extraits substantiels de celle-ci ne doivent être imprimés ou autrement reproduits sans son autorisation.

In compliance with the Canadian Privacy Act some supporting forms may have been removed from this thesis.

Conformément à la loi canadienne sur la protection de la vie privée, quelques formulaires secondaires ont été enlevés de cette thèse.

While these forms may be included in the document page count, their removal does not represent any loss of content from the thesis.

Bien que ces formulaires aient inclus dans la pagination, il n'y aura aucun contenu manquant.


Canada

*“Now unto him that is able to do exceeding abundantly above all that we ask or think, according to the power that worketh in us, Unto him be glory in the church by Christ Jesus throughout all ages, world without end.
Amen.*

Ephesians 3:20,21

DEDICATION

*Dedicated to my wife Comfort...
to my children Samuel and Gloria...
and to my mother for her support and foresight.
Without these dear ones, this accomplishment would
not have been possible.*

ABSTRACT

The extremely small size of nanoscale materials and their tunable physical properties call for the development of novel devices and strategic approaches that make the particles amenable to different surface chemistries. Surface serves as the communication link between the adsorbate and the substrate. Hence, a thorough understanding of the surface chemistries directly interfacing with biological molecules and other adsorbates would provide insight into the fabrication approach as well as the adsorption characteristics of biomolecules adsorbed on the surface. In this thesis, a viable microfluidic patterning of functionalized gold nanoparticles was developed for high-sensitivity detection and reading of protein microarrays. Surface-enhanced Raman spectroscopic (SERS) was employed to read the arrays. The surface enhancement afforded by coupling metal nanoparticles to extrinsic labels was used to generate high-sensitivity detection.

The initial step adopted in this work was to develop skills and techniques for patterning gold nanoparticles that would later serve as a SERS-based sensing platform for biological interactions. Self-assembled monolayers (SAMs) of alkanethiols on gold were used to control surface chemistry. Gold nanoparticles were modified with 4-mercaptobenzoic acid and the functionalized nanoparticles patterned on thiolated planar gold substrate using microfluidic channels created in poly(dimethylsiloxane)

(PDMS). Raman mapping was utilized to provide differences in chemical patterns.

Techniques and protocols developed in Chapter II of this thesis were applied to fabricate protein microarrays for SERS reading based on gold nanoparticle labels. The reagent employed was 30 nm gold nanoparticles modified with a bi-functional Raman reporter molecule, 5,5'-dithiobis(succinimidyl-2-nitrobenzoate) (DSNB), to integrate anti-bovine IgG for antigen response in the immunoassay and generate intense SERS signal. Signal from DSNB reporter molecule, particularly the strong symmetric nitro stretch was used for the detection of antigen-antibody interactions.

Issues related to sensitivity and selectivity of the assay were also addressed. The effects of reporter and nanoparticle surface densities on observed SERS signals were evaluated using mixed SAMs. In addition, quantitative analysis of the immunoassay and multivalency of the binding event were investigated. Finally, it is our hope that work presented in this thesis would provide useful insights into SERS-based immunoassays, and serve as basis for eventful adventure into interfacial biomolecular interactions.

ACKNOWLEDGEMENTS

Everything that has a beginning also has an end. Dear Lord, great is thy faithfulness. I am also greatly indebted to several people who have contributed immensely in diverse ways to my academic career and especially towards the preparation of this thesis.

First of all, I wish to express my sincere appreciation to my M.Sc. and Ph.D. supervisor, Dr. Mark McDermott for his guidance, advice and encouragement. Mark, your noble deeds will forever be remembered in time and in eternity. I remember very well your encouraging words during difficult moments and your insightful discussions. Indeed, you did not only act as a research director but also as a caring and concerned friend. I am indeed grateful to you Mark for your help throughout my stay in your group. It has been an enjoyable experience and a time well spent. In a nutshell, I wish to thank you again for the confidence and trust you have reposed in me and all your help in getting a job. God richly bless you for the good training and exposure to SERS and protein studies.

I also wish to thank all the McDermott group members for their useful suggestions and even discussions outside chemistry. Thank you again for changing my name from Francis to Frank. I would like to also acknowledge the old group members, James, Truong, Gregory, Mirwais, Vishal, Solomon and Bushra. Without your assistance this journey would

not have been possible. Jimmy and Greg, your good advice and assistance will not be forgotten. I must also thank Aaron, Chris, Dwayne Rongbing, Hongmei, Ni, Wendy, Andrew, Lars, Peng and David. Thank you all for the togetherness, informative discussions and the conducive atmosphere you created towards this accomplishment.

Moreover, I am grateful to the Department of Chemistry for their financial support, the Faculty of Graduate Studies and Research and the Natural Science and Engineering Research Council of Canada (NSERC) as well as National Research Council-Genome Health Initiative (NRC-GHI) for funding my research. I am indebted to my PhD. Committee members and my external examiner for their excellent and incisive comments on this thesis. In addition, I thank the entire faculty and the staff in the Chemistry Department especially Ilona, Dr. Cantwell and Dr. Marcus. Thank you very much for your help, encouragement and precious advice.

My very special thank you goes to my dear wife Comfort and my children Samuel and Gloria. Connie, thank you for your patience, special love, and encouraging words offered throughout my studies. Samuel and Gloria, I will forever remember your special welcome and smiles that brought relief after hard day's toil. Thank you and I owe all of you a great deal. I also thank my mum who single handedly sponsored my education. Mum, may God richly reward you for your labour of love. I wish to say a big

thank you to my family in Ghana, my in-laws, and all church members both in Ghana and in Edmonton for their support and prayers.

Finally, I wish to thank all my friends, Pastor Joseph Agyenim Boateng and his family, Brother Peters and his family, Fred, Leonard, Stephen and Yaw Opoku for their support, advice and encouragement. I know my acknowledgement list is incomplete. If I forgot to mention your name, please bear with me and accept my thanks.

TABLE OF CONTENTS

CHAPTER I: INTRODUCTION	PAGE
Surface Based Protein Assays	1
Vibrational Spectroscopy	4
Nanoparticles for Biological Applications	15
SERS-Based Immunoassay Sensing Platforms	19
Research Objectives	25
References	26

CHAPTER II: MICROFLUIDIC PATTERNING OF CHEMICALLY MODIFIED NANOPARTICLES FOR SURFACE ENHANCED RAMAN SPECTROSCOPIC MAPPING

Introduction	33
Experimental	37
Results and Discussion	42
Conclusions	72
References	73

CHAPTER III: NANOPARTICLE-BASED SURFACE ENHANCED RAMAN SPECTROSCOPIC IMAGING OF BIOLOGICAL ARRAYS

Introduction	77
Experimental	81
Results and Discussion	91
Conclusions	114
References	114

CHAPTER IV: CONTROL OF PROTEIN DENSITY ON NANOPARTICLES FOR SERS-BASED IMMUNOASSAYS

Introduction	120
Experimental	123
Results and Discussion	126
Conclusions	151
References	151

CHAPTER V: INVESTIGATION OF ADSORPTION CHARACTERISTICS OF FIBRINOGEN ON MODIFIED GOLD SUBSTRATES USING INFRARED REFLECTION ABSORPTION SPECTROSCOPY

Introduction	154
Experimental	158
Results and Discussion	161
Conclusions	189
References	190

CHAPTER VI: CONCLUSIONS AND FUTURE WORKS

Overall Conclusions	194
Suggestions for Future Work	196
References	198

LIST OF TABLES

Table 3.1	Spectroscopic measurements of the intensities of 1332 cm^{-1} band of DSNB-labeled immunogold nanoparticles on different antigen surface densities	106
Table 4.1	Spectroscopic measurements of the intensities of 1332 cm^{-1} band of serially diluted 100% DSNB-labeled gold nanoparticles with bound antibody	131
Table 4.2	Curve fitting and calculated parameters for anti-bovine IgG bound DSNB-modified nanoparticles with series of solution particle concentrations	135
Table 4.3	Curve fitting and calculated parameters for particle density and 1332 cm^{-1} intensity plots for 100% DSNB	138
Table 4.4	Spectroscopic measurements of the intensities of 1332 cm^{-1} band of serially diluted 50% DSNB-labeled gold nanoparticles with bound antibody	147
Table 4.5	Spectroscopic measurements of the intensities of 1332 cm^{-1} band of serially diluted 50% DSNB-labeled gold nanoparticles with bound antibody	150
Table 5.1	C-H stretching frequencies for UDT, MUA and AUT.	165

Table 5.2	IRRAS measurements of the direct adsorption of 14.7 and 588 nM concentrations of HFG on UDT, MUA and AUT monolayers	170
Table 5.3	Tabulated spectroscopic measurements for evaluation of binding strength of adsorbed 14.7 and 588 nM HFG on MUA substrate	175
Table 5.4	IRRAS measurements of 14.7 and 588 nM concentrations of HFG adsorbed on 14.7 nM pre-HFG film with underlying UDT, MUA and AUT substrates	179
Table 5.5	Curve fitting parameters for HFG on both SAMs and pre-HFG modified gold substrates.	184
Table 5.6	IRRAS measurements of adsorption of HFG, IgG and LYS on AUT patterned substrates	188

LIST OF FIGURES

Figure 1.01	Presentation of protein-protein interaction on a modified solid surface.	2
Figure 1.02	Pictorial representation of Raman vibrational showing individual scattering processes.	7
Figure 1.03	Enzyme immunoassay based on extrinsic SERS method illustrated with peroxidase labeled immunocomplex reaction.	21
Figure 1.04	Silver staining enhancement of Raman molecule labeled immunogold nanoparticle approach for SERS-based immunoassay.	23
Figure 1.05	Extrinsic Raman labeled immunoassay.	24
Figure 2.01	UV-Vis adsorption spectra of unmodified 30 nm gold nanoparticle and 4-MBA modified 30 nm gold nanoparticle (MBANP).	43
Figure 2.02	Raman characterization of MBANP substrate showing powdered, monolayer and SERS spectra of MBA.	45
Figure 2.03	MBANP patterning via microfluidic channels (μ FCs) in PDMS.	48
Figure 2.04	Optical image and SERS spectra of MBANP patterns.	50
Figure 2.05	Illustration of the concept of Raman mapping.	52

Figure 2.06	Demonstration of Raman mapping based on different peaks.	54
Figure 2.07	Raman maps of MBANP patterns on glass and glassy carbon substrates.	57
Figure 2.08	SERS spectra of 4-MBA, NAT and HND patterns on AUT substrate.	58
Figure 2.09	SEM images of 4-MBA, NAT and HND patterns on AUT substrate.	60
Figure 2.10	Multiple color mapping of 4-MBA, NAT and HND patterns and their cross-sectional analysis.	62
Figure 2.11	SERS investigation of MBANP adsorption on UDT, MUA, MUL and AUT modified planar gold substrates.	65
Figure 2.12	SEM micrographs of MBANP adsorption on UDT, MUA, MUL and AUT modified planar gold substrates.	66
Figure 2.13	SERS spectral analysis and intensity plots showing the effect of solution pH on MBANP surface density.	69-70
Figure 3.01	Cartoon representation of DSNB-functionalized nanoparticle-labeled antibody.	84

Figure 3.02	Cartoon representation of interaction of labeled-target with probe molecules.	86
Figure 3.03	Microfluidic patterning of nanoparticle-labeled target.	88
Figure 3.04	SERS analysis revealing the significance of DSNB reporter molecule.	92
Figure 3.05	UV-Vis characterization of nanoparticle labelling procedure.	94
Figure 3.06	Raman spectroscopic stepwise characterization of nanoparticle labelling procedure.	96
Figure 3.07	IRRAS investigation of anti-bovine IgG adsorption to DSNB-modified planar gold substrate.	98
Figure 3.08	Quantitation of the number of antibodies per nanoparticle.	101
Figure 3.09	Spectroscopic reading of protein microarrays.	102
Figure 3.10	Raman map showing intensity variation due to differences in antigen concentration at 1332 cm^{-1} band.	104

Figure 3.11	SERS spectra showing the effect of bovine IgG (blgG) antigen surface concentration.	105
Figure 3.12	SEM investigation of the effect of blgG surface concentration.	108
Figure 3.13	Plots showing variations of antigen concentration and nanoparticle density with the intensity of 1332 cm^{-1} band.	110
Figure 3.14	Demonstration of selectivity in SERS-based immunoassays using blgG and lysozyme.	111
Figure 3.15	Evidence of selectivity in antigen-antibody measurements based on anti-SMA and anti-blgG.	113
Figure 4.01	Surface patterning of different nanoparticle solution concentrations with labeled anti-bovine IgG.	127
Figure 4.02	SERS spectra for varying nanoparticle solution concentrations with 100% DSNB and bound anti-bovine IgG.	129
Figure 4.03	SEM images for nanoparticle surface densities of 10^7 , 10^9 and 10^{11} particles/mL with 100% DSNB and bound anti-bovine IgG.	130
Figure 4.04	Quantitative binding curves showing intensity of the symmetric nitro stretch at 1332 cm^{-1} for 100% DSNB with bound anti-bovine IgG as a function of nanoparticle solution concentration.	134

Figure 4.05	Logarithmic plots of 1332 cm^{-1} band intensity for 100% DSNB-modified antibody and surface particle concentration as a function of nanoparticle concentration.	137
Figure 4.06	Presentations depicting the effects of “hot spot” and multivalent interactions to observed SERS signal.	140
Figure 4.07	SERS spectrum of 4-mercaptophenol (4-MP).	142
Figure 4.08	SERS spectra showing mixed monolayers of 50:50% 4-MP:DSNB and bound anti-bovine IgG modified nanoparticles having different solution concentrations.	144
Figure 4.09	SEM images for nanoparticle surface densities of 10^7 , 10^9 and 10^{11} particles/mL with 50% DSNB and bound anti-bovine IgG.	146
Figure 4.10	Quantitative binding curves showing intensity of the symmetric nitro stretch at 1332 cm^{-1} for 50% DSNB with bound anti-bovine IgG as a function of the logarithm of the nanoparticle solution concentration.	149
Figure 5.01	IRRAS spectrum of polystyrene patterned gold substrates showing characteristic C-H stretching modes for monosubstituted benzene ring and alkyl chain of the polymer.	162
Figure 5.02	FTIR spectra of 1 mM solutions of UDT, MUA and AUT adsorbed gold substrates.	164

Figure 5.03	IRRAS spectra obtained after the 1 h adsorption of 14.7 nM HFG on polystyrene, UDT, MUA and AUT modified planar gold substrates.	168
Figure 5.04	IRRAS spectra obtained after the 1 h adsorption of 588 nM HFG on polystyrene, UDT, MUA and AUT modified planar gold substrates.	169
Figure 5.05	IRRAS investigation of the before and after displacements of 14.7 and 588 nM HFG on MUA derived gold substrates.	174
Figure 5.06	IRRAS spectra obtained after the 1 h adsorption of 588 nM HFG on 14.7 nM pre-HFG substrate initially modified with UDT, MUA and AUT SAMs.	178
Figure 5.07	Binding curves showing HFG coverage on pre-formed HFG substrates initially modified with UDT, MUA and AUT chemistries.	182
Figure 5.08	Binding curves showing direct HFG coverage on gold substrates modified with UDT, MUA and AUT chemistries.	183
Figure 5.09	Evaluation of the influence of adsorbed protein structure on protein coverage using 14.7 and 588 nM solutions of HFG, IgG and LYS on AUT patterned gold substrates.	187

LIST OF SYMBOLS

\AA	A distance unit (angstroms)
A_{aI}	Absorbance value of amide I band
A_{aII}	Absorbance value of amide II band
θ_{a}	Advancing contact angle
Θ	Angle of incidence
K_{ads}	Adsorption coefficient
K_{a}	Association constant
Ψ	Ellipsometric parameter
Δ	Ellipsometric parameter
$I(\nu_L)$	Excitation laser intensity
$A(\nu_L)$	Laser enhancement factor
N	Number of molecules
A_{PAII}	Peak area of amide II band
$\sigma_{\text{free}}^{\text{R}}$	Raman cross-section

$\sigma_{\text{ads}}^{\text{R}}$	Raman cross-section of adsorbed molecules
n	Refractive index
B_{max}	Saturation binding
$A(\nu_{\text{S}})$	Stokes enhancement factor
$I_{\text{RS}}(\nu_{\text{S}})$	Total Stokes intensity
λ	Wavelength
λ_{max}	Maximum wavelength
ν_{a}	Asymmetric C-H stretch
ν_{s}	Symmetric C-H stretch
ν_{al}	Wavenumber (cm^{-1}) of amide I band
ν_{all}	Wavenumber (cm^{-1}) of amide II band

LIST OF ABBREVIATIONS

μ CP	Microcontact printing
μ FC	Microfluidic channel
AFM	Atomic force microscopy
Anti-HFG	Antibody to human fibrinogen
Anti-SMA	Anti-salmonella
AUT	11-Amino-1-undecanethiol
blgG	Bovine immunoglobulin G
BSA	Bovine serum albumin
CCD	Charge coupled device
CD	Circular dichroism
CHEM	Chemical enhancement
DCCD	1,3-Dicyclohexylcarbodiimide
DNA	Deoxyribonucleic acid
DNBA	5,5'-Dithiobis(2-nitrobenzoic acid)
DPN	Dip-pen lithography
DSNB	5,5'-Dithiobis(succinimidyl-2-nitrobenzoate)
DTSP	3,3'-Dithiodipropionic acid di(<i>N</i> -hydroxysuccinimide ester)
EM	Electromagnetic field
EF	Enhancement factor
ELISA	Enzyme linked immunosorbent assay

ERL	Extrinsic Raman label
F _{ab}	Antigen binding fragment
F _c	Crystallizable fragment
FTIR	Fourier transform infrared
FT-SPR	Fourier transform-surface plasmon resonance
GC	Glassy carbon
GLAD	Glancing-angle deposition
HFG	Human fibrinogen
HND	6-Hydroxy-2-naphthyl disulfide
HPNIR	High-performance near-infrared
IgG	Immunoglobulin G
abIgG	Anti-bovine immunoglobulin G
blgG	Bovine immunoglobulin G
IR	Infrared
IRRAS	Infrared reflectance absorbance spectroscopy
LYS	Lysozyme
4-MBA	4-Mercaptobenzoic acid
MCT	Mercury-cadmium-telluride
MHA	Mercaptodecanoic acid
MBANP	4-Mercaptobenzene-functionalized gold nanoparticle
4-MP	4-Mercaptophenol

MUA	11-Mercaptoundecanoic acid
MUL	11-Mercaptoundecanol
MW	Molecular weight
MWCO	Molecular weight cut-off
NAT	2-Naphthalenethiol
NHS	<i>N</i> -hydroxysuccinimide
NIR	Near infrared
NMR	Nuclear magnetic resonance
NP	Nanoparticle
NSL	Nanosphere lithography
PCR	Polymerase chain reaction
PBS	Phosphate buffered saline
PDMS	Poly(dimethyl) siloxane
PEG	Poly(ethylene) glycol
POD	Peroxidase
PS	Polystyrene
PVD	Physical vapour deposition
QD	Quantum dot
RNA	Ribonucleic acid
SAMs	Self-assembled monolayers
SEM	Scanning electron microscopy

SERS	Surface Enhanced Raman Spectroscopy
ssDNA	Single-stranded deoxyribonucleic acid
SP	Surface Plasmon
SPR	Surface plasmon resonance
THF	Tetrahydrofuran
TLC	Thin layer chromatography
TSH	Thyroid stimulating hormone
UDT	1-Undecanethiol
UV-Vis	Ultraviolet-visible

CHAPTER I

INTRODUCTION

Surface Based Protein Assays

Biomolecular interactions and detection at solid surfaces are of fundamental interest in the rapidly growing field of biosensors. The development of surface based protein assay as illustrated in Figure 1.01 begins with the immobilization of a probe molecule (antigen, antibody, or a small molecule) to a pretreated solid surface. A solution containing a target molecule is allowed to interact with the probe molecules leading to the physisorption of the target to the probe molecule. Washing and drying steps are carried to separate the bound antigen-antibody complex from the solution species. Detection of the antigen-antibody interaction is then accomplished using either labeled or non-labeled technique. The work presented in this thesis establishes the development of an alternative sensitive array based detection technique for antigen-antibody interaction. Our approach relies on the use gold nanoparticles as antibody labels and Raman spectroscopy as a readout technique for antibody-antigen interactions.

Surfaces therefore serve as the communication link between protein species interacting either at the macroscopic or microscopic scale. The appreciation of the role surfaces and interfaces in bioreactions facilitates

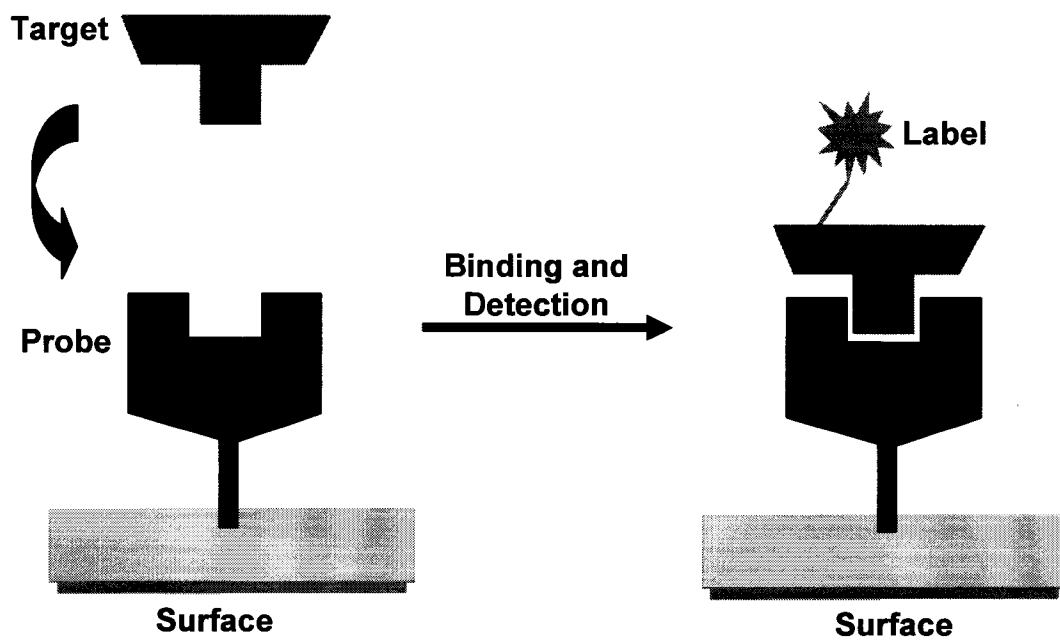


Figure 1.01. Presentation of simple binding and detection of Protein-protein interaction on a modified solid surface.

our understanding of the interfacial behaviour of proteins. For instance, at the molecular scale, an interface might be presented by a protein with a given conformation and/or orientation which regulates its affinity to a binding partner. Figure 1.01 illustrates the interaction and the detection of proteins adsorbed to an interface. Protein adsorption has been found in most cases to be irreversible under physiological conditions.¹ The use of surfaces in protein-protein studies has led to proliferation of detection methodologies and a number of immunoassay sensing platforms.

The commonly used direct, label-free protein detection method for protein detection is the surface plasmon resonance (SPR).²⁻⁴ SPR detects changes in the refractive index upon protein binding to a thin metal film. SPR-based detection shows considerable promise especially in the real-time detection of binding specificity of proteins. The traditional indirect protein detection schemes, on the other hand, employ labeling reagents such as a radioisotope, a fluorescent probe or an enzyme.⁵⁻⁷ The most widely used labeling detection method for protein studies is the enzyme-linked immunosorbent assay (ELISA) technique.⁸⁻¹⁰ ELISA utilizes enzymes as a signal amplifying method. Typically, the procedure involves the capture of a probe analyte into culture wells followed by incubation with an antibody. A secondary antibody tagged with an enzyme is added to each well. The activity of the enzyme is measured by various methods such as colorimetry and fluorometry, depending on the type of enzyme.

SPR and ELISA detection schemes have found widespread application in protein studies. In a quest for alternative technologies that meet the demands of easy and high sensitivity bioanalytical detection, our group and others are investigating the use of noble metal nanoparticles as signal generators of protein binding events. The readout techniques employed for the immunoassays are the vibrational spectroscopic techniques of Raman and IR.

Vibrational Spectroscopy

When a photon of light is incident on matter, it can interact with the atoms or molecules in several ways. It can be absorbed directly or scattered from the sample. These processes can result in the excitation of the vibrational modes of the molecules in the sample. The main spectroscopies employed to detect vibrations in molecules are based on the processes of infrared (IR) absorption and Raman scattering. In IR, the changes in dipole moments are detected whilst Raman spectroscopy measures changes in polarizabilities. Although IR and Raman techniques differ in some respects, yet they provide complementary chemical information about samples. These techniques are used for the identification of substances from their characteristic spectral signatures (fingerprinting). Quantitative and semi-quantitative analysis of the spectral

features can also provide information on the amount of substance in a chemical sample.

Infrared (IR) Spectroscopy. Modern IR spectroscopy is a versatile tool that is applied to the qualitative and quantitative determination of adsorbed protein films. One of the IR techniques that has been widely used in this regard is the infrared reflection absorption spectroscopy (IRRAS).¹¹⁻¹³ IRRAS was first described both theoretically and experimentally in the late fifties.¹⁴ One advantage of IR technique is the ease and rapidity of acquiring high quality spectra from small amounts of proteins. In addition to this, IR provides structural information of proteins in a variety of environments. This makes it a useful probe for protein conformation and orientation changes. Besides, the vibrational characteristics of the peptide backbone (C=O and N-H stretches), conformational structural changes of protein molecules can be monitored by infrared spectroscopy.^{12, 13} A molecule will generally absorb IR radiation if its molecular vibration is associated with a change in dipole moment. In the case of IRRAS, addition to this fundamental selection rule, the molecule must have a component of its dipole moment change normal to the metal in order to be IR active. Hence, IRRAS has the advantage of providing information of the amount of adsorbed protein as well as the geometrical arrangement of the adsorbed protein molecule relative to its metal substrate compared fluorescence-based technique. A sensitive

technique such as fluorescence imaging, besides its requirement of fluorescent label, needs a set of protocols and quantitative analysis of acquired data is not easy. Hence, in this work, we took advantage of capabilities inherent in infrared spectroscopy to monitor protein adsorption on single component monolayer substrates and on bare gold surface.

Raman Spectroscopy. The phenomenon of inelastic light scattering was observed experimentally in 1928 by Sir C. V. Raman and K. S. Krishnan,¹⁵ and is referred to as Raman scattering. The molecular issues underlying Raman scattering are illustrated in Figure 1.02. When monochromatic light of energy $h\nu_0$ considered as a propagating oscillating dipole, passes over a molecule, it can interact and distort the electron cloud around its nuclei. This interaction causes the electrons to polarize and go to a higher energy state. This virtual state is not necessarily a true quantum state of the molecule and it is referred to as a virtual state. The virtual state can be considered a very short lived distortion of the electron cloud caused by the oscillating electric field of the light. At that instant, the energy present in the light is transferred into the molecule leading to an unstable situation and therefore the light is released immediately as scattered radiation.

Two types of scattering are readily identified upon a change in polarizability. The first scattering process is called Raleigh scattering.¹⁶ This is the most intense scattering and it is essentially an elastic process

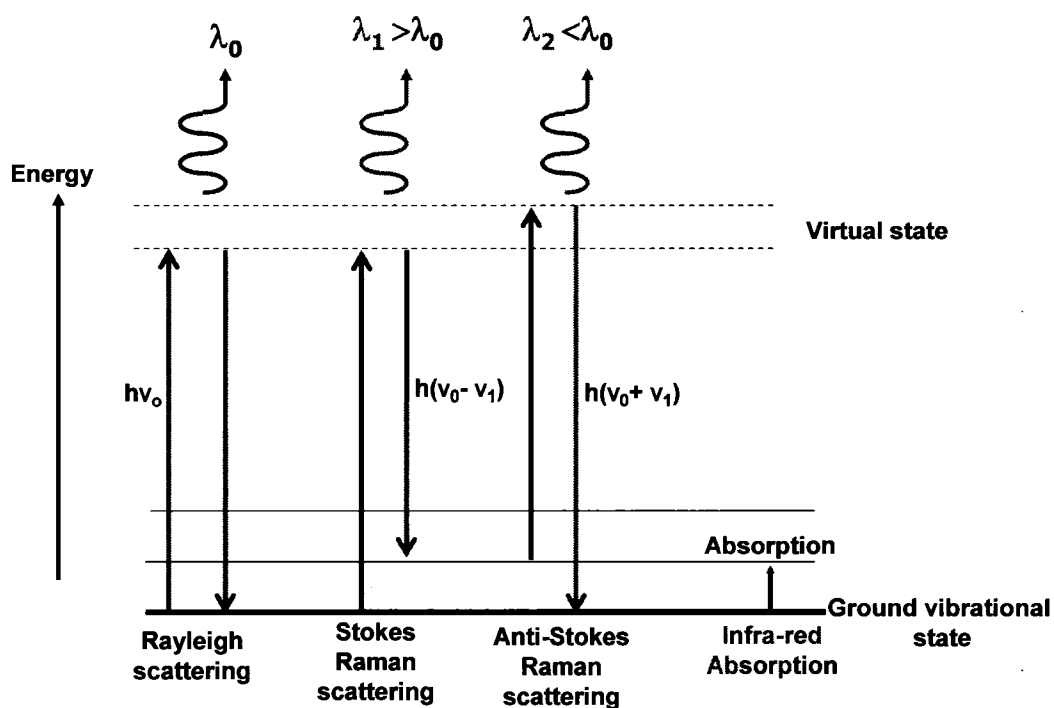


Figure 1.02. Phenomenon of vibrational spectroscopy involving infrared absorption and light scattering processes of Rayleigh and Raman. λ_0 is the wavelength of the incident radiation, λ_1 and λ_2 are corresponding to Stokes and anti-Stokes scattering wavelengths respectively.

(there is no change in energy). Raman scattering, on the other hand, is a much weaker event which involves only one in 10^6 of the scattered radiation. The Raman scattering occurs when a molecule relaxes from the virtual state (described above) to the vibrational states of the ground electronic state. The molecule can relax to either a lower or a higher vibrational state depending on whether the process started with a molecule in the ground state (Stokes scattering) or from a vibrationally excited state (Anti-Stokes scattering). The anti-Stokes intensity is less than the Stokes intensity because the anti-Stokes scattering occurs from an excited vibrational state, which according to Boltzmann distribution, is less populated than the ground vibrational state. Hence, in most cases, the more intense Stokes lines are detected.

The intensity (I) of the Raman scattering is described by Equation 1.1 below:

$$I \propto \nu^4 \sigma(\nu) P_o \exp\left(\frac{-E_1}{kT}\right) \quad (1.1)$$

where ν is the frequency of light, σ is the Raman cross-section of the molecule, P_o is the incident radiant power, E_1 is the energy difference between the ground and excited vibrational states of the molecule, k is the Boltzmann's constant and T is the temperature. In the absence of absorption, the Raman intensity is proportional to the fourth power of the frequency of the source (Equation 1.1). In addition, the intensity is usually

proportional to the concentration of the active species. Hence, Raman spectroscopy resembles fluorescence in which the concentration-intensity has a linear relationship. Raman and its associated techniques have therefore become useful bioanalytical tools.

IR and Raman are complementary vibrational techniques. They are widely used to provide information on chemical structures and physical forms, to identify substances from the characteristic spectral patterns, and to determine quantitatively the amount of a substance in a sample. However, Raman scattering is less widely used than IR absorption largely due to problems with sample degradation and fluorescence. Raman spectroscopy probes vibrational transitions indirectly light scattering. The fundamental difference between IR absorption and Raman scattering is probability, with absorption being a far more likely event. Again, IR requires a dipole moment change for an allowed absorption, while Raman requires a finite polarizability (momentary distortion of the electron cloud around a molecule) change. Thus, it is possible for a vibrational protein band to be IR-active and Raman-inactive. For example, carbonyl groups of the amide linkage in proteins which are both polar and asymmetric will have a dipole moment which will change when the group stretches in a manner analogous to the oxygen atom. They have strong bands in the infrared spectrum but are weaker in the Raman spectrum. Symmetric C=C and S-S bonds, on other hand, are weak infrared absorbers but strong Raman

scatterers. However, recent advances in Raman instrumentation such as low noise multichannel detectors, efficient spectrographs, use of near-infrared (NIR) excitation and fibre optic techniques have provided a strong motivation for its application to protein studies.¹⁶

Development of SERS. About fifty years after the discovery of the Raman effect, the novel phenomenon of a strongly increased Raman signal from pyridine adsorbed on roughened silver electrodes was first reported by Fleischmann et al.^{17, 18} The observed signal enhancement was attributed to increased surface area (that is, an increase in the number of adsorbed molecules contributing to the Raman signal) due to the roughening process. However, in 1977, Van Duyne and Jeanmaire,¹⁹ and Albrecht and Creighton²⁰ independently concluded that the unusually strong Raman signal measured from the adsorbed pyridine cannot be explained simply by an increase in surface area but must be caused by a true enhancement of the Raman scattering efficiency itself. Based on carefully combined experiments and calculations, the major contribution to the intense Raman signal was found to be an enhancement of 10^6 times in the scattering cross-section of the bulk pyridine. This effect was later called surface enhanced Raman spectroscopy (SERS).²¹

Theory of SERS. A lot of studies have been carried out to understand and explain the SERS phenomenon.^{19, 22-33} An overview of theoretical mechanisms stressing classical and chemical origins was

provided by Otto.²⁹⁻³² Metiu and Das,²⁵ Wokaun,²⁶ Efrima,²⁷ Chang and Laube,²⁸ and Moskovits.²⁴ Theories proposed to explain the enhancement phenomenon are currently classified into two different categories, namely the electromagnetic field (EM) enhancement and chemical (CHEM) effect.

It is generally agreed that the SERS enhancement is largely due to the electromagnetic (EM) enhancement.²⁴ Briefly, the EM theory postulates that upon irradiation, the free electrons in a roughened metal or a nanoparticle oscillate with a resonance frequency determined by the dielectric function of the metal. The collective oscillating conduction electrons that propagate parallel to the metal/dielectric interface are called surface plasmons. In this resonance condition, the electric field at the surface is greatly increased. There are many versions of the EM theory with different levels of sophistication. For example, different models have been developed for spheres, interacting spheres, hemispheres and gratings. However, the simplest and widely used model is the isolated spherical particle model.³⁴

The CHEM model, on the other hand, results from the interaction between the surface and the molecule. This results in the formation of a charge-transfer complex or bond formation. The interaction increases the polarizability. The formation of the complex depends on factors such as the adsorption sites, the geometry of bonding and the energy levels of the

adsorbate molecules. CHEM effect is short-range and its contribution to SERS is estimated to be approximately 10^{-3} .³⁵

Biomolecular Application of SERS. SERS holds great possibilities for investigating biological materials from small molecules to tissues. Research efforts in this direction have been towards exploration of SERS application to real-time monitoring and low-level detection of a variety of bioanalytes.^{36, 37} With very narrow spectral bands, low signal strength of water and high sensitivity of SERS, one can obtain spectra of biological molecules at concentrations down to $\sim 10^{-13}$ M.^{37, 38} SERS spectra have been measured for biomolecules such as amino acids and peptides, purine and pyrimidine bases, proteins, DNA and RNA.³⁷⁻⁴¹ Medical applications involving detection of stimulating drugs and selective analysis of antitumor drugs interaction with living cancer cells have also been carried out with SERS.^{42, 43}

Currently, SERS-based detection and characterization of molecules of biomedical interest are carried out in two ways. The first platform involves SERS experiments that attempt to use the intrinsic surface enhanced Raman spectral features of the molecules to directly address their chemical interactions.⁴⁴⁻⁴⁷ These experiments are almost exclusively based on heme proteins such as myoglobin, cytochrome c and hemoglobin. These proteins contain the heme group (iron protoporphyrin) as the active site of their biological functions. Porphyrin rings of the

molecules produce strong resonance enhancement when the laser wavelength is chosen to coincide with the π - π^* transitions of the porphyrin rings. Limited set of proteins that contain porphyrin will give good Resonance SERS. However, there are some difficulties in direct SERS application to biomolecule detection especially at relatively low concentrations. In addition, because biomolecules are built from a limited set of building blocks, they tend to have complex spectra with a lot of overlap due to their structural similarities.

The second approach utilizes the extrinsic SERS labeling so as to circumvent problems associated with the direct SERS-based detection of biologically relevant targets.^{37, 39, 40, 48-53} The idea is to indirectly detect the presence of interaction of a complex and/or weak scattering molecule by labeling the molecule with a small molecule with high intensity, well defined and characteristic Raman spectral features (called Raman reporter molecule). For example, Mirkin and co-workers have used ssDNA coupled to gold nanoparticle and a SERS label to detect DNA hybridization events. With their proposed technique, they were able to use multiplexed detection to distinguish hepatitis A, hepatitis B, HIV, Ebola, smallpox and anthrax with a detection limit of 20 fM.³⁷ Vo-Dinh et al. have also used Raman labels to identify cancer genes.⁵³ In this work, Raman labeled DNA species were prepared and incubated with capture-probe modified substrate. The labeled probes containing a sequence complementary to the capture probe

were successfully hybridized and resulted in a large SERS signal. Other SERS labels such as self-assembled monolayer thiol functionalized silver and gold nanoparticles have been extensively used in several bioanalytical studies in the literature.^{46, 51, 54-56}

SERS-Active Substrates for Bioanalysis. Application of SERS in bioanalysis requires the development of SERS-active substrates that provide reproducible and large enhancement factors that are compatible to biological environments. The choice and fabrication of SERS substrate is therefore the most critical aspect in performing a SERS experiment. Surface features such as size, shape, dielectric environment and interparticle distance greatly impact the localized surface plasmons and the SERS signal intensities. Traditionally, SERS has been performed on silver, gold and copper substrates because these noble metals provide the desired optical properties for the observation of the SERS phenomenon. Electrodes made of transition metals such as bare platinum, ruthenium, rhodium, palladium, iron, cobalt and nickel have also been investigated as SERS substrates.⁵⁷⁻⁵⁹ These transition metals have been found to exhibit enhancement factors ranging from 1 to 4 orders of magnitude depending on the nature of the metal and the surface morphology. Recently, Brolo et al. introduced a simple way to prepare SERS-active substrate by performing a series of scratches in a 100 nm thick gold film deposited on glass. The observed SERS intensity from their substrates is polarization

dependent, with maximum enhancement occurring when the electric vector of the incident field is perpendicular to the direction of the scratches.⁶⁰

Silver and gold have been prepared in different ways to generate SERS-active substrates for a number of biological applications. The most common SERS substrates used include roughened silver electrodes,^{17, 19} island films,⁶¹⁻⁶³ surface-confined nanostructures⁶⁴ and colloidal nanoparticles in solution, the dry on a surface or self-assembled into polymer-coated substrates.^{51, 54, 65-67} Van Duyne and co-workers have fabricated surface-confined structures using electron-beam lithography, colloid immobilization and soft lithography for glucose sensing and other biomolecular applications.^{52, 68} Recently, the SERS behavior of glycine on silver and gold nanoparticles, and particularly the nature of the interaction between amino acids and SERS nanoparticle substrates have been studied.⁶⁹ There is on-going research work to develop novel SERS substrates to prolong lifetime, provide stable and optimized enhancement factors, and allow biological studies in different media.

Nanoparticles for Biological Applications

Advances in research areas such as chemical sensing, biomedical imaging, high-throughput screening analysis and nanoscale photonics have sparked a resurgence of interest in metal and semiconducting nanoparticles in recent times.⁷⁰ Notable among these materials that have

enjoyed widespread applications in biomaterials are the metal nanoparticles and quantum dots (QDs) whose properties are size-dependent. The studies of these nanometer scale (1-100 nm) materials incorporate properties of atoms or molecules whose properties are neither those of the individual constituents nor those of the bulk.

Quantum Dots (QDs). Quantum dots, a special class of semiconductor nanoparticles, have opened up a plethora of possibilities in biological detection and imaging due to their small size, stable luminescence and resistance to photobleaching.^{71, 72} Hundreds of different colors are possible from QDs generated from the same material with the same synthesis protocols. For example, small cadmium selenide (CdSe) dots emit blue light, whereas larger ones can emit green, yellow, or red light across the visible region. Another striking feature of QDs are that all of its colors can be seen simultaneously with a fluorescent microscope. This makes QDs useful for multiplexing in both imaging applications and *in vitro* assays. In order to make QDs biocompatible, several strategies have been devised which involving coating the QDs with amphiphilic phospholipids⁷³ and specialized polymers,⁷⁴ or performing a capping ligand exchange with thiol-containing organic acids.^{75, 76} QDs which have been modified by covalent and electrostatic attachment of antibodies, proteins and peptides for specific applications have also been reported.⁷⁵⁻⁷⁷ However, these modification schemes tend to result in a large sphere

which limit their biological applications. Moreover, fabrication of QDs is not trivial and it is very difficult to precisely control their surface compositions. In addition, cadmium, one of the most commonly used core components, is a heavy metal toxin. Some researchers resorted to the use of alternative material particularly gold nanoparticles for biological applications with the aim of addressing the size, surface chemistry and toxicity issues associated with QDs.

Gold Nanoparticles. Metal nanoparticles (especially silver, gold and copper) play a special role in surface-enhanced spectroscopies because they exhibit strong enhancement and are relatively easy to prepare by using chemical reduction methods. They also provide the possibility to study fundamental optical properties of small conducting particles. One and a half century ago, Faraday proposed that colors exhibited by silver and gold nanoparticles in solution might be due to the various subdivisions of the metal particles comprising these nanoparticles.⁷⁸

Gold nanoparticles have been widely used for a number of biological studies. Features such as ease of preparation, inertness, compatibility with biomolecules and high affinity for thiol binding make them attractive for bioanalytical applications. Gold is also exceptionally easy to pattern by a combination of lithographic tools and chemical etchants. Besides their use as enhancing SERS substrates, aggregated gold nanoparticles have strong tunable near-IR (NIR) adsorption. NIR excitation radiation is

particularly ideal for biological studies because it allows greater penetration depths in tissues while causing less fluorescence background relative to visible radiation. Kneipp et al. have observed extremely large enhancement factors (up to 10^{14}) for dyes adsorbed on gold nanoparticles with NIR excitation.^{79, 80} Surface-modified gold nanoparticles have recently been developed to function as analytical reagents in ultrasensitive bioassays based on SERS.^{49, 51, 81} Some of the chemical modification schemes that have been used to impart detection selectivity of modified gold nanoparticles as SERS substrates include organic polymer layers, SAM coatings,^{51, 81} ultra-thin metal films or monolayers of bioreceptors.³⁹ Different sizes of sequentially labeled gold nanoparticles and their impact on SERS signal from bioassays have also been investigated by Porter and co-workers.⁸² They observed red shifts for gold nanoparticles with increasing particle size. More importantly, greater red shifts and higher enhancement factors (EFs) were obtained for gold nanoparticles tethered to a gold substrate than on a silver substrate. The high red shifts and the concomitant increase in EFs on gold substrates were attributed to the existence of a strong coupling interaction between the nanoparticles and underlying gold substrate.⁸² This study proposed that SERS intensity from SERS-active modified gold nanoparticle substrates can be optimized simply by varying the nanoparticle size, particle-substrate separation and

substrate material which are necessary for the design of SERS-based immunoassay.

SERS Based Immunoassay Sensing Platforms

An immunoassay is based on a specific interaction between an antigen and a complementary antibody, and it is a powerful analytical tool for development of biosensors,⁵ clinical diagnosis,⁸³ environmental analysis⁸⁴ and food industry.⁸⁵ By far the most common antibody employed in immunoassays is the immunoglobulin G (IgG). IgG molecule has a Y-shaped structure consisting of two identical heavy and two identical light polypeptide chains with molecular weight of 150 kD. Proteolytic cleavage of IgG molecule yields two antigen binding fragments (F_{ab}) and one crystallizable fragment (F_c). Each Fab fragment has six loops (complementarity determining regions) which present a potential binding surface for the antigenic epitopes. Numerous hydrogen bonds, electrostatic interactions, and van der Waals interactions, reinforced by hydrophobic interactions, combine to give specific and strong binding of antigen to an antibody.

In recent times, SERS-based immunoassays are gaining popularity due to the characteristic narrower SERS bands which potentially reduce spectral overlaps associated with fluorescence methods. In addition, Raman responses are much less susceptible to photobleaching than

fluorescence, enabling the use of extended signal averaging to lower detection limits.⁸¹

Commonly reported SERS-based immunoassays use indirect methods for the detection of antigen-antibody binding events. The first application of SERS to immunoassays was reported by Rohr et al.⁵⁶ In their approach, a resonance dye, *p*-dimethylaminoazobenzene, was covalently attached to an antibody directed against human thyroid stimulating hormone (TSH), and the resultant conjugate was used as the reported molecule in a sandwich immunoassay for the TSH antigen. Silver film was used as the SERS substrate in their experiment. The intensity of the resultant SERS signal showed a good correlation with TSH antigen concentration over a range of 4 to 60 x 10⁻⁶ mg/mL.⁵⁶ A similar approach was adopted by Dou et al. who developed a new indirect SERS-based enzyme immunoassay illustrated in Figure 1.03.⁴⁹ As shown in Figure 1.03, an antibody bound to a solid support reacts with an antigen, which binds to a secondary antibody labeled with peroxidase (POD). When the immunocomplex undergoes a reaction with *o*-phenylenediamine in the presence of hydrogen peroxide, azoaniline is produced. SERS signals from azoaniline adsorbed on the silver nanoparticle are measured to estimate the concentration of the antigen (mouse IgG). The Raman reporter in this system is a simple and stable dye that shows very strong Raman bands owing to the N=N and C=C stretching modes. The authors

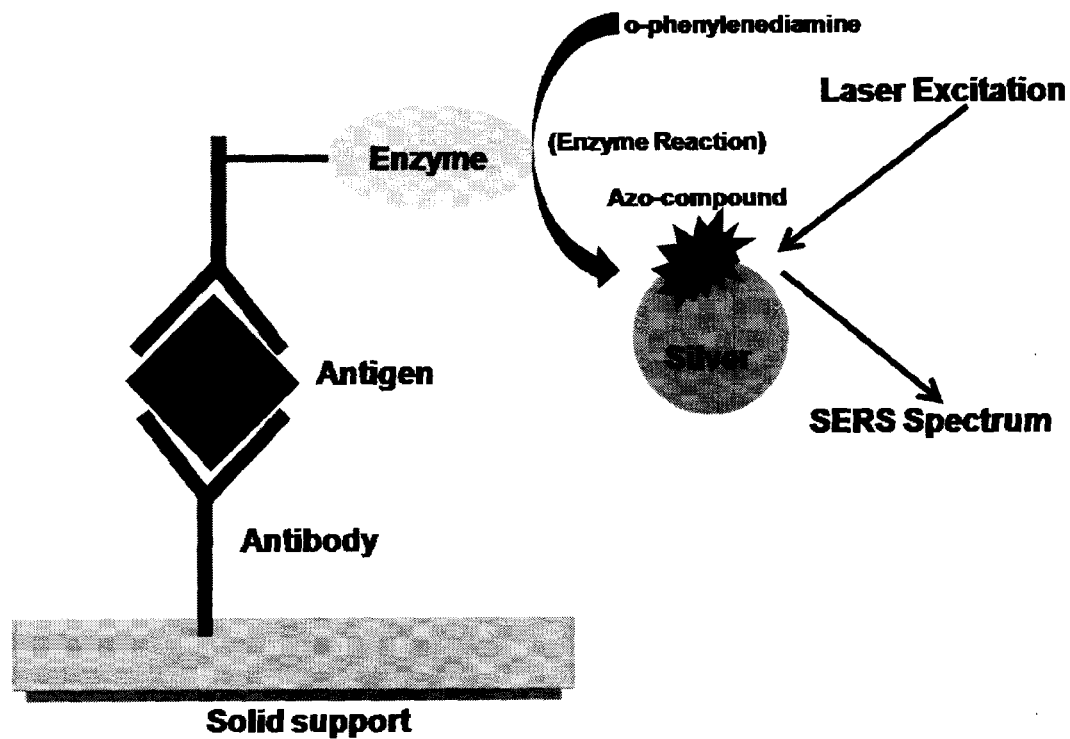


Figure 1.03. Enzyme immunoassay based on extrinsic SERS method. Peroxidase labeled immunocomplex reacts with *o*-phenylenediamine and hydrogen peroxide to azoaniline (Raman-active species).

obtained extremely high selectivity since only the azo compound yielded SERS signal. The detection limit of their system was about 10^{-7} mg/mL. It should be noted here that the sensitivity of the method is not related to the Raman scattering intensity of the label directly attached to the antibody. Hence this approach is often referred to as indirect SERS method.

Another elegant SERS immunoassay based on immunogold labeling with silver staining enhancement has been proposed by Xu et al.⁸⁶ Their indirect SERS method utilizes immunoreactions between immunogold nanoparticles labeled with 4-mercaptobenzoic acid (4-MBA) and immobilized antigens. SERS signals from the Raman-active molecule (4-MBA) were used for the detection of the antigen-antibody interaction in the sandwich immunoassay (Figure 1.04). First, polyclonal mouse antibody against Hepatitis B virus surface antigen was immobilized on a solid support and allowed to interact with the complementary antigen molecules. Gold nanoparticles modified with both 4-MBA and monoclonal mouse antibody were then added to the bound antigen. After silver enhancement, the antigen binding was identified via the SERS spectrum of the 4-MBA. The detection limit for this system was 5×10^{-4} mg/mL which was lower than those previously reported.^{39, 49}

An alternative, extremely sensitive detection method has been introduced by Porter and co-workers.^{51, 55, 81, 87, 88} Their immunoassay (Figure 1.05) relies on the use of gold nanoparticles as the SERS-active

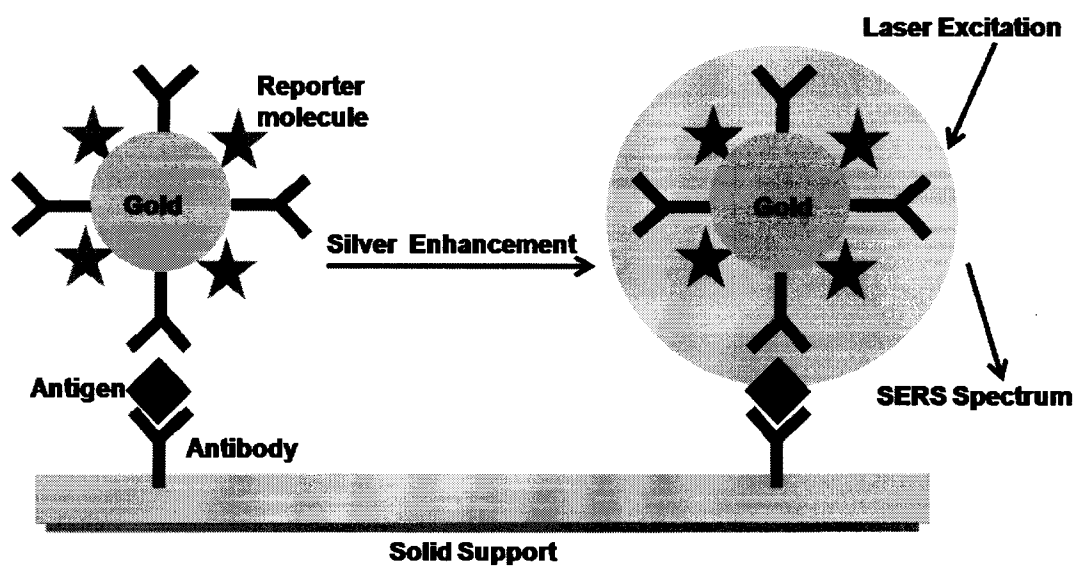


Figure 1.04. Silver staining enhancement of a Raman molecule labeled immunogold nanoparticle approach for SERS-based immunoassay.

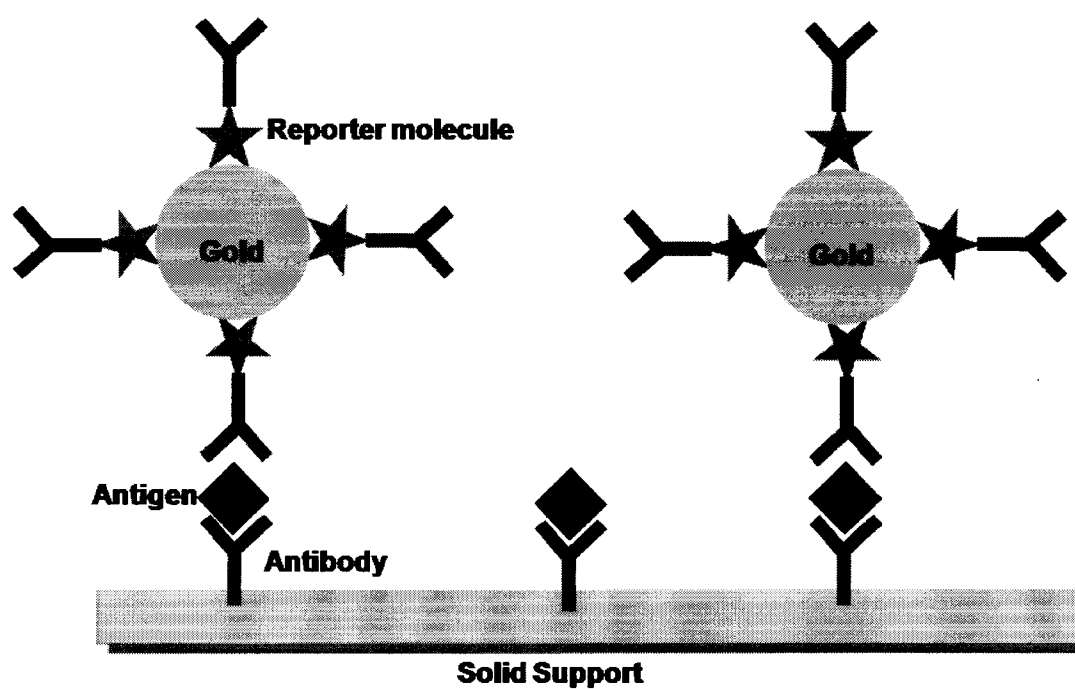


Figure 1.05. Extrinsic Raman labeled immunoassay. Antibody is covalently coupled to the nanoparticle via the reporter molecule. The SERS signal of reporter molecule was used as a measure of antigen-antibody binding.

substrate. Gold nanoparticles are labeled with both bifunctional organic Raman-active molecules often referred to as extrinsic Raman labels (ERLs) and antibodies. By labeling gold nanoparticles with different combinations of ERLs and antibodies, Ni et al. reported simultaneous detection of rabbit and rat IgG molecules.⁵¹ Later, using a different design of Raman labeled immunogold nanoparticles, femtomolar detection of free-prostate specific antigen⁸¹ and low-level detection of virus were reported.⁸⁷ In summary, with SERS' excellent features such as photostability and narrow spectral bands, SERS has a bright future as a bioanalytical tool for trace biomolecular analysis.

Research Objectives

The overall objective of the research presented herein is the development of a nanoparticle labeling system for high sensitive SERS detection of antibody-antigen interactions in an array format. To achieve this goal, the following tasks were completed. The first task involved the optimization of the surface chemistry for probing protein (antigen) immobilization (Chapter V). Gold surfaces tailored to exhibit specific chemistries were prepared from alkylthiols. The amine-thiolated gold surface which presented an ideal substrate for protein studies was chosen for array patterning.

Secondly, protein patterning techniques based on microfluidic network will be developed. These techniques will be employed for initial patterning gold nanoparticles which have been modified with extrinsic Raman labels (Chapter II). The modified nanoparticle patterns will be characterized and the average signal intensity measurements obtained using SERS. SEM is used to obtain nanoparticle surface densities for each pattern.

Thirdly, skills developed in Chapter II were utilized to develop procedures to modify gold nanoparticles with extrinsic labels and antibodies. The protein arrays are characterized and quantitative analysis of the amount of antibodies on nanoparticles is carried out as will be presented in Chapter III. Raman spectroscopy and Raman mapping will be used for detection of the antigen-antibody interactions and as the array readout scheme respectively (Chapters III and IV).

The final task is the evaluation of the system to enable quantitative binding studies. The effect of the extrinsic Raman label solution composition on the protein coverage was studied (Chapter IV).

References

- (1) Brash, J. L. *Current Opinion in Colloid & Interface Science* **1996**, *1*, 682-688.
- (2) Mullett, W. M.; Lai, E. P. C.; Yeung, J. M. *Methods* **2000**, *22*, 77-91.

- (3) Kanda, V.; Kariuki, J. K.; Harrison, D. J.; McDermott, M. T. *Analytical Chemistry* **2004**, *76*, 7257-7262.
- (4) Tian, Y.; Chen, Y. H.; Song, D. Q.; Liu, X.; Bi, S. Y.; Zhou, X.; Cao, Y. B.; Zhang, H. Q. *Analytica Chimica Acta* **2005**, *551*, 98-104.
- (5) Morgan, C. L.; Newman, D. J.; Price, C. P. *Clinical Chemistry* **1996**, *42*, 193-209.
- (6) Skladal, P. *Electroanalysis* **1997**, *9*, 737-745.
- (7) Skladal, P.; Macholan, L. *Chemicke Listy* **1997**, *91*, 105-113.
- (8) Arkel, Y. S.; Ku, D. H. W.; Le, P.; Carr, A. M. *Thrombosis and Haemostasis* **2001**, *86*, 1127-1128.
- (9) Ferrin, N. H.; Fang, Y.; Johnson, C. R.; Murtaugh, M. P.; Polson, D. D.; Torremorell, M.; Gramer, M. L.; Nelson, E. A. *Clinical and Diagnostic Laboratory Immunology* **2004**, *11*, 503-514.
- (10) McKenna, S. L. B.; Keefe, G. P.; Barkema, H. W.; Sockett, D. C. *Veterinary Microbiology* **2005**, *110*, 105-111.
- (11) Liedberg, B.; Ivarsson, B.; Lundstrom, I. *Journal of Biochemical and Biophysical Methods* **1984**, *9*, 233-243.
- (12) Liedberg, B.; Ivarsson, B.; Lundstrom, I.; Salaneck, W. R. *Progress in Colloid and Polymer Science* **1985**, *70*, 67-75.
- (13) Ta, T. C.; McDermott, M. T. *Analytical Chemistry* **2000**, *72*, 2627-2634.
- (14) Francis, S. A.; Ellison, A. H. *Journal of the Optical Society of America* **1959**, *49*, 131-138.
- (15) Raman, C. V.; Krishnan, K. S. *Nature* **1928**, *121*, 501-502.
- (16) McCreery, R. L. *Raman Spectroscopy for Chemical Analysis*; John Wiley & Sons, Inc.: Toronto, 2000.
- (17) Fleischmann, M.; Hendra, P. J.; McQuilla, A. J. *Journal of the Chemical Society-Chemical Communications* **1973**, 80-81.

- (18) Fleischmann, M.; Hendra, P. J.; McQuilla, A. J. *Chemical Physics Letters* **1974**, *26*, 163-166.
- (19) Jeanmaire, D. L.; Van Duyne, R. P. *Journal of Electroanalytical Chemistry* **1977**, *84*, 1-20.
- (20) Albrecht, M. G.; Creighton, J. A. *Journal of the American Chemical Society* **1977**, *99*, 5215-5217.
- (21) Van Duyne, R. P. *Laser Excitation of Raman Scattering from Adsorbed Molecules on Electrode Surfaces*; Academic Press: New York, 1979.
- (22) Xu, H. X.; Aizpurua, J.; Kall, M.; Apell, P. *Physical Review E* **2000**, *62*, 4318-4324.
- (23) Xu, H. X.; Kall, M. *ChemPhysChem* **2003**, *4*, 1001-1005.
- (24) Moskovits, M. *Reviews of Modern Physics* **1985**, *57*, 783-826.
- (25) Metiu, H.; Das, P. *Annual Review of Physical Chemistry* **1984**, *35*, 507-536.
- (26) Wokaun, A. *Solid State Physics-Advances in Research and Applications* **1984**, *38*, 223-294.
- (27) Efrima, S. *Journal of Physical Chemistry* **1985**, *89*, 2843-2849.
- (28) Chang, R. K.; Laube, B. L. *Critical Reviews in Solid State and Materials Sciences* **1984**, *12*, 1-73.
- (29) Otto, A. *Applied Surface Science* **1980**, *6*, 309-355.
- (30) Otto, A. *Bulletin of the American Physical Society* **1981**, *26*, 198-198.
- (31) Otto, A. *Surface Science* **1982**, *117*, 330-330.
- (32) Otto, A. *Topics in Applied Physics* **1984**, *54*, 289-418.
- (33) Wang, D. S.; Kerker, M. *Physical Review B* **1981**, *24*, 1777-1790.
- (34) Wang, D. S.; Chew, H.; Kerker, M. *Applied Optics* **1980**, *19*, 2256-2257.

- (35) Otto, A.; Mrozek, I.; Grabhorn, H.; Akemann, W. *Journal of Physics-Condensed Matter* **1992**, *4*, 1143-1212.
- (36) Kneipp, K.; Haka, A. S.; Kneipp, H.; Badizadegan, K.; Yoshizawa, N.; Boone, C.; Shafer-Peltier, K. E.; Motz, J. T.; Dasari, R. R.; Feld, M. S. *Applied Spectroscopy* **2002**, *56*, 150-154.
- (37) Cao, Y. W. C.; Jin, R. C.; Mirkin, C. A. *Science* **2002**, *297*, 1536-1540.
- (38) Nabiev, I. R.; Savchenko, V. A.; Efremov, E. S. *Journal of Raman Spectroscopy* **1983**, *14*, 375-379.
- (39) Dou, X.; Yamaguchi, Y.; Yamamoto, H.; Doi, S.; Ozaki, Y. *Journal of Raman Spectroscopy* **1998**, *29*, 739-742.
- (40) Dou, X. M.; Jung, Y. M.; Cao, Z. Q.; Ozaki, Y. *Applied Spectroscopy* **1999**, *53*, 1440-1447.
- (41) Kneipp, K.; Pohle, W.; Fabian, H. *Journal of Molecular Structure* **1991**, *244*, 183-192.
- (42) Chourpa, I.; Morjani, H.; Riou, J. F.; Manfait, M. *Febs Letters* **1996**, *397*, 61-64.
- (43) Nabiev, I.; Chourpa, I.; Manfait, M. *Journal of Physical Chemistry* **1994**, *98*, 1344-1350.
- (44) Cotton, T. M.; Kim, J. H.; Chumanov, G. D. *Journal of Raman Spectroscopy* **1991**, *22*, 729-742.
- (45) Nabiev, I.; Chourpa, I.; Manfait, M. *Journal of Raman Spectroscopy* **1994**, *25*, 13-23.
- (46) Petry, R.; Schmitt, M.; Popp, J. *ChemPhysChem* **2003**, *4*, 14-30.
- (47) Hu, S. Z.; Yu, A. E.; Burstyn, J. N.; Spiro, T. G. *Biophysical Journal* **1994**, *66*, 11-18.
- (48) Cao, Y. C.; Jin, R. C.; Nam, J. M.; Thaxton, C. S.; Mirkin, C. A. *Journal of the American Chemical Society* **2003**, *125*, 14676-14677.

- (49) Dou, X.; Takama, T.; Yamaguchi, Y.; Yamamoto, H.; Ozaki, Y. *Analytical Chemistry* **1997**, *69*, 1492-1495.
- (50) Graham, D.; Mallinder, B. J.; Smith, W. E. *Biopolymers* **2000**, *57*, 85-91.
- (51) Ni, J.; Lipert, R. J.; Dawson, G. B.; Porter, M. D. *Analytical Chemistry* **1999**, *71*, 4903-4908.
- (52) Haes, A. J.; Stuart, D. A.; Nie, S. M.; Van Duyne, R. P. *Journal of Fluorescence* **2004**, *14*, 355-367.
- (53) Vo-Dinh, T.; Allain, L. R.; Stokes, D. L. *Journal of Raman Spectroscopy* **2002**, *33*, 511-516.
- (54) Mirkin, C. A.; Letsinger, R. L.; Mucic, R. C.; Storhoff, J. J. *Nature* **1996**, *382*, 607-609.
- (55) Park, H. Y.; Driskell, J. D.; Kwarta, K. M.; Lipert, R. J.; Porter, M. D.; Schoen, C.; Neill, J. D.; Ridpath, J. F. *Surface-Enhanced Raman Scattering: Physics and Applications* **2006**, *103*, 427-446.
- (56) Rohr, T. E.; Cotton, T.; Fan, N.; Tarcha, P. J. *Analytical Biochemistry* **1989**, *182*, 388-398.
- (57) Ren, B.; Lin, X. F.; Yang, Z. L.; Liu, G. K.; Aroca, R. F.; Mao, B. W.; Tian, Z. Q. *Journal of the American Chemical Society* **2003**, *125*, 9598-9599.
- (58) Tian, Z. Q.; Ren, B.; Wu, D. Y. *Journal of Physical Chemistry B* **2002**, *106*, 9463-9483.
- (59) Yang, Z. L.; Wu, D. Y.; Yao, J. L.; Hu, J. Q.; Ren, B.; Zhou, H. G.; Tian, Z. Q. *Chinese Science Bulletin* **2002**, *47*, 1983-1986.
- (60) Brolo, A. G.; Addison, C. J. *Journal of Raman Spectroscopy* **2005**, *36*, 629-634.
- (61) Ni, F.; Sheng, R. S.; Cotton, T. M. *Analytical Chemistry* **1990**, *62*, 1958-1963.
- (62) Van Duyne, R. P.; Hulteen, J. C.; Treichel, D. A. *Journal of Chemical Physics* **1993**, *99*, 2101-2115.

- (63) Stockle, R. M.; Deckert, V.; Fokas, C.; Zeisel, D.; Zenobi, R. *Vibrational Spectroscopy* **2000**, *22*, 39-48.
- (64) Hulteen, J. C.; Van Duyne, R. P. *Journal of Vacuum Science & Technology A-Vacuum Surfaces and Films* **1995**, *13*, 1553-1558.
- (65) Grabar, K. C.; Allison, K. J.; Baker, B. E.; Bright, R. M.; Brown, K. R.; Freeman, R. G.; Fox, A. P.; Keating, C. D.; Musick, M. D.; Natan, M. J. *Langmuir* **1996**, *12*, 2353-2361.
- (66) Alivisatos, A. P.; Johnsson, K. P.; Peng, X. G.; Wilson, T. E.; Loweth, C. J.; Bruchez, M. P.; Schultz, P. G. *Nature* **1996**, *382*, 609-611.
- (67) Emory, S. R.; Nie, S. M. *Analytical Chemistry* **1997**, *69*, 2631-2635.
- (68) Yonzon, C. R.; Haynes, C. L.; Zhang, X. Y.; Walsh, J. T.; Van Duyne, R. P. *Analytical Chemistry* **2004**, *76*, 78-85.
- (69) Yang, J. H.; Lu, L. H.; Wang, H. S.; Shi, W. D.; Zhang, H. J. *Crystal Growth & Design* **2006**, *6*, 2155-2158.
- (70) Burda, C.; Chen, X. B.; Narayanan, R.; El-Sayed, M. A. *Chemical Reviews* **2005**, *105*, 1025-1102.
- (71) Alivisatos, A. P. *Science* **1996**, *271*, 933-937.
- (72) Alivisatos, P. *Nature Biotechnology* **2004**, *22*, 47-52.
- (73) Dubertret, B.; Skourides, P.; Norris, D. J.; Noireaux, V.; Brivanlou, A. H.; Libchaber, A. *Science* **2002**, *298*, 1759-1762.
- (74) Wu, X. Y.; Liu, H. J.; Liu, J. Q.; Haley, K. N.; Treadway, J. A.; Larson, J. P.; Ge, N. F.; Peale, F.; Bruchez, M. P. *Nature Biotechnology* **2003**, *21*, 41-46.
- (75) Chan, W. C. W.; Nie, S. M. *Science* **1998**, *281*, 2016-2018.
- (76) Mattoussi, H.; Mauro, J. M.; Goldman, E. R.; Anderson, G. P.; Sundar, V. C.; Mikulec, F. V.; Bawendi, M. G. *Journal of the American Chemical Society* **2000**, *122*, 12142-12150.

- (77) Sukhanova, A.; Dewy, M.; Venteo, L.; Kaplan, H.; Artemyev, M.; Oleinikov, V.; Klinov, D.; Pluot, M.; Cohen, J. H. M.; Nabiev, I. *Analytical Biochemistry* **2004**, *324*, 60-67.
- (78) Faraday, M. *Phil. Trans.* **1857**, *147*, 147.
- (79) Kneipp, K.; Kneipp, H.; Deinum, G.; Itzkan, I.; Dasari, R. R.; Feld, M. S. *Applied Spectroscopy* **1998**, *52*, 175-178.
- (80) Kneipp, K.; Kneipp, H.; Manoharan, R.; Hanlon, E. B.; Itzkan, I.; Dasari, R. R.; Feld, M. S. *Applied Spectroscopy* **1998**, *52*, 1493-1497.
- (81) Grubisha, D. S.; Lipert, R. J.; Park, H. Y.; Driskell, J.; Porter, M. D. *Analytical Chemistry* **2003**, *75*, 5936-5943.
- (82) Driskell, J. D.; Lipert, R. J.; Porter, M. D. *Journal of Physical Chemistry B* **2006**, *110*, 17444-17451.
- (83) Tsikas, D. *Clinica Chimica Acta* **2004**, *344*, 215-217.
- (84) Lee, J. K.; Ahn, K. C.; Stoutamire, D. W.; Gee, S. J.; Hammock, B. D. *Journal of Agricultural and Food Chemistry* **2003**, *51*, 3695-3703.
- (85) Anand, A.; Moreira, R.; Henry, J.; Chowdhury, M.; Cote, G.; Good, T. *Lwt-Food Science and Technology* **2005**, *38*, 849-858.
- (86) Xu, S. P.; Ji, X. H.; Xu, W. Q.; Li, X. L.; Wang, L. Y.; Bai, Y. B.; Zhao, B.; Ozaki, Y. *Analyst* **2004**, *129*, 63-68.
- (87) Driskell, J. D.; Kwarta, K. M.; Lipert, R. J.; Porter, M. D.; Neill, J. D.; Ridpath, J. F. *Analytical Chemistry* **2005**, *77*, 6147-6154.
- (88) Driskell, J. D.; Kwarta, K. M.; Lipert, R. J.; Vorwald, A.; Neill, J. D.; Ridpath, J. F.; Porter, M. D. *Journal of Virological Methods* **2006**, *138*, 160-169.

CHAPTER II

MICROFLUIDIC PATTERNING OF CHEMICALLY MODIFIED NANOPARTICLES FOR SURFACE ENHANCED RAMAN SPECTROSCOPIC MAPPING

Introduction

This chapter explores the use of microfluidics and interfacial chemistry to chemically pattern 4-mercaptobenzene-functionalized gold nanoparticles (MBANP) onto modified planar gold substrates. The main objective is to utilize nanoparticle labeled systems later in this thesis to measure protein interactions using surface enhanced Raman spectroscopy (SERS). Hence, it is needful to develop a viable patterning procedure and explore the use of SERS for measuring the interactions of modified nanoparticles on surfaces. Efforts will also be directed towards controlling and measuring the interactions within these patterns. The skills and techniques acquired in this study provided us a good background to nanoparticle patterning and sensing platform. It also formed the basis for the bioanalytical studies carried out in the proceeding chapters in this thesis.

Metal nanoparticles have been a focus of intense research in recent times owing to their interesting physical and optical properties which are greatly different from those of their bulk materials.^{1, 2} For example, gold and silver nanoparticles have characteristic red and yellow colours which are quite different from bulk gold and silver. Recent studies have shown that the colours of these noble metal

nanoparticles are due to collective oscillations of the electrons in the conduction band, known as the surface plasmons (SPs).³ The oscillation frequency is usually in the visible region of the electromagnetic spectrum for gold and silver giving rise to the strong surface plasmon adsorption.⁴ Besides, the ability of these metal nanoparticles to efficiently scatter visible light is being vigorously pursued by the scientific research community.^{3, 5, 6} To understand these properties, optical techniques such as surface enhanced Raman spectroscopy (SERS) have proved useful.^{3, 4, 7, 8} SERS phenomenon owes its origin to the enhanced spectroscopic response of molecules bound to or in close proximity to electrochemically roughened metal substrates or surface of metal nanoparticles.⁹

The excitation of SPs by light from surfaces requires optical couplers (prism or grating), a roughened metal surface or a metal nanoparticle.¹⁰ Based on this requirement, a lot of synthetic routes, fabrication and patterning techniques have evolved to develop surface structures and nanoparticles with tunable plasmonic properties particularly for SERS applications.^{1, 2, 4, 7, 10-12} For example, a considerable number of methods such as nanosphere lithography (NSL),⁴ vacuum vapour deposition,¹³ dip-pen nanolithography (DPN)¹⁴ and microcontact printing (μ CP)¹⁵ have been employed to pattern two-dimensional (2D) nanostructures and nanoparticles on surfaces.

In spite of the numerous patterning methodologies being developed for SERS applications, to date no work involving microfluidic devices to pattern 2D nanoparticle arrays is found in the literature. Microfluidic devices utilize very small quantities of samples and reagents to generate well-defined surface patterns. Moreover, microfluidic devices can be fabricated from a wide variety of materials. The most commonly used microfluidic device is poly(dimethylsiloxane) (PDMS). PDMS is a transparent rubber which is relatively inert to a wide range of chemicals. Its surface inertness allows easy transport of relevant chemical and biological species. The simple PDMS microfluidic devices developed by Whitesides' group¹⁶⁻¹⁸ less than a decade ago have now grown into a plethora of advanced structures with micron scale features which has recently been used in SERS applications. Work presented in this thesis, employs microfluidic channels created in PDMS to pattern 2D arrays of gold nanoparticles.

Recent developments in Raman instrumentation have also led to emerging areas such Raman imaging and mapping of surfaces. The Raman mapping technique which arises from the combination of Raman spectroscopy and microscopy has enormous potential in revealing chemical contrast in a wide variety of samples. Raman mapping is of particular interest to a number of applications which include pharmaceuticals^{19,20} and self-assembled monolayers (SAMs) on gold nanoparticles.²¹⁻²³ To generate a map, a sample area of interest is

selected and a step size defined. The step size defines the pixel size. A large number of spectra are then collected from within the defined area. From this data, any characteristic peak within the spectral region is then selected and analyzed to produce a Raman map of the intensity variation (as brightness) for the plotted vibration with each pixel being a point where a spectrum was collected. Areas showing lighter pixel intensity have greater Raman scattering.

With the variety of SERS substrates available today, researchers are able to select SERS substrate architecture to best match their experimental needs. Gold nanoparticle substrates modified with SAMs of alkanethiols have been investigated using SERS^{8, 24-27} due to their ease of preparation, robustness and numerous applications. For example, Johnson *et al.* have shown that the nature of the terminal group of a SAM significantly affects the particle-particle interaction both in solution and in thin films.²⁷ Moreover, Hales' group and others have used 4-mercaptobenzoic acid (4-MBA) SAM for SERS investigations. 4-MBA which functions as a Raman-reporter molecule provides very strong SERS signal and exhibits different adsorption characteristics on different surface chemistries.^{11, 28, 29}

Described herein is a viable and efficient procedure developed to pattern MBANP on SAM modified planar gold substrates. The MBANP patterning procedure employed relies on the use of microfluidic channels created in PDMS. The bifunctionality of the 4-MBA molecule

helps to examine its interaction with different functional groups on the surface. SAMs of alkanethiols on gold substrate with the same chain length but different terminal functionalities (-COOH, -NH₂, -OH, -CH₃) were studied. Raman mapping was used to provide spectral differences in MBANP patterns. Investigations into the effect of surface chemistry and pH on particle density gave insight into the adsorption characteristics of MBANP on different surface chemistries.

Experimental

Reagents and Materials. Gold nanoparticles (30 nm, BBI International, UK) were purchased and used as received. 1-undecanethiol (UDT) 98%, 11-mercapto-1-undecanol (MUL) 97%, 11-mercaptoundecanoic acid (MUA) 95%, 4-mercaptobenzoic acid (4-MBA), 2-naphthalenethiol (NAT) 99% and 6-hydroxy-2-naphthyl disulfide (HND) 98% were purchased from Aldrich (Milwaukee, WI) and used as received. 11-amino-1-undecanethiol (AUT) was purchased from Dojindo Laboratories (Kumamoto, Japan). Millimolar thiol solutions were prepared in anhydrous ethanol (Quantum Chemical Co., Newark, NJ). Buffer solution employed salts from Fisher Scientific Company (Ottawa, ON). Phosphate buffered saline (PBS, pH 7.4) was prepared with reagent grade 1.4 mM KH₂PO₄ and 4.3 mM Na₂PO₄, 137 mM NaCl and 2.7 mM KCl. Glassy carbon plates (10 x 10 cm, 3 mm thick) were obtained from Tokai Carbon Co. Ltd. (Tokai GC-20S, Tokyo, Japan)

and diced into 2.5 x 2.5 cm sizes. GC-20 refers to a pyrolysis temperature of 2000°C. All reagents were used as received.

Substrate Preparation. 0211 glass (Dow Corning, Portsmouth, NH, 18 mm x 18 mm x 1 mm) substrates used were pre-cleaned in piranha solution (1:3 H₂O₂: H₂SO₄) at 90°C for 15 min, rinsed several times with deionized water and dried with argon. A 15 nm adhesive layer of chromium and a 200 nm gold film were prepared by physical vapor deposition (PVD). A thermal evaporation system (Ion International Inc., New Windsor, NY) was used for the deposition of the gold and chromium films on the clean 0211 glass substrates. A vacuum of 4.6×10^{-6} mbar was maintained during evaporation with rates of 0.2 Å/sec for Cr and 0.4 Å/sec for Au. Once prepared, the Au surfaces were rinsed using ethanol and water followed by drying with argon. The substrates were then cleaned in an ozone cleaner (UVO-Cleaner, Model No. 42, Jelight Company Inc., Irvine, CA) for 10 min prior to surface modification.

Fabrication of PDMS Device. Poly(dimethyl)siloxane (PDMS) microfluidic channels were fabricated according to published procedure³⁰. Briefly, a relief pattern of photoresist on a silicon wafer was created using photolithography. PDMS elastomer kit obtained from Dow Corning (Sylgard 184, Dow Corning, Midland, MI) containing polydimethylsiloxane prepolymer and cross-linker (mixed in a 10:1 w/w) was cured by weight against the relief structure and a negative of the

relief was formed in the PDMS. The microchannels measured 200 μm wide and 10 - 15 μm deep. The optimal cleaning procedure for PDMS devices proposed by Graham *et al.*³¹ was used in this study. Briefly, the procedure involved soaking the device in hexanes overnight, air drying followed by three times sonication in a 2:1 ethanol/water mixture.

Preparation of Raman Reporter-Labeled Gold Nanoparticles.

The Raman reporter-labeled gold nanoparticles were prepared following the procedure outlined by Ni *et al.*³² Briefly, the unconjugated gold nanoparticles were labeled with the Raman reporters (4-MBA, NAT and HND) through the spontaneous adsorption of these thiol molecules on to gold. 2.5 μL of 1 mM ethanolic solution of 4-MBA, NAT or HND was added to 1 mL of 2×10^{11} particles/mL unconjugated gold nanoparticle solution and incubated for 1 h. The resultant Raman reporter-labeled gold nanoparticles were then centrifuged at 10000 rpm for 7 min. The nanoparticles were redispersed in 1 mL of deionized water from a Nanopure (Barnstead, Dubuque, IA) purification system and centrifuged again as above to remove unbound species. After this step, the gold nanoparticles were finally redispersed to a final volume of 500 μL with deionized water.

Substrate Modification and Patterning. Surface modification was achieved through self-assembly of UDT, MUL, AUT and MHA. Typically, a planar gold-coated 0211 chip was immersed in a 1 mM ethanolic solution of UDT, AUT or MUL overnight or MUA for 1 h. After the

specified assembly time, the slides were removed from solution and rinsed well with ethanol to remove unbound thiols from the surface, and then dried with a stream of Argon. Arrays of Raman reporter-labeled gold nanoparticles were then patterned on the modified gold substrates having different surface chemistries using microfluidic channels formed in the PDMS. First, a gold substrate was modified with a thiol molecule via chemisorption. A poly(dimethylsiloxane) (PDMS) device with microfluidic channels (μ FC) was placed on the substrate. The use of the PDMS allows for a strong conformal contact between the PDMS and the substrate. 4-MBA-labeled gold nanoparticles were adsorbed on the modified substrate through the μ FCs. Solutions were left in the channels for about 12 h but typically the surface reaction takes 1-2 h to complete.

Effect of Solution pH on 4-MBA-Labeled Gold Nanoparticles (MBANP). Buffer solutions tried in this study included phosphate, acetate, borate and citrate. Acetate, borate and citrate buffer solutions caused the nanoparticles to precipitate out in solution hence these solutions were not employed for the pH studies described in this section. Phosphate-buffered saline (PBS) solutions of pH values ranging from pH 4 to pH 9 taking into account components and ionic strength of each buffer. The range of pH was chosen based on published reports.^{33, 34} However, the gold nanoparticles precipitated in less than 5 min when added to highly acidic (pH 1 to 3) and basic (pH 13 to 14) solutions. To evaluate the pH effect, 200 μ L of MBANP

solutions were added to 800 μL of each buffer solution. The solutions were incubated for 1 h, centrifuged at 10000 rpm for 7 min, rinsed with deionized water and patterned onto AUT-modified gold substrates. After 1-2 h incubation, substrates were rinsed with deionized water, dried under nitrogen and SERS spectra were measured. Several spectra were collected for each pH analyzed.

Instrumentation: (1) *UV-VIS Spectroscopy Measurements.* Absorption spectra were obtained using a PelkinElmer Lambda 35 UV/VIS spectrometer with a 10 mm optical path length.

(2) *Surface-Enhanced Raman Scattering (SERS) Measurements.* SERS spectra were recorded with a Renishaw inVia Raman Microscope equipped with high-performance near-IR (HPNIR) diode (785 nm, 1200 W/mm) lasers, and a CCD detector. Radiation of 785 nm from air-cooled diode laser was used for excitation. Laser power at the sample was 10 mW (measured with power meter). The microscope attachment was based on a Leica system. A 5X objective was used to first focus the laser beam and a 50X objective used to collect spectra and maps. Data for Raman maps were collected over a 1 mm x 1 mm area using a step size of 100 μm controlled by an automated motorized XYZ scanning stage. All reported maps and spectra were the results of 10 s accumulations. Each of the maps required approximately 2 h to collect.

(3) *Scanning Electron Microscopy (SEM) Measurements.* SEM images were collected using a Hitachi S4800 FE-SEM system (Hitachi

Scientific Equipment, Japan) equipped with an ultrahigh resolution, low voltage 10 kV SEM inspection with advanced sample navigation package.

Results and Discussion

Characterization of Nanoparticles. This study employs 4-MBA as a Raman probe molecule. Adsorbing a monolayer of 4-MBA onto gold nanoparticles provides a system for SERS studies. Monolayers of 4-MBA formed by solution self-assembly on gold nanoparticles and planar gold substrate were characterized using UV-Vis and Raman techniques.

UV-Vis Spectroscopy of 4-MBA Modified Nanoparticle. Characteristically, noble metals exhibit a strong absorption band that is not present in the spectrum of bulk metal. This adsorption band results when the incident photon frequency is in resonance with the collective oscillation of the conduction electrons called surface plasmons. A major thrust behind the application of UV-Vis in this study is to detect wavelength shifts upon surface modification of the nanoparticles. The UV-Vis absorption spectra in the range of 400 – 1000 nm for 30 nm gold nanoparticles before and after 4-MBA immobilization are shown in Figure 2.01. The unmodified 30 nm gold nanoparticles show a characteristic surface plasmon absorption peak at 520 nm. The plasmon band showed a red shift to 522 nm after exposure to 4-MBA. The small bathochromic shift in the wavelength maximum (λ_{\max}) denotes

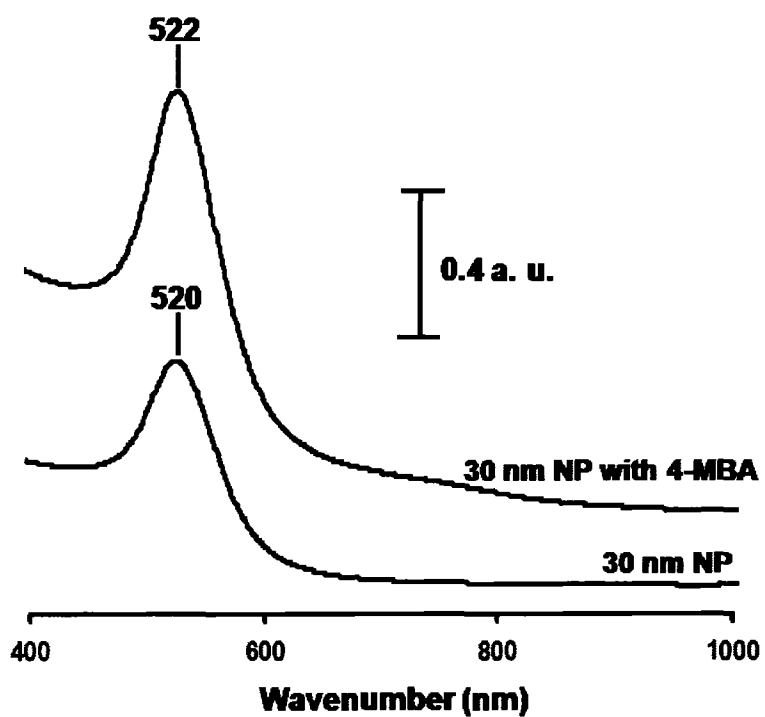


Figure 2.01. UV-Vis absorption spectra of unmodified 30 nm gold nanoparticles (30 nm NP) and 4-MBA modified 30 nm gold nanoparticle (MBANP). The unmodified and 4-MBA modified nanoparticle solution concentration used were 2×10^{10} particles/mL. Each of the solutions was diluted 5-fold prior to UV-Vis measurements.

subtle changes in optical properties of the nanoparticle upon 4-MBA adsorption. Besides, comparison of the two spectra shows an increase in absorbance and peak width of the unmodified nanoparticles upon modification with 4-MBA indicative of wavelength dependence on particle size. The UV-Vis measurement reveals the changes in optical properties of nanoparticles upon surface modification.

SERS of 4-MBA Films. To characterize the self-assembled 4-MBA films on the nanoparticles, Raman spectroscopic measurements were made. Several inherent features of SERS make it an excellent technique to study chemically modified nanoparticles. The much narrower SERS bands reduce the likelihood of spectral overlap. In addition, the optimum SERS excitation wavelength is dependent on the chemical/physical properties of the enhancing substrate. The Raman spectra of 4-MBA on planar gold substrate and powdered 4-MBA as well as SERS of 4-MBA on gold nanoparticle collected under the same experimental conditions are shown in Figure 2.02A. The inset shows the spectrum of 4-MBA film on planar gold substrate. Comparison of the powdered spectrum to monolayer spectra shows that the adsorbed 4-MBA has a similar structure to 4-MBA in the solid state. However, there is a pronounced increase in intensity when 4-MBA is adsorbed on nanoparticle which is attributable to the SERS effect of the nanoparticle substrate. The mean SERS enhancement factor (EF) was calculated by dividing the intensities at 1077 and 1587 cm^{-1} of the SERS spectrum by

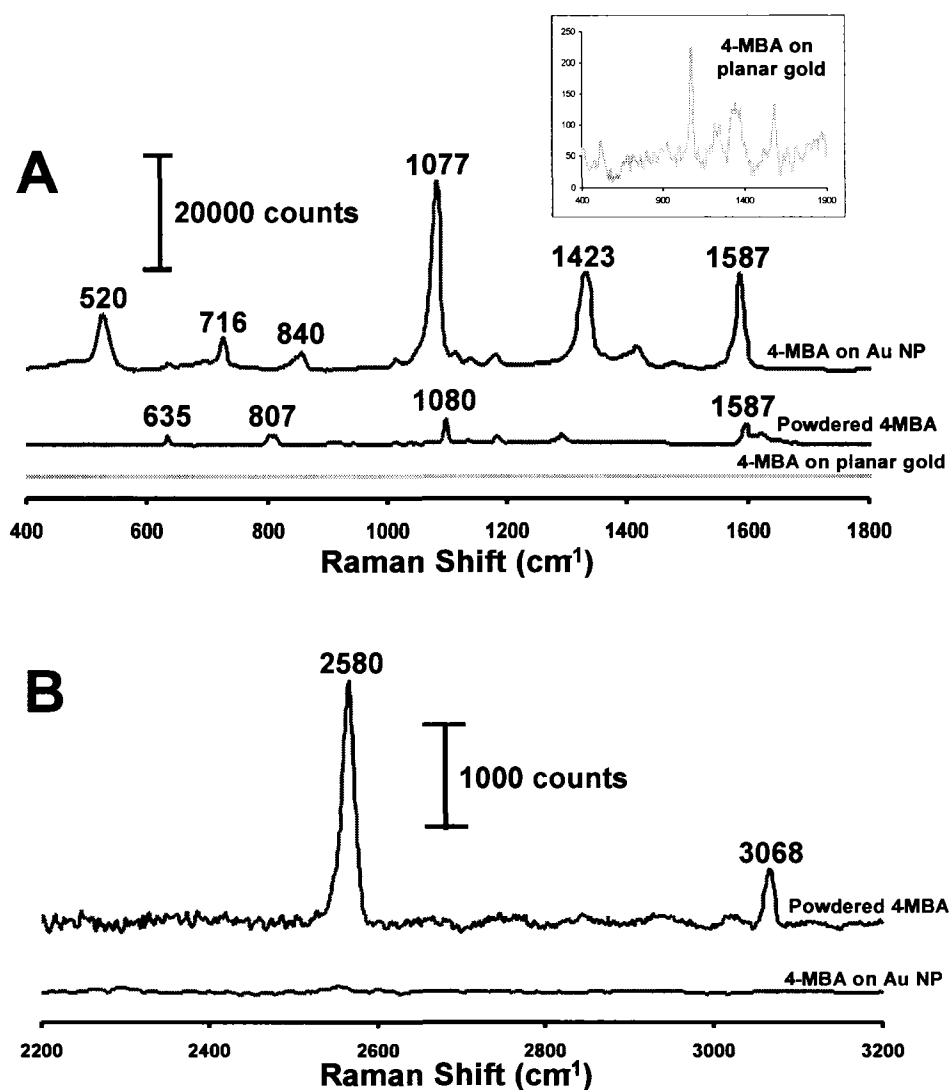


Figure 2.02. Characterization of MBANP SERS substrate. (A) Spectra showing: 4-MBA on planar gold substrate; Raman spectrum of powdered MBA and SERS spectrum of MBA. Inset shows the expanded spectrum of monolayer of 4-MBA on planar gold substrate. (B) High-wavenumber region Raman spectra of powdered 4-MBA; and 4-MBA SERS. All spectra were obtained using 785 nm laser and integration time of 10 s.

those from the planar substrate. This calculation yielded a SERS EF of 177 ± 3 . The observed EF may be attributed to cluster formation resulting from the 4-MBA film on the nanoparticle. The 30 nm diameter nanoparticles used in this study were synthesized, according to the manufacturer's specifications, via citrate reduction of tetrachloroauric acid in aqueous media. This procedure results in particles having a negative surface charge which provide the repulsive forces that keep them suspended in solution. Adsorption of SAMs to the surface of the nanoparticles displaces the surface anions and forms a cover or envelop around the metal nanoparticles.^{1, 35} The repulsive forces become disrupted and the interparticle spacing is decreased leading to nanoparticle aggregation. Aggregation of the MBANPs produces enhanced local electromagnetic fields near the surface of the nanoparticle which is responsible for the intense signal observed in the SERS spectrum in Figure 2.02A.

The advantage of the SERS technique in the provision of bands with very narrow spectral bandwidth was also exploited to identify the surface functional groups, the binding sites and possibly information on the orientation of the MBANP molecules. Strong aromatic ring vibrations at positions 1077 and 1587 cm^{-1} dominate both normal Raman and SERS spectra of 4-MBA. The bands at 716 , 840 and 1423 cm^{-1} are assigned to the out-of-plane $\gamma(\text{CCC})$ vibration of the aromatic ring, $\delta(\text{COO}^-)$ and $\nu_s(\text{COO}^-)$ respectively. However, the C=O band at about

1710 cm^{-1} was not identified in the SERS spectrum. According to Michota *et al.*,²⁹ the appearance of these bands suggests a rather tilted orientation of the 4-MBA molecule with the dissociated COO^- groups on the surface. In Figure 2.02B, the spectrum of the powdered 4-MBA shows distinct bands at 2580 and 3068 cm^{-1} which correspond to the $\nu(\text{SH})$ mode and aromatic $\nu(\text{CH})$ stretching mode respectively. The disappearance of the 2580 cm^{-1} band in the MBANP spectrum confirms the chemisorption of the thiol to the nanoparticle through the Au-S bond. Further discussions on the interactions of MBANP on different surfaces will be based on the orientation of the 4-MBA molecule alluded to in this section.

Microfluidic Patterning of Modified Nanoparticles. A microfluidic network created in PDMS provides a good way to deliver nanoparticles to modified substrates. The most common device used for patterning surfaces is PDMS. PDMS is a commercially available non-toxic silicone rubber. Its low surface energy, unreactive nature towards most chemicals and flexibility allow conformal contact between the PDMS device and substrates. Figure 2.03 shows the surface patterning scheme employed in this work. First, a planar gold substrate is placed in millimolar alkanethiol solution for a specified period of time leading to the formation of self-assembled monolayer (SAM) thiol molecules on the gold substrate. A PDMS device with 200 μm microfluidic channels (μFC) placed on the substrate allowed the formation of strong conformal

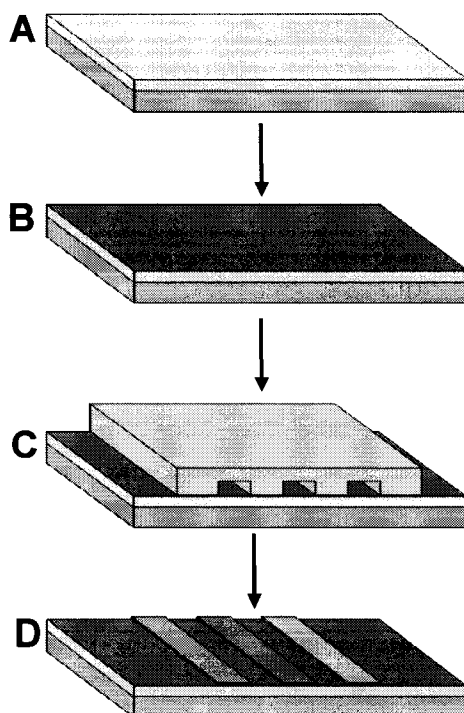


Figure 2.03. MBANP patterning via microfluidic channels (μ FCs) in PDMS: (A) Gold substrate; (B) SAM modified gold substrate; (C) PDMS device is placed on gold substrate, forming μ FCs and (D) MBANP patterned in lines via μ FCs on SAM modified gold substrate.

contact between the PDMS and the substrate. Solutions of MBANPs are then delivered through the μ FCs to the SAM modified substrate. Removal of the PDMS device leaves two-dimensional MBANP chemical patterns on the surface.

The effectiveness of our patterning procedure is demonstrated in Figure 2.04. High nanoparticle concentrations (2×10^{10} particles/mL) were employed in this study to aid in the visualization of the MBANP patterns. The optical image of the resulting pattern on an amine-terminated monolayer is shown in Figure 2.04A. The lateral dimensions of the MBANP patterns show exact replica of the relief features in the PDMS device. For example, the width of the patterns corresponds to those of the PDMS device shown in Figure 2.03 (200 μ m) and the edges of the patterns have high fidelity. Figure 2.04B shows SERS spectra collected on MBANP pattern and that of the region between the patterns. The SERS spectrum of the MBANP is dominated by strong aromatic ring vibrations at 1077 and 1587 cm^{-1} as discussed earlier. The positions of these bands are in good agreement with data shown in Figure 2.02A. The absence of detectable SERS signal from an area outside the array shows the effectiveness of our modified nanoparticle patterning scheme.

Mapping of MBANP on Different Surfaces. Raman mapping technique was employed to reveal the chemical contrast in a wide variety of samples. The Raman maps are based on point-by-point

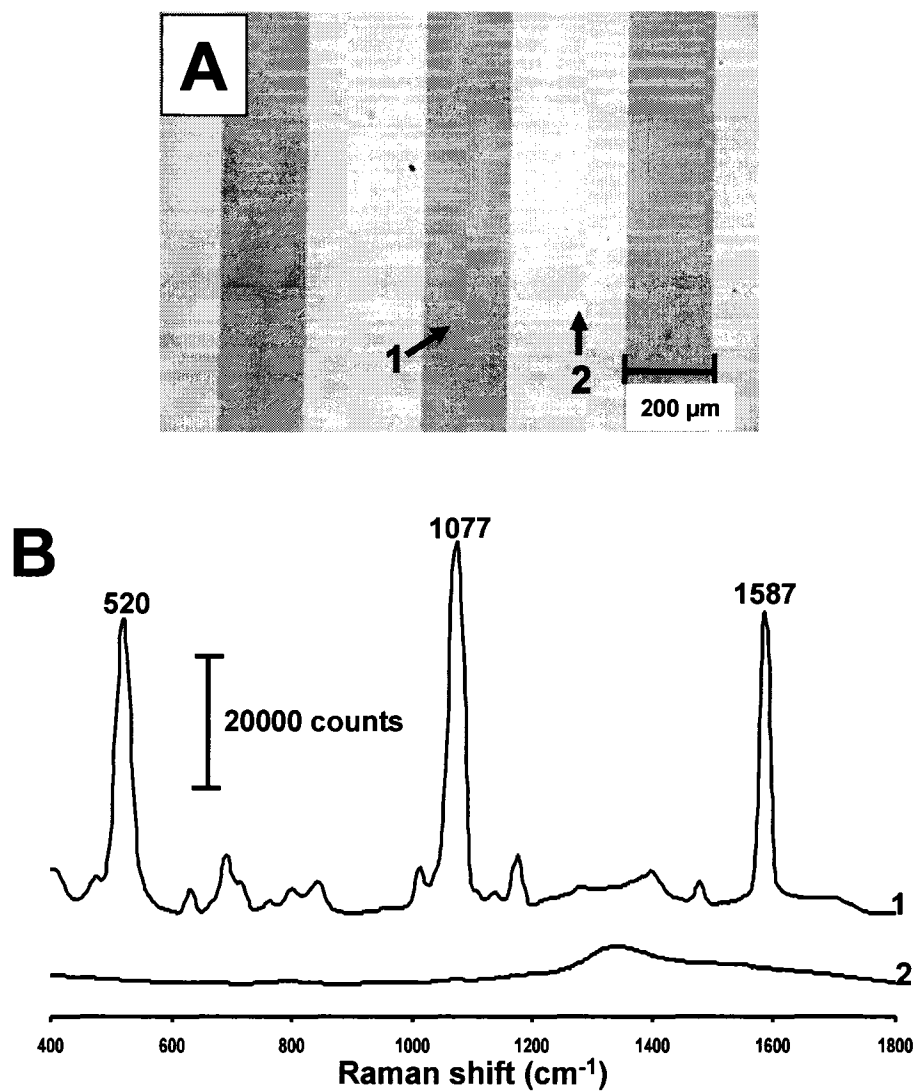


Figure 2.04. (A) Optical image of patterned MBANP on AUT surface. Arrows indicated on image correspond to regions where spectra in (B) were collected. (B) SERS spectra collected on the MBANP pattern (1) and outside the MBANP pattern (2). All spectra were obtained using 785 nm laser and integration time of 10 s.

collection of Raman spectra acquired via programmed movements of a microscope objective that focuses laser light and collects Raman scatter. Parameters such as grid size, pixel size, integration time and wavelength range govern Raman map acquisition. Figure 2.05 illustrates the steps involved in the acquisition of a Raman map of MBANP generated on the NH_2 -terminated surface.

Creation of an MBANP Raman Map. To generate a map, an optical image of the sample surface is first taken. A grid is then designed over the sample area of interest by choosing a step size which also defines the pixel size. The smaller the step or pixel size, the longer the acquisition time and the more computer memory required for information storage. We choose a step size of 100 μm for this study to collect maps within shorter time intervals (2 h). A Raman spectrum is collected from each pixel within a specified range of wavelengths and using a specific integration time. The collection of spectra continues until the analytical area has been covered. From the two dimensional (2D) collection of spectra, any one of the characteristic peaks shown in Figure 2.05B can be chosen to produce a contrast.

Raman spectra collected during a mapping experiment contain both spatial and chemical information about the mapped sample. In this section, the display of pixel intensity variation of a spectral band within a defined spectral region will be illustrated. The distinct spectral bands at positions 1077, 1180 and 1587 cm^{-1} shown in Figure 2.05B will be used

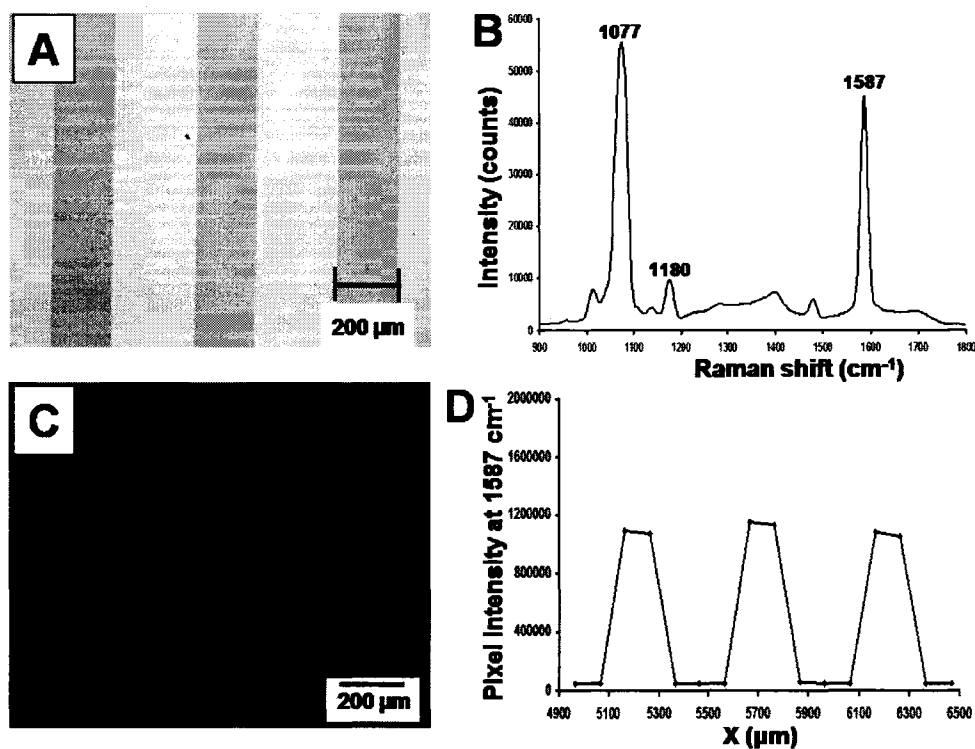


Figure 2.05. Concept of Raman mapping. (A) Optical image of MBANP patterned area to be mapped. (B) SERS spectrum showing 1587 cm^{-1} band used to generate Raman map. (C) Raman map obtained using the 1587 cm^{-1} band shown in (B). (D) Horizontal cross-sectional profile showing relative intensities of 1587 cm^{-1} of each nanoparticle labeled-MBA patterns in (C). SERS spectra were obtained using 785 nm laser and integration time of 10 s.

to create Raman maps. The ring vibration mode at 1587 cm^{-1} generated the map in Figure 2.05C. SERS-active 4-MBA regions (brighter regions) showed intense Raman scattering relative to the NH_2 -modified non-active SERS regions (darker contrast). This shows the capability of Raman mapping in revealing both chemical composition and contrast on modified surfaces. The lighter the pixel, the more intense the Raman scattering. Figure 2.05D is a horizontal cross-sectional analysis of the map in Figure 2.05C. The x-axis defines the width of the initial grid used for collection of the map. The height of pixel intensity profiles of the 1587 cm^{-1} map scales with the peak intensity of the band shown in Figure 2.05B. The width of the pixel intensity profiles corresponds to the width of the patterns shown in the optical image (Figure 2.05A). Together, these results potentially demonstrate the precision of our patterning procedure and the capability of Raman mapping technique in probing patterned structures of surfaces.

Mapping With Different Peaks. The key requirement of any surface pattern analysis is a precise spectral characterization of the unique features exhibited by the patterns. Figure 2.06 is a further demonstration of Raman mapping technique in revealing surface contrast. Raman maps acquired using the 1077 and 1180 cm^{-1} bands are shown in Figures 2.06A and 2.06C respectively. Again, regions having MBANP patterns show brighter contrast compared to those outside the patterns. The generated maps represent the spatial

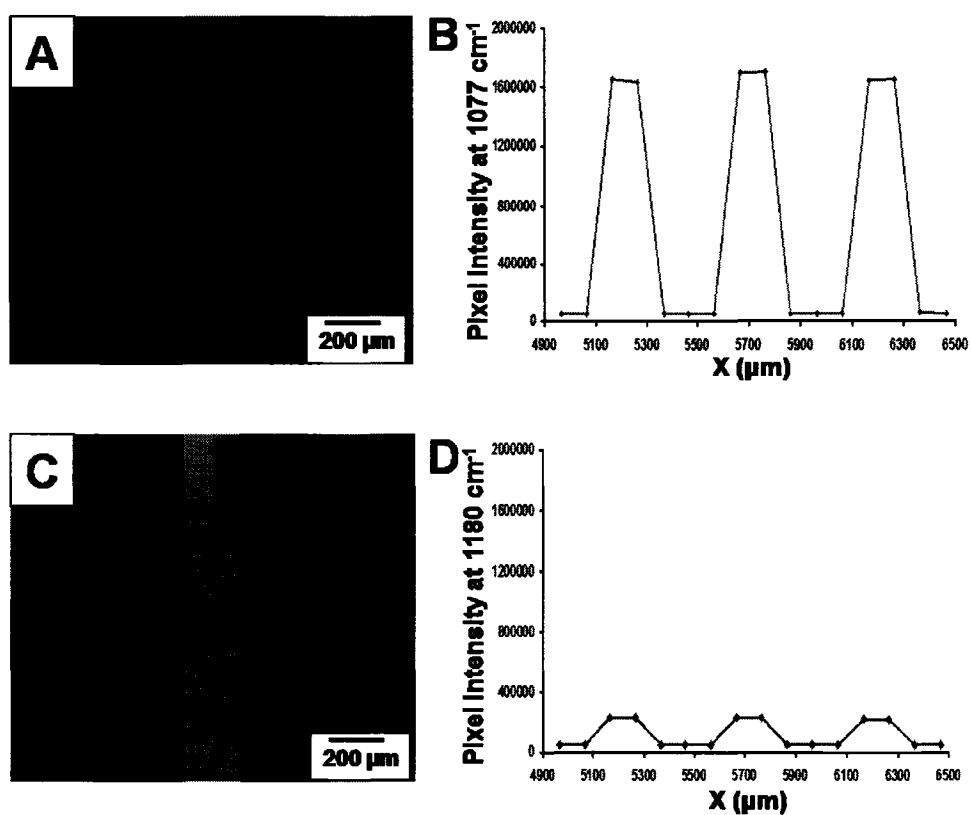


Figure 2.06. Raman mapping using different peaks. (A) Map generated using 1077 cm⁻¹ band shown in Figure 2.05B. (B) Horizontal cross-sectional profile showing pixel intensities of the patterns in (A). (C) Raman map obtained using the 1180 cm⁻¹ band. (D) Horizontal cross-sectional profile showing relative pixel intensities of map in patterns in (C).

distribution of a spectral component of interest based on its intensity at a uniquely assignable Raman shift.

SERS signal intensities can be correlated with pixel intensity profiles. The pixel intensity profiles shown in Figures 2.06B and 2.06D corresponds to the peak intensities of the 1077 and 1180 cm^{-1} bands represented in Figure 2.05B. For example, the less intense $\delta(\text{CH})$ mode at 1180 cm^{-1} observed in the SERS spectrum of MBANP showed much less pixel intensity compared to that of the more intense aromatic ring vibration at 1077 cm^{-1} . These results further confirm the ability of Raman mapping in exploring spectral features of modified nanoparticle patterns.

Mapping on Different Substrates. Surface patterning of MBANP was examined using different substrates in order to explore the versatility of both our patterning procedure and the robustness of Raman mapping technique employed in this thesis. Unmodified bare glass and polished glassy carbon (GC) substrates were examined in this case. The choice of these substrates were based on their availability in our lab and their unique chemistries. The negatively charged silica (SiO_2) layer and other functionalities present on unmodified glass substrate as well as the compositional graphitic oxide layer of GC surface might have also contributed to the attachment of the modified nanoparticles on these substrates. The conformal contact provided by the PDMS device enabled MBANP patterning on both glass

and GC substrates.

Our ability to map patterned MBANP on substrates other than planar gold substrate is demonstrated by Figure 2.07. Raman maps shown in Figures 2.07A and 2.07B were generated using the 1587 cm^{-1} ring vibration mode on the glass and GC substrates respectively. Mapping of the patterns on the GC substrate shows fairly uniformly distributed pixels compared to the map of the glass substrate. The differences in the two maps might be attributed to the influence of surface functionalities on the MBANP patterns and on the final outcome of the mapping experiment. Nonetheless, we have been able to show the possibility of mapping MBANP patterns on different substrates.

Mapping With Multiple Colors. The use of Raman mapping as a tool for multicolor imaging of different Raman reporter molecules was also investigated. In this case, three nanoparticle-labeled reporter molecules: 4-mercaptobenzoic acid (4-MBA), 2-naphthalenethiol (NAT) and 6-hydroxy-2-naphthyl disulfide (HND) were chosen based on the differences in their chemistries and spectral signatures. Figure 2.08A indicates an optical image obtained from microfluidic patterning of MBA, NAT and HND on an AUT surface. The observed patterns of the three nanoparticle-labeled reporter molecules are dictated by the surface interactions between the functional groups of the reporters and the positively charged amine groups on the planar gold substrate. SERS spectral intensities of the three nanoparticle-labeled reporter molecules

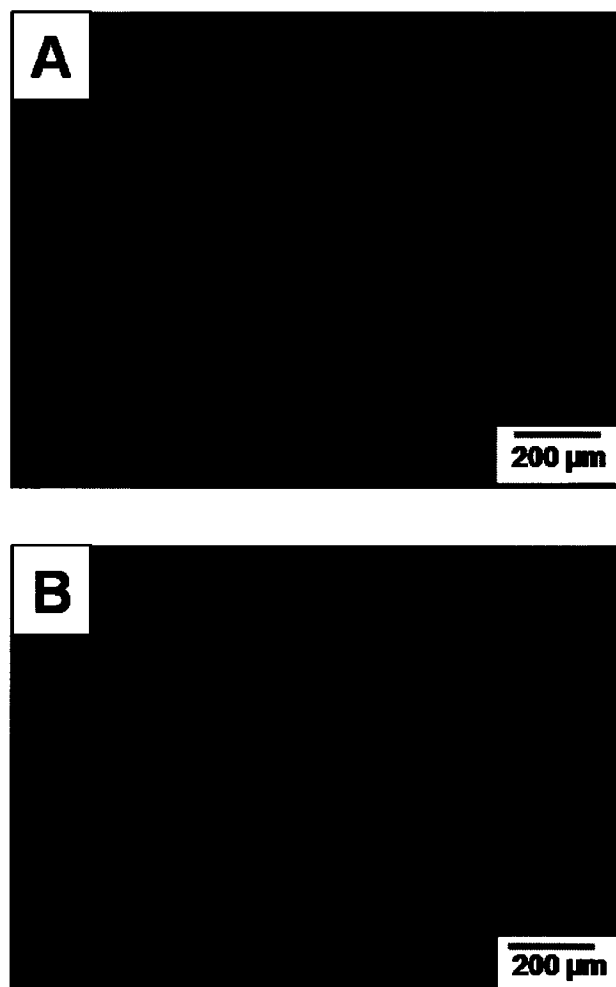


Figure 2.07. Raman maps of MBANP patterns generated using 1587 cm^{-1} band on (A) glass and (B) glassy carbon substrates.

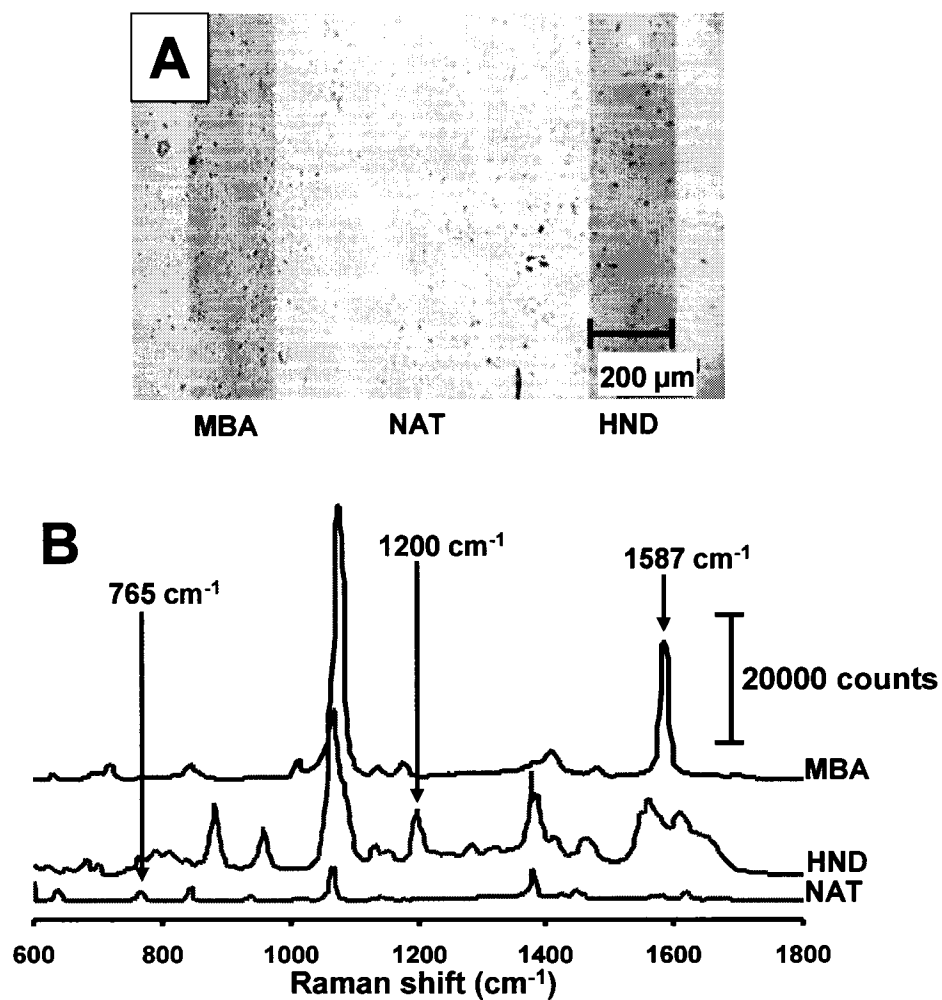


Figure 2.08. Different reporter molecules on AUT substrates. (A) Optical image showing 4-MBA, NAT and HND patterns on AUT substrate. (B) SERS spectra obtained from patterns indicating bands used to generate maps of the patterns. Assigned peaks on each spectrum were used to generate maps shown in Figure 2.10. All spectra were obtained using 785 nm laser and integration time of 10s.

shown in Figure 2.08B confirm the observed patterns in Figure 2.08A. The adsorption of 4-MBA-labeled gold nanoparticle shows higher SERS signal intensity compared to NAT and HND due to the electrostatic interaction between the carboxylic acid groups of the MBANP and the positively charged amine functionalities of the AUT monolayer.

SEM imaging was employed to visualize the particle distribution of the reporter-labeled nanoparticles since it can significantly impact the observed SERS signal intensities. Parts A, B and C of Figure 2.09 show scanning electron micrographs for nanoparticle-labeled 4-MBA, NAT and HND respectively on the AUT surface. Surface particle densities of the nanoparticle-labeled reporters on amine modified substrates correlates with their SERS signal intensities observed in Figure 2.08A. Hence, the SERS signal intensities scale with particle density which are controlled by the molecular interactions between the nanoparticle-labeled reporters and the surface. In effect, we can take advantage of the intensity variations to explore multiple color mapping of these systems.

Raman microscopic mapping is capable of performing spatially resolved raster scans of a sample surface to build up chemical images representing the spatial distribution of one or more sample components. In this study, three bands at 765, 1200 and 1587 cm^{-1} from the SERS spectra of NAT, HND and 4-MBA were respectively chosen to generate Raman maps. The choice of these three bands was to provide minimal

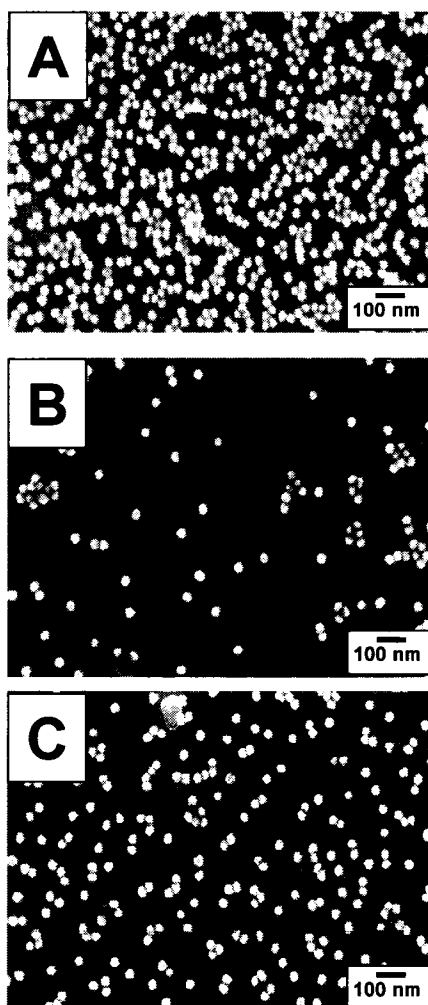


Figure 2.09. SEM Images of gold nanoparticle labeled-Raman reporter molecules: (A) 4-MBA, (B) NAT and (C) HND adsorbed on AUT-modified gold substrate. All SEM images were collected with an acceleration voltage of 10 kV.

spectra overlap. Maps generated using the 1587 cm^{-1} band as shown in Figure 2.10A distinguishes MBANP from the other labeled-reporters. The cross-sectional analysis based on Figure 2.10A presented in Figure 2.10B further confirms the differences between the three Raman reporters. Similarly, maps obtained with 1200 cm^{-1} band from labeled HND spectrum (Figure 2.10C) and its corresponding cross-sectional profile shown in Figure 2.10D clearly show the beauty of Raman mapping analysis. In addition, pixel intensity profiles scales well with SERS signal intensities of the molecules presented in this section. The very low SERS intensity of the 765 cm^{-1} ring breathing band of NAT although has been previously observed to be unique to this molecule is overshadowed by some spectral features of 4-MBA and HND³⁶. This shadowing effect is reflected in the NAT map presented in Figure 2.10E. Moreover, low signal intensity of the 765 cm^{-1} band contributed to the observed low pixel intensity profile for the nanoparticle labeled NAT molecules. However, the cross-sectional analysis of NAT map shown in Figure 2.10F clearly distinguishes NAT from HND and 4-MBA. In a nutshell, analyses of the maps presented show the potential of the Raman mapping technique in revealing differences between different Raman molecules based on their spectral signatures.

Controlling Surface Nanoparticle Density Via Chemical Interactions. To provide an effective and a viable surface patterning scheme for modified nanoparticle, interactions between the surface and

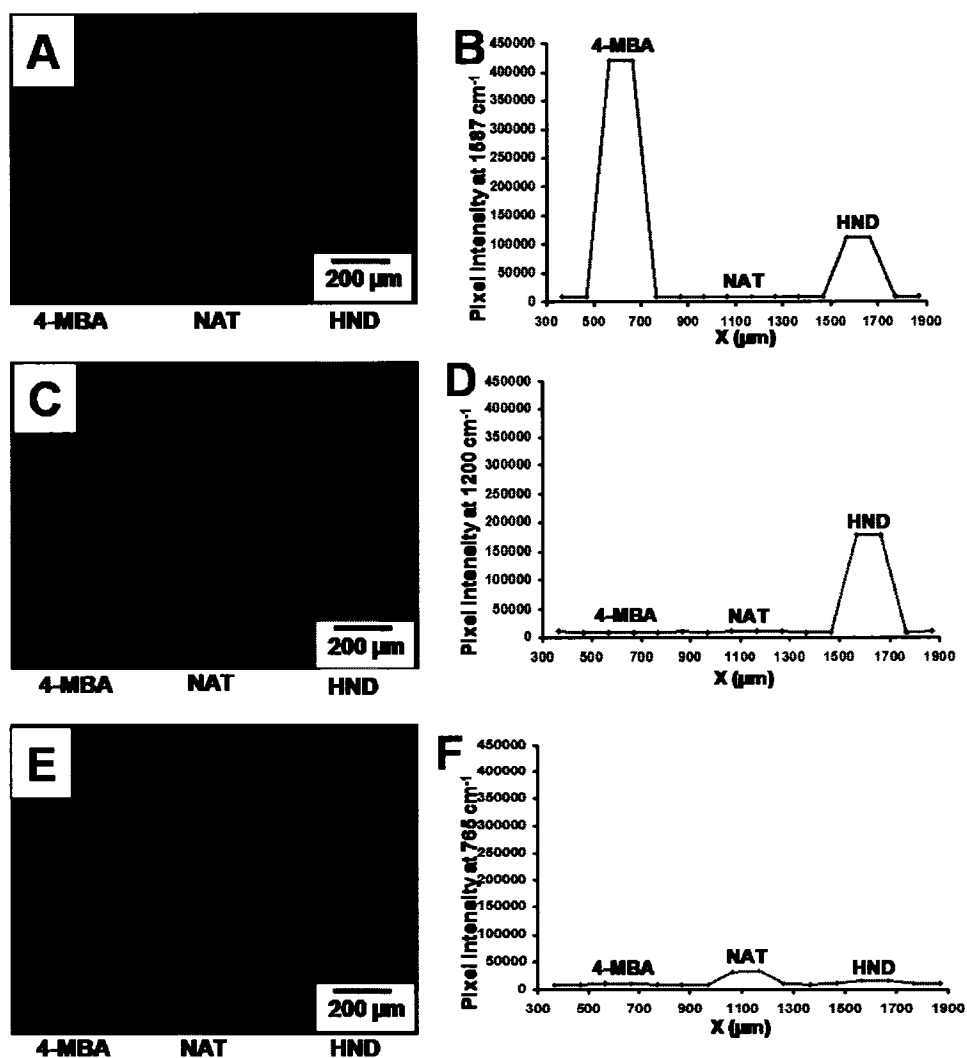


Figure 2.10. Multiple-color mapping using different bands from different reporters. (A) Raman map of 4-MBA generated using 1587 cm^{-1} band. (B) Cross-sectional profile of the map in (A). (C) Map of HND obtained using 1200 cm^{-1} band. (D) Cross-sectional analysis of map in (C). (E) Raman map of NAT using 765 cm^{-1} band. (F) Cross-sectional profile of the map in (E).

nanoparticle labels cannot be overlooked. To address this, qualitative and quantitative evaluation of SERS signal recorded in our MBANP patterns were carried out by examining the effects of surface chemistry and pH on the particle density.

Effect Surface Chemistry on Nanoparticle Density. In applications where gold nanoparticles are used as sensitive SERS labels, it will be important that the SERS signal is a measure of nanoparticle density on the surface. In this study, we can control the nanoparticle surface density by choice of the substrate and therefore by controlling the molecular interactions between 4-MBA and the surface. In order to track the effect surface chemistry on the adsorption of the MBANP, the versatile chemistry of self-assembled monolayers on gold was used. The adsorption of MBANP on amine (AUT), methyl (UDT), carboxylate (MUA) and hydroxyl (MUL)-terminated alkyl thiolate monolayers was examined. These surfaces were chosen because of their range of chemistries. Published results from our laboratory show advancing contact angle measurements from 37 ± 2 , 110 ± 1.19 , 33.0 ± 2.20 and $2.0 \pm 1.12^\circ$ for amine, methyl, carboxyl and hydroxyl terminated thiols respectively.^{37, 38} These measurements confirm the differences in surface chemistries of substrates employed in this study. Single component monolayers of the same chain length (C_{11}) were used in this study to help control surface chemistry.

The ability to directly observe the effects of substrate chemistry on adsorption of modified nanoparticles is of potential interest to studies involving patterning of nanoparticles. The main thrust of the present study was to examine the interactions between MBANP and other different surface functionalities. Figure 2.11 contains overlaid SERS spectra of adsorbed MBANP patterns on the different surfaces. The UDT surface recorded the lowest signal intensity because its uncharged hydrophobic CH_3 groups interact with the carboxylic functionalities only through weak van der Waals forces. The very low nanoparticle density observed by SEM analysis of the UDT substrate shown in Figure 2.12C reflects the dominant effect of the hydrophobic forces that mask other chemical interactions on the methyl surface. The limit of detection of our system based on Figure 2.12C is $97 \text{ particles}/\mu\text{m}^2$.

It should be pointed out that solution pH was not controlled in this study. Therefore, we expect that the deprotonated sites on both the MBANP and the MUA surface would present electrostatic repulsion towards each other. Studies performed on the surface confined carboxylic acid terminated thiolate SAMs have reported pKa of ~ 5 to 8 .³⁸⁻⁴⁰ The electrostatic repulsion presented by the deprotonated $-\text{COO}^-$ groups of the MUA modified substrate are responsible for the relatively low SERS intensities on MUA-modified surface. The scanning electron micrograph of the MBANP on MUA surface shown in Figure 2.12D is consistent with its SERS analysis.

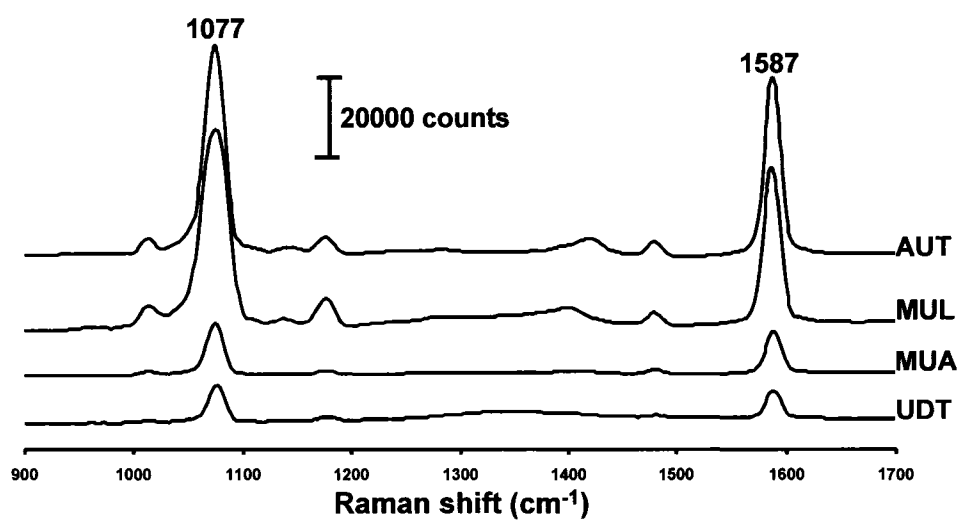


Figure 2.11. SERS investigation of MBANP adsorbed on UDT, MUA, MUL and AUT modified gold substrates. All spectra were obtained using 785 nm laser and integration time of 10 s.

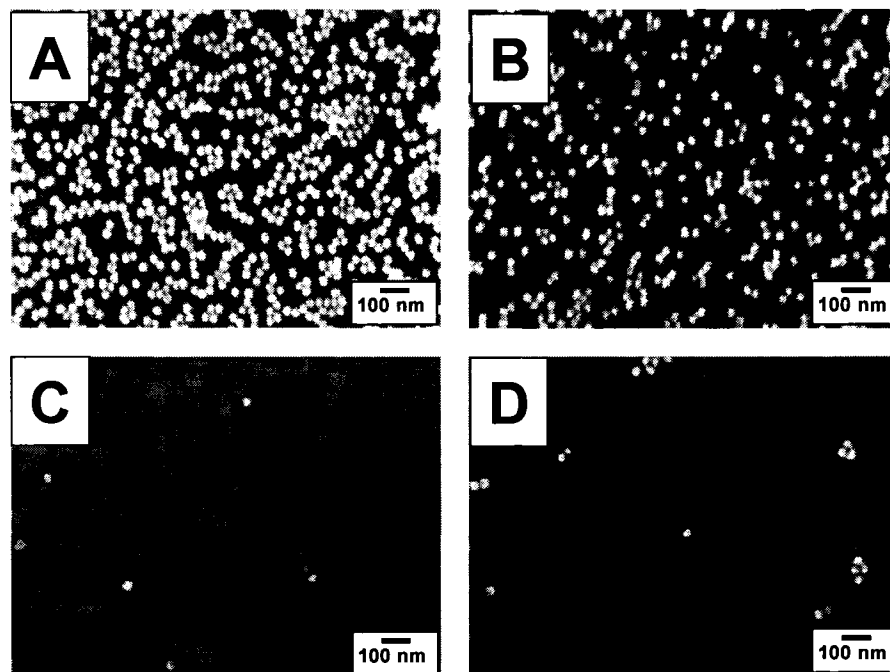


Figure 2.12. Scanning electron micrographs of MBANP adsorbed on (A) AUT, (B) MUL, (C) UDT and (D) MUA substrates. All SEM images were collected with an acceleration voltage of 10 kV.

It is also interesting to note that the SERS signal intensity recorded for the interaction between deprotonated COO^- groups of MBANP and OH functionalities of the MUL surface (Figure 2.11) is much higher than that observed for MUA. The uncontrolled pH in this study would give rise to deprotonated COO^- which interact with non-ionizing polar OH groups mainly through hydrogen bonding. Studies have also shown that the tilt angle of the polar OH SAMs tend to maximize the hydrogen bonding between the two surface groups.^{39, 41} The high surface particle density observed on the MUL surface shown in Figure 2.12B confirms the strong interaction between the carboxyl and hydroxyl surfaces.

The positively charged hydrophilic amine modified substrate produced the highest observed SERS signal. This is attributed to strong electrostatic forces between the negatively charged deprotonated carboxylic acid group of 4-MBA and the positively charged surface amine functionalities. Surface interactions on the amine surface scales with its particle density shown in Figures 2.12A. Thus, the higher surface particle density is a result of the strong interaction between the two surfaces. In addition, there is a high degree of modified nanoparticle aggregation observed on the AUT scanning electron micrograph. The electromagnetic SERS theory suggests that aggregation of particles create what are known as “hot-spots” which greatly enhances the SERS intensity.^{5, 42, 43} Nonetheless, the significant contribution from the strong

surface interactions provided the platform for these clusters and the resulting higher SERS intensity. In summary, control of surface chemistry is a key requirement for designing surface nanoparticle patterns.

Effect of Solution pH on the MBANP SERS Signal Intensity. The interaction between two substrates is controlled by their surface functional groups which is usually governed by the local pH of the environment. Hence, controlling pH will not only impact on the molecular interactions but also nanoparticle density of our patterns. The SERS studies on the effect of pH on MBA adsorption in literature tend to vary the pH of the nanoparticle solution and observe its effect on MBA adsorption^{29, 33, 34, 44}. The investigation of the effect of pH in this study was carried out on an amine modified planar gold substrate. To evaluate the pH effect, solutions of MBANP in PBS buffer were prepared and the pHs of the solutions were adjusted. We employed an AUT surface to help evaluate the observed higher particle density of the MBANP patterns on AUT substrate.

The impact of the variation of pH on SERS intensity of the MBANP adsorption to modified surface was examined in aqueous solutions. pH range of 4 to 9 was employed because the aggregation of MBANP in pH values outside this range and this has been confirmed by other studies.^{33, 34} Figure 2.13A shows the response SERS signal to changes in bulk solution pH for MBANP system. The bands in the

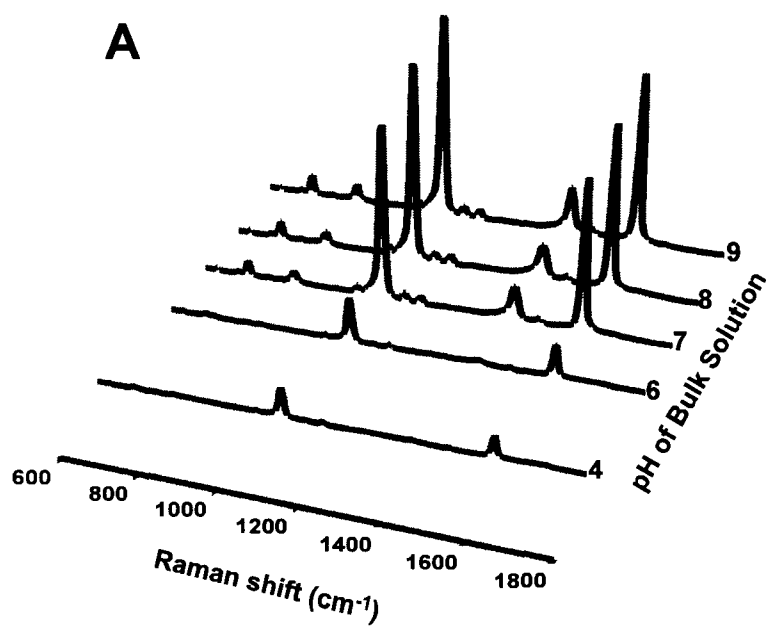


Figure 2.13A. SERS spectra showing the effect of solution pH variation on MBANP surface density on AUT modified substrate. Solution pH values were varied from 4 to 9.

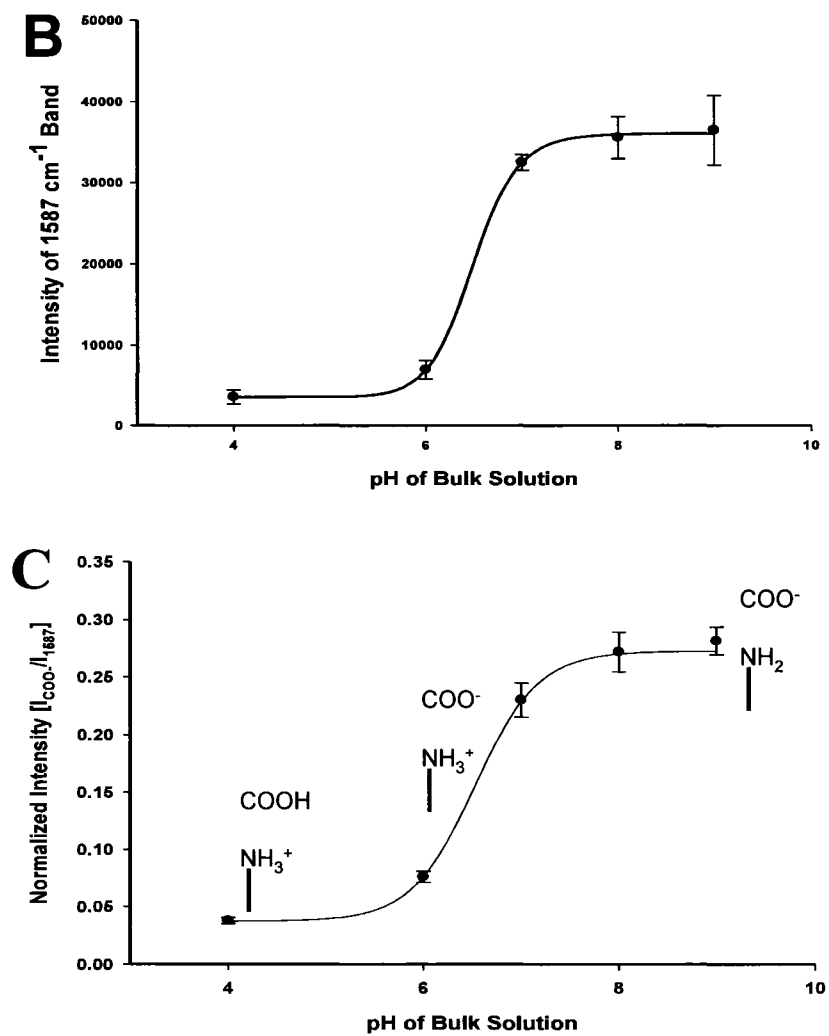


Figure 2.13 continued. Plots of (B) intensity of 1587 cm^{-1} versus pH of bulk solution and (C) normalized intensity for 1393 cm^{-1} ($\nu(\text{COO}^-)$) as a function of pH of bulk solution.

spectra are assigned to the ring breathing modes at 1077 and 1587 cm^{-1} as well as the $\nu(\text{COO}^-)$ mode at about 1393 cm^{-1} . The SERS signal intensities of these bands increase as the pH is increased from 4 to 9. At lower pH values the dominant species are the NH_3^+ from the amine surface and protonated COOH from MBANP. The interaction between these species will be rather weak resulting in lower nanoparticle surface density and hence lower SERS signals. As the pH increases, the COOH groups become deprotonated which leads to electrostatic attraction between NH_3^+ and the COO^- surface groups. The attractive forces between the species lead to increased particle density and therefore higher SERS signal intensities. For the range of pH used in this study, we expect the dominant species present at pH greater than 7 to be NH_2 and COO^- . As a result, we observe that intensity of COO^- stretching vibration band increases as pH is increased from 4 to 9. Hence, the intensity of the $\nu(\text{COO}^-)$ tracks changes in the pH of the local environment of the MBANP system. We also observed a shift from 1393 to 1417 cm^{-1} as the pH was increased from 4 to 9 for the $\nu(\text{COO}^-)$ mode which has been seen in earlier studies.^{29, 33, 34}

Moreover, the plot of 1587 cm^{-1} versus the pH of the bulk solution is shown in Figure 2.13B reveals an increase in the SERS signal intensity as the pH increases. As pH is increased, the deprotonated COO^- moieties of the MBANP surface increase. The presence of more COO^- groups will promote the interaction between MBANP and the

amine surface. As the attractive forces increases, more modified nanoparticle will bind to the amine substrate leading to an increase in the number of hot-spots and more intense SERS signals as observed in Figure 2.13A and 2.13B.

The signal intensities of the 1587 cm^{-1} band shown in Figure 2.13B were used to normalize the peak heights for the COO^- stretching mode to demonstrate that the MBANP particles are indeed sensitive to pH changes. Figure 2.13C is a plot of the results of normalized intensities for the COO^- stretching vibrational mode as a function of the pH of the bulk solution. The curve shows that the MBANP is sensitive to changes within the range of pH used in this study. From Figure 2.13C, the pKa was found to be 6.7 ± 0.2 . This surface pKa value for 4-MBA is less than the 4.2 measured for benzoic acid in solution.³⁸ This is not surprising because surface pKa values have been found to be higher than those of their solution analogs and this is attributed to changes in the number of degrees of freedom for immobilized species.^{38, 40} The results presented in this section demonstrate that we can effectively control modified nanoparticle surface density by controlling both pH and surface chemistry.

Conclusions

The work presented in this Chapter has demonstrated for the first time the use of microfluidic channels created in PDMS to chemically

pattern modified gold nanoparticles. Modified nanoparticle patterning procedure employed led to the creation of chemical patterns with very high fidelity and suitable for protein microarray applications presented in the proceeding chapters. In addition, surface chemistry plays a critical role in both particle cluster formation and attachment of reporter molecules to modified surfaces. By changing the pH of the bulk solution, we have been able to show the 4-MBA modified nanoparticle respond to changes in pH of its local environment and this opens up potential applications to biological systems which are pH-sensitive. Mapping analysis showed that there is a potential for using SERS as a qualitative tool and for material differentiation. In a nutshell, protocols developed in this study could be used to fabricate SERS-based chemical patterns and microarrays for biological applications.

References

- (1) Burda, C.; Chen, X. B.; Narayanan, R.; El-Sayed, M. A. *Chemical Reviews* **2005**, *105*, 1025-1102.
- (2) Daniel, M. C.; Astruc, D. *Chemical Reviews* **2004**, *104*, 293-346.
- (3) Moskovits, M. *Journal of Raman Spectroscopy* **2005**, *36*, 485-496.
- (4) Haes, A. J.; Stuart, D. A.; Nie, S. M.; Van Duyne, R. P. *Journal of Fluorescence* **2004**, *14*, 355-367.
- (5) Aravind, P. K.; Nitzan, A.; Metiu, H. *Surface Science* **1981**, *110*, 189-204.

- (6) Eustis, S.; El-Sayed, M. A. *Chemical Society Reviews* **2006**, *35*, 209-217.
- (7) Nicewarner-Pena, S. R.; Freeman, R. G.; Reiss, B. D.; He, L.; Pena, D. J.; Walton, I. D.; Cromer, R.; Keating, C. D.; Natan, M. J. *Science* **2001**, *294*, 137-141.
- (8) Freeman, R. G.; Grabar, K. C.; Allison, K. J.; Bright, R. M.; Davis, J. A.; Guthrie, A. P.; Hommer, M. B.; Jackson, M. A.; Smith, P. C.; Walter, D. G.; Natan, M. J. *Science* **1995**, *267*, 1629-1632.
- (9) Jeanmaire, D. L.; Vanduyne, R. P. *Journal of Electroanalytical Chemistry* **1977**, *84*, 1-20.
- (10) Raether, H. *Springer Tracts in Modern Physics* **1988**, *111*, 1-133.
- (11) Lyon, L. A.; Pena, D. J.; Natan, M. J. *Journal of Physical Chemistry B* **1999**, *103*, 5826-5831.
- (12) Porter, L. A.; Choi, H. C.; Schmeltzer, J. M.; Ribbe, A. E.; Elliott, L. C. C.; Buriak, J. M. *Nano Letters* **2002**, *2*, 1369-1372.
- (13) Morkved, T. L.; Wiltzius, P.; Jaeger, H. M.; Grier, D. G.; Witten, T. A. *Applied Physics Letters* **1994**, *64*, 422-424.
- (14) Piner, R. D.; Zhu, J.; Xu, F.; Hong, S. H.; Mirkin, C. A. *Science* **1999**, *283*, 661-663.
- (15) Xia, Y. N.; Rogers, J. A.; Paul, K. E.; Whitesides, G. M. *Chemical Reviews* **1999**, *99*, 1823-1848.
- (16) McDonald, J. C.; Duffy, D. C.; Anderson, J. R.; Chiu, D. T.; Wu, H. K.; Schueller, O. J. A.; Whitesides, G. M. *Electrophoresis* **2000**, *21*, 27-40.
- (17) Anderson, J. R.; Chiu, D. T.; Jackman, R. J.; Cherniavskaya, O.; McDonald, J. C.; Wu, H. K.; Whitesides, S. H.; Whitesides, G. M. *Analytical Chemistry* **2000**, *72*, 3158-3164.

- (18) Duffy, D. C.; McDonald, J. C.; Schueller, O. J. A.; Whitesides, G. M. *Analytical Chemistry* **1998**, *70*, 4974-4984.
- (19) Sasic, S.; Clark, D. A.; Mitchell, J. C.; Snowden, M. J. *Applied Spectroscopy* **2005**, *59*, 630-638.
- (20) Clarke, F. C.; Jamieson, M. J.; Clark, D. A.; Hammond, S. V.; Jee, R. D.; Moffat, A. C. *Analytical Chemistry* **2001**, *73*, 2213-2220.
- (21) Wang, J.; Zhu, T.; Tang, M.; Cai, S. M.; Liu, Z. F. *Japanese Journal of Applied Physics Part 2-Letters* **1996**, *35*, L1381-L1384.
- (22) Zhu, T.; Yu, H. Z.; Wang, J.; Wang, Y. Q.; Cai, S. M.; Liu, Z. F. *Chemical Physics Letters* **1997**, *265*, 334-340.
- (23) Yang, H. F.; Liu, Y. L.; Liu, Z. M.; Yang, Y.; Jiang, J. H.; Zhang, Z. R.; Shen, G. L.; Yu, R. Q. *Journal of Physical Chemistry B* **2005**, *109*, 2739-2744.
- (24) Weisbecker, C. S.; Merritt, M. V.; Whitesides, G. M. *Langmuir* **1996**, *12*, 3763-3772.
- (25) Gole, A.; Orendorff, C. J.; Murphy, C. J. *Langmuir* **2004**, *20*, 7117-7122.
- (26) Driskell, J. D.; Kwart, K. M.; Lipert, R. J.; Porter, M. D.; Neill, J. D.; Ridpath, J. F. *Analytical Chemistry* **2005**, *77*, 6147-6154.
- (27) Johnson, S. R.; Evans, S. D.; Brydson, R. *Langmuir* **1998**, *14*, 6639-6647.
- (28) Orendorff, C. J.; Gole, A.; Sau, T. K.; Murphy, C. J. *Analytical Chemistry* **2005**, *77*, 3261-3266.
- (29) Michota, A.; Bukowska, J. *Journal of Raman Spectroscopy* **2003**, *34*, 21-25.
- (30) Xia, Y. N.; Whitesides, G. M. *Angewandte Chemie-International Edition* **1998**, *37*, 551-575.

- (31) Graham, D. J.; Price, D. D.; Ratner, B. D. *Langmuir* **2002**, *18*, 1518-1527.
- (32) Ni, J.; Lipert, R. J.; Dawson, G. B.; Porter, M. D. *Analytical Chemistry* **1999**, *71*, 4903-4908.
- (33) Bishnoi, S. W.; Rozell, C. J.; Levin, C. S.; Gheith, M. K.; Johnson, B. R.; Johnson, D. H.; Halas, N. J. *Nano Letters* **2006**, *6*, 1687-1692.
- (34) Talley, C. E.; Jusinski, L.; Hollars, C. W.; Lane, S. M.; Huser, T. *Analytical Chemistry* **2004**, *76*, 7064-7068.
- (35) Schmid, G. *Chemical Reviews* **1992**, *92*, 1709-1727.
- (36) Alvarez-Puebla, R. A.; Dos Santos, D. S.; Aroca, R. F. *Analyst* **2004**, *129*, 1251-1256.
- (37) Nsiah, F. MSc., University of Alberta, Edmonton, 2003.
- (38) Vezenov, D. V.; Noy, A.; Rozsnyai, L. F.; Lieber, C. M. *Journal of the American Chemical Society* **1997**, *119*, 2006-2015.
- (39) Vezenov, D. V.; Noy, A.; Ashby, P. *Journal of Adhesion Science and Technology* **2005**, *19*, 313-364.
- (40) Hu, K.; Bard, A. J. *Langmuir* **1997**, *13*, 5114-5119.
- (41) Kwon, Y. J.; Park, S. S.; Kim, K.; Kim, M. S. *Journal of Raman Spectroscopy* **1994**, *25*, 655-661.
- (42) Aravind, P. K.; Metiu, H. *Surface Science* **1983**, *124*, 506-528.
- (43) Liver, N.; Nitzan, A.; Gersten, J. I. *Chemical Physics Letters* **1984**, *111*, 449-454.
- (44) Lee, S. B.; Kim, K.; Kim, M. S. *Journal of Raman Spectroscopy* **1991**, *22*, 811-817.

CHAPTER III

NANOPARTICLE-BASED SURFACE ENHANCED RAMAN SPECTROSCOPIC IMAGING OF BIOLOGICAL ARRAYS

Introduction

In Chapter II, microfluidic patterns and Raman mapping were employed to functionalized gold nanoparticles. These techniques and protocols are further developed in this chapter for application in biomolecular interaction analysis. This chapter presents a surface-enhanced Raman spectroscopic (SERS) method for high-sensitivity detection and reading of protein microarrays.

The discovery of SERS in the early seventies ushered in a new era of Raman spectroscopy.¹ Application of the SERS technique as a bioanalytical tool is surging in recent times.²⁻⁵ Biological compounds studied via SERS include amino acids,⁶⁻⁸ enzymes,⁹⁻¹² DNA,^{13, 14} RNA,¹⁵ fatty acids,^{16, 17} lipids^{18, 19} and antibodies.^{4, 5, 20-27} The extensive progress made in the development of reliable SERS substrates for the past few decades has driven the SERS application for bioanalysis. In addition, SERS spectral bands are significantly narrower than those of fluorescence thus preventing possible spectral overlaps. Another advantage is the surface selectivity SERS offers. Only molecules or species on or close to the metal surface can provide SERS signal. Finally, SERS is a viable technique for sensitive biological detection since it is insensitive to

humidity, oxygen and other quenchers.^{28, 29} However, a major hurdle in the application of SERS in biomolecular analysis is the development of SERS-active substrates that provide reproducible, large enhancement and that are also adaptive to biological systems.

Electrochemically roughened metal surface, the first SERS-active substrate to be fabricated, served as the basis for extensive theoretical studies. Subsequently, noble metal nanoparticles (such as silver and gold) gained widespread use because of their easy synthesis and tuneable optical properties. For example, silver and gold nanoparticles have been adapted in many studies for use in solid-surface-based substrates.³⁰⁻³² The surface properties of these nanoparticles play an important role in their reaction and stability in surface analysis since the surface is the connection of the nanoparticles to the substrate materials. In view of this, surface chemical modification of the nanoparticles is usually employed especially for biological applications.

SERS holds great possibilities for biomolecular applications. However, direct detection of biological species is still problematic. The limitation to intrinsic SERS detection of biologically relevant molecules such as proteins, drugs, nucleic acids, etc. arises from the complexities in their structures.³³ Since these molecules are built from a limited number of basic units, they tend to have structural similarities leading to spectral overlaps. To further compound this problem, most of these biomolecules

are weak Raman scatterers and do not bind to SERS-active substrates making low-sample detection a near impossible task. Recently, a wide variety of SERS substrate modification schemes have been developed with the view to impart selectivity and robustness to SERS-based bioanalysis.³⁴ These coatings are generally in the form of thin metal films and organic coatings made up of monolayers of SAMs or bioreceptors. Silver staining enhancement which involves vacuum evaporation of thin silver films on spin-coated gold nanoparticles and other metals has been proposed for immunological studies.^{27, 34-36} Surface enhancement afforded by coupling metal nanoparticles to extrinsic SAMs as Raman labels have also proven to be a valuable factor in SERS bioanalysis applications.^{22, 23, 26, 37-40} Extrinsic SERS labeling techniques provide higher signal intensities and characteristic SERS spectral features with minimal overlap thus opening pathways for multiplexing.

Immunoassays are powerful bioanalytical methods that utilize antibodies as analytical reagents for specific recognition of antigens. Conventional labelling immunoassay techniques such as fluorescence,^{41, 42} enzyme-linked immunosorbent assay^{43, 44} and chemiluminescence⁴⁵ have also been extensively demonstrated. Label-free measurement of antigen binding to antibodies immobilized on a microarray platform has been studied using surface plasmon resonance (SPR).^{46, 47} Many novel methods for SERS-based immunoassays have been employed in recent times. In

one instance, silver nanotriangles synthesized using fabricated nanosphere lithography (NSL) arrays have been used in a prototypical immunoassay involving biotin and anti-biotin, an IgG antibody.⁴⁸ Ni *et al.* introduced another SERS-based immunoassay that utilizes Raman labeled gold nanoparticles labeled with both Raman reporter molecules and antibodies for simultaneous detection of rabbit and rat IgG.²⁶ Later, using a different design of Raman labeled immunogold nanoparticles, femtomolar detection of free-prostate specific antigen was reported.²³ Dou *et al.* have introduced an enzyme immunoassay for mouse IgG utilizing SERS of the enzyme reaction product. In their system, a secondary antibody labeled with peroxidase was reacted with o-phenylenediamine to produce azoaniline. SERS signals from azoaniline adsorbed to silver nanoparticles were then used to estimate the concentration of the antigen (mouse IgG).²¹ Despite the elegance of the methods discussed above, no one has studied SERS-based immunoassays in a microarray format.

Microarray analysis commonly relies on robotic spotting and fluorescent labeling. The concepts and methodology developed in Chapter II are applied to fabricate protein microarrays for SERS reading based on gold nanoparticle labels. Specifically, this chapter describes a systematic study on the overall binding specificity of nanoparticle-labeled antibody-antigen complexes on a microarray platform. The array fabrication is based on microfluidic patterning methods and detection relies on gold

nanoparticle labeling procedures. Our efforts towards using Raman mapping in reading antibody-antigen arrays will also be discussed.

Experimental

Reagents and Materials. All aqueous solutions were prepared using water from a Nanopure (Barnstead, Dubuque, IA) purification system. Gold nanoparticles (30 nm, BBI International, UK) were purchased and used as received. Buffer solution employed salts from Fisher Scientific Company (Ottawa, ON). Phosphate buffered saline (PBS, pH 7.4) contained 1.4 mM KH_2PO_4 and 4.3 mM Na_2PO_4 , 137 mM NaCl and 2.7 mM KCl. 1 mM PBS was used to prepare all protein solutions. Bovine IgG (blgG) and anti-bovine IgG (ablgG) were purchased from ICN Biomedicals (Aurora, Ohio). ablgG was diluted with PBS to achieve concentrations of 1067 nM and blgG diluted to various concentrations ranging from 67, 134, 333, 667 and 1340 nM. Chicken lysozyme (LYS) and bovine serum albumin (BSA) (fraction V, 99% protein) were obtained from Sigma (St. Louis, MO) and were prepared to concentrations of 100 $\mu\text{g}/\text{mL}$ and 1 mg/mL respectively. The monoclonal antibody Se 155-4 which binds to Salmonella epitopes (disaccharide) was received in 6.15 mg/mL solution in 0.05 M Tris buffer with 0.15 M NaCl and 0.02% NaN_3 (a gift from Dr. David Bundle from University of Alberta). 11-amino-1-undecanethiol (AUT) was purchased from Dojindo Laboratories (Kumamoto, Japan). 3,3'-Dithiodipropionic acid

di(*N*-hydroxysuccinimide ester) (DTSP) was purchased from Aldrich (Milwaukee, WI). 5,5'-Dithiobis(succinimidyl-2-nitrobenzoate) (DSNB) was synthesized following the procedure published by Grubisha *et al.* with slight modifications.²³ An outline of the synthetic procedure follows. 0.50 g of 5,5'-dithiobis(2-nitrobenzoic acid) (DNBA), 0.52 g of 1,3-dicyclohexylcarbodiimide (DCCD) and 0.29 g of *N*-hydroxysuccinimide (NHS) were added to 50 mL of dry tetrahydrofuran (THF) in a 100 mL round-bottom flask equipped with a drying tube. The mixture was magnetically stirred at 25 °C for 18 h. The progress of the reaction was monitored on a thin layer chromatography (TLC) plate. A 2:1 ratio of methanol:ethylacetate was used for the TLC since the product was more polar. The reaction was stopped when the percent product was about 95 %. The crude product was filtered, washed with ethylacetate and rotoevaporated to remove solvent. Recrystallization was carried out in an ethylacetate-hexane two-solvent system which yielded a yellow product. The final product was further washed in cold hexane and dried overnight using vacuum pump yielding about 98 % pure DSNB compound based on melting point determination. Electrospray mass spectrometry verified the correct mass (590.00503; Na adduct) and proton nuclear magnetic resonance (¹H NMR) spectroscopy confirmed the structure.

Substrate Preparation and Fabrication of PDMS Stamps. Glass slides (Dow Corning, 0211, 18mm x 18mm x 1mm) substrates used were

pre-cleaned in piranha solution (1:3 H₂O₂:H₂SO₄) at 90°C for 15 min, rinsed several times with deionized water and dried with argon. Thin gold films were thermally evaporated onto the glass slides as discussed in Chapter II. The 10-channelled microfluidic Poly(dimethyl)siloxane (PDMS) devices were fabricated according to a published procedure⁴⁹ as outlined in Chapter II. Briefly, a relief pattern of photoresist on a silicon wafer was created by photolithography. A negative of the relief was formed in the PDMS by curing a 10:1 w/w mixture of the prepolymer and cross-linker (Sylgard 184, Dow Corning, Midland, MI) against the relief structure. The microchannels measured 200 μm wide and 10-15 μm deep. Each PDMS device was cleaned in 2:1 ethanol/water mixture and sonicated for 15 min prior to use. The cleaning procedure was repeated three times for each device. Inlet and outlet holes were through-bored in the PDMS device to allow fluid access to the channels when in conformal contact with the substrate. Fluid flow was driven by applying vacuum suction to the outlet while connecting the inlet to a reservoir of solution.

Preparation of Raman Reporter-Labeled Gold Nanoparticles. The Raman reporter-labeled gold nanoparticles were prepared following the procedure outlined by Grubisha *et al.*²³ Briefly, as shown in Figure 3.01, the unconjugated 30 nm gold nanoparticles were linked to a bi-functional Raman reporter molecule, DSNB, through the spontaneous adsorption of thiol molecules on gold. A 100 μL aliquot of 2.5 mM DSNB solution

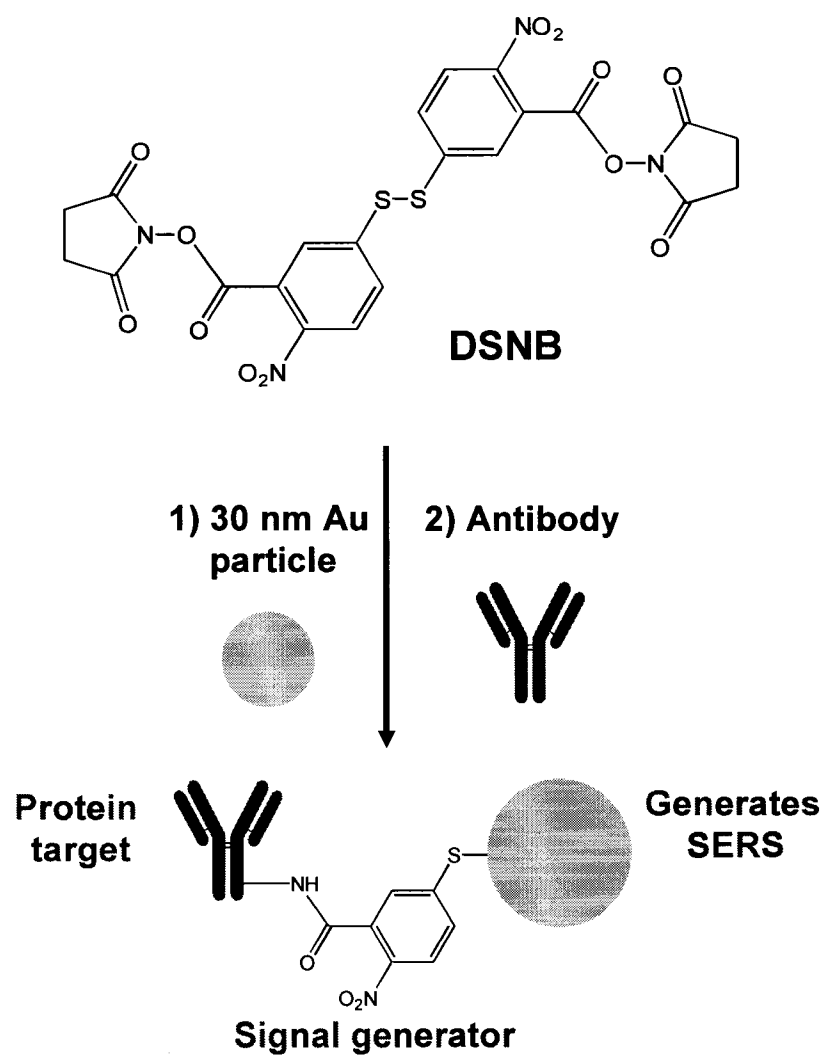


Figure 3.01. Cartoon representation of DSNB-functionalized nanoparticle-labeled antibody.

dissolved in acetonitrile was added to 1 mL of an unconjugated gold nanoparticle solution and incubated for 3-5 h. The resultant Raman reporter-labeled gold nanoparticles were then separated at 10000 rpm for 7 min. The nanoparticles were redispersed in 1 mL of deionized water from a Nanopure (Barnstead, Dubuque, IA) purification system and centrifuged again as above to remove unbound species. After this step, the gold nanoparticles were finally redispersed to a final volume of 1 mL with deionized water prior to antibody attachment. A 7 μ L of 1067 nM solution of anti-bovine IgG was added to the DSNB-labeled nanoparticles for about 12 h and centrifuged at 10000 rpm for 7 min. After the discharge of the supernatant liquid, the modified nanoparticles were suspended in 1 mM PBS at pH 7.4 and centrifuged as above to remove any unbound proteins. Antibodies are linked to the gold nanoparticles via a bi-functional DSNB is depicted in Figure 3.01. The use of PBS concentrations higher than 2 mM tend to cause aggregation of the particles.

Substrate Modification and Patterning. Figure 3.02 is a representation of the assay studied in this work. The thin gold film substrates were modified through self-assembly of NH_2 -terminated thiol (AUT). Typically, gold-coated chips were immersed in a 2 mM aqueous solution of AUT overnight. After the specified assembly time, the slides were removed from solution and rinsed well with deionized water to remove unbound thiols from the surface, and then dried with a stream of

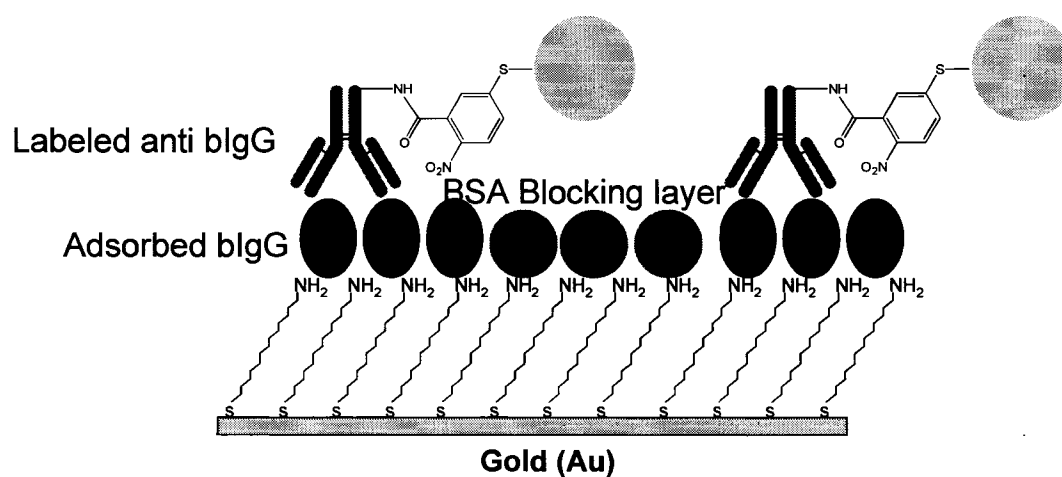


Figure 3.02. Cartoon representation of the interaction of labeled-target with probe molecules on an NH_2 -modified planar gold substrate.

argon. Arrays of protein antigens were constructed in a three-step process using polydimethylsiloxane (PDMS) microfluidic networks as shown in Figure 3.03. First, the PDMS stamp with microchannels was brought into conformal contact with the AUT-modified planar gold substrate. Solutions of bovine IgG (blgG) in buffer were introduced into the channels for 2 h. During this time the blgG adsorbed onto the NH₂-terminated monolayer. The channels were rinsed with 1 mM PBS buffer and then the PDMS stamp was removed, resulting in a pattern of 200 μm bovine IgG lines. Next, the entire chip was immersed in 0.1 % BSA in 1 mM PBS buffer solution for 1 h to block non-specific adsorption. Finally, a second set of microfluidic channels is placed perpendicularly to the bovine IgG lines and a solution of nanoparticle labeled antibodies was then patterned across the bovine IgG lines. Solutions were left in the channels for about 12 h but typically the antigen antibody interaction takes only 1-2 h to complete. An optical image of the resulting protein array is shown in Figure 3.03D. The contrast is due to specific antigen-antibody interaction.

Nanoparticle Etching. The DSNB functionalized nanoparticle labeled antibody samples were prepared as discussed earlier in this chapter. Samples were centrifuged three times to remove any unbound protein and the supernatant liquid was discarded in each case. 100 μL of 0.072 M KCN solution was added to 1 mL of ablgG-modified nanoparticle solution and left overnight at room temperature. Etching of the gold nanoparticles

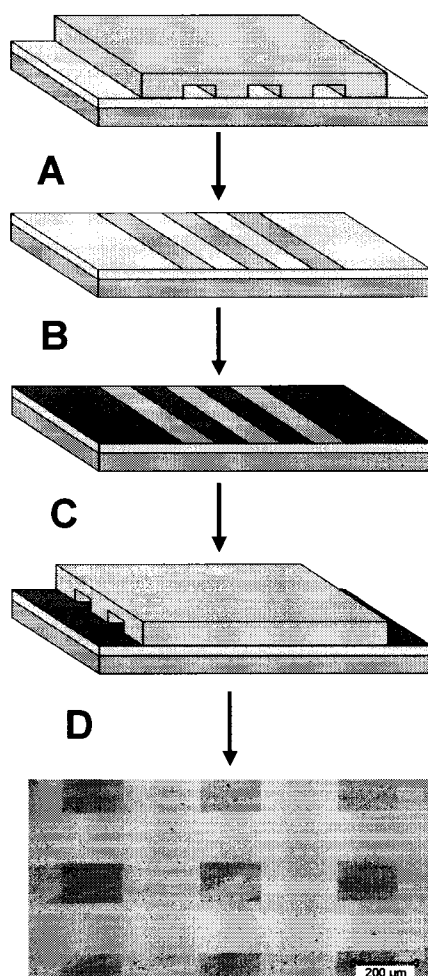


Figure 3.03. Surface patterning via microfluidic channels (μ FCs) in PDMS. (A) Probe (bIgG) patterned in lines via μ FCs on AUT SAM-modified gold substrate. (B) Gold is backfilled with BSA to block non-specific adsorption; (C) Second set of μ FCs is placed perpendicularly to pattern Gold-DSNB-abIgG. (D) Optical image of patterned nanoparticle-labeled target arrays on modified gold surface.

resulted in a color change from red to brown. Solution was loaded into Spectra/Pro dialysis tubing (MWCO 12000 – 14000) and left in 10 mM PBS for 24 h. Dialysis was repeated three times to concentrate the protein and ensure removal of salts and other contaminants. The resulting solution was transferred to a vial and centrifuged at 32000 rpm for 10 min to separate the gold nanoparticles. Five dilutions of protein standards of 160 µg/mL unmodified anti-bovine IgG were prepared. 800 µL of each standard and sample were pipetted into a clean dry microtitre plate with specific address. These solutions were stained with 200 µL of Coomassie Blue G-250 reagent dye, stirred very well and incubated for 5 min prior to analysis. Spectroscopic analysis was performed using a Spectra max 340PC Absorbance microtitre plate reader at a wavelength of 595 nm. The output from the instrument is determined by a difference measurement and the number of anti-bovine IgG molecules bound to each nanoparticle was calculated.

Instrumentation: (1) *UV-VIS Spectroscopy Measurements.*

Absorption spectra were obtained using a Pelkin Elmer Lambda 35 UV/VIS spectrometer with a 10 mm optical path length.

(2) *Surface-Enhanced Raman Scattering (SERS) Measurements.*

SERS spectra were recorded with a Renishaw inVia Raman Microscope equipped with a high-performance near-IR (HPNIR) diode (785 nm, 1200 W/mm) lasers, and a CCD detector. Radiation of 785 nm from air-cooled

diode laser was used for excitation. Laser power at the sample was 10 mW measured using power meter. The microscope attachment was based on a Leica system. A 5X objective was used to first focus the laser beam and then switched to a 50X objective to collect spectra and maps. Data for Raman maps were collected over a 1 mm x 1 mm area using a step size of 50 μm controlled by an automated motorized XYZ scanning stage. All reported maps and spectra were the result of 10 s accumulations.

(3) *Scanning Electron Microscopy (SEM) Measurements.* SEM images were collected using a Hitachi S4800 FE-SEM system (Hitachi Scientific Equipment, Japan) equipped with ultrahigh resolution, low voltage 10 kV SEM inspection with advanced sample navigation package.

(4) *Infrared Reflection Absorption Spectroscopy (IRRAS).* IRRAS spectra were collected with a Mattson Infinity FTIR Spectrometer (Madison, WI) equipped with a low-noise mercury-cadmium-tellurium (MCT) detector cooled with liquid N_2 to about 77 K. A reflection accessory and a home-built sample holder housed in an external auxiliary bench were employed. The self-assembled monolayer of DSNB on Au was formed after 1 h adsorption. Anti-bovine IgG films were formed by immersing the DSNB-modified Au slides in the protein solution for 2 h. Spectra for the DSNB monolayer and anti-bovine IgG samples were collected at 2 cm^{-1} resolution with a glancing angle of 86°. A self-

assembled deuterated octadecanethiol, a gift from Dr. John-Bruce Green (University of Alberta), was used as the background.

Results and Discussion

We first demonstrate the need for the extrinsic Raman label (Figure 3.01) in this assay. Figure 3.04 contains Raman spectra of anti-bovine IgG linked to 30 nm gold nanoparticles in three different ways. The first method involves the simple adsorption of bovine IgG to unmodified nanoparticles. The nanoparticles were deposited onto the NH_2 -terminated planar gold substrate and the spectrum in Figure 3.04A was collected. No bands characteristic of adsorbed protein are observed in the spectrum. This result shows the limitations of the direct SERS-based detection of proteins. The second attachment scheme involves covalently linking the antibody to the nanoparticles. The bifunctional molecule, 3,3'-dithiodipropionic acid di(*N*-hydroxysuccinimide ester) (DTSP) (inset Figure 3.04B) was employed. The disulfide group of DTSP promotes adsorption to the gold nanoparticles and the NHS group is reactive to free- NH_2 groups on the protein. Figure 3.04B is the Raman spectrum of antibody modified nanoparticles using DTSP. Again, no discernable spectral features from the protein or the DTSP are apparent. It is expected that molecules on or very close to the metal surface must contribute to the SERS signal. However, no detectable characteristic protein peaks were observed in the spectrum. This confirms

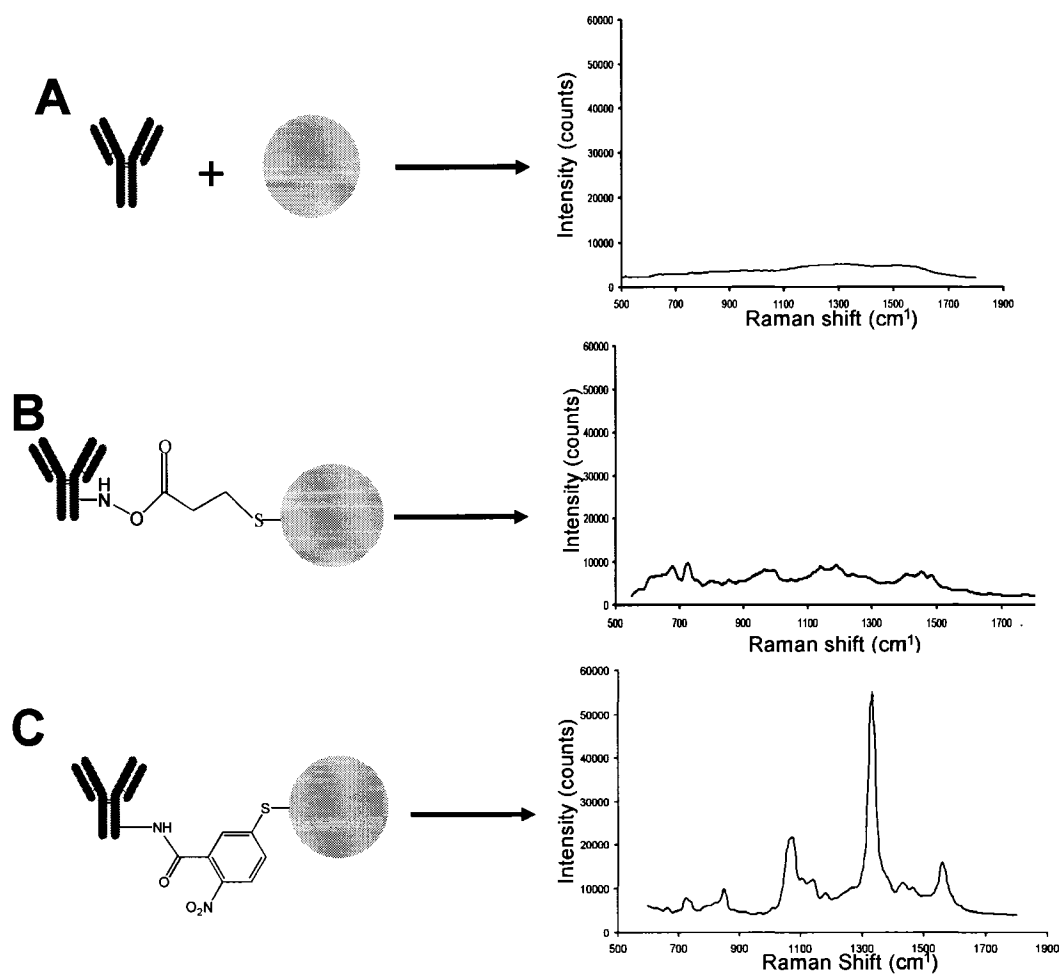


Figure 3.04. Significance of DSNB reporter molecule: (A) Direct SERS of protein. (B) SERS of DTSP-linked ablgG. (C) SERS showing the detection with DSNB reporter molecule. SERS spectra were obtained using 785 nm laser and integration time of 10 s.

considerable difficulties inherent in direct SERS detection of biomolecules such as proteins, DNA and enzymes. This claim is supported by earlier reports from Vo-Dinh's group on DNA^{4, 13, 34, 37} and several other studies conducted on proteins.^{22, 23, 26, 38, 50, 51} The third method for conjugating the antibody to the gold nanoparticles is through the extrinsic Raman label, DSNB (Figure 3.01). DSNB contains bifunctionality similar to DTSP. DSNB also contains a nitrobenzene moiety that provides a strong Raman signal. Figure 3.04C is the Raman spectrum of the antibody labeled nanoparticles using a DSNB linker. Intense bands corresponding to the nitrobenzene are observed as has been reported previously.²³ Hence, the signal from the DSNB reporter molecule, particularly the strong symmetric NO₂ stretch at 1332 cm⁻¹, will be used in this chapter for the detection of antigen-antibody interactions.

Characterization of Nanoparticle Labeling Procedure. Detailed step-wise characterization of the labeling procedure was also carried out using UV-Vis and Raman spectroscopic techniques.

UV-Vis Characterization. Adsorption of molecules to metal nanoparticle surfaces causes slight changes in their optical properties. These changes in the optical properties are observed as shifts in the oscillation frequency of the surface plasmon bands. The oscillation frequency is observed in the visible region for gold nanoparticles. UV-Vis spectroscopy was therefore employed to examine shifts in absorbance

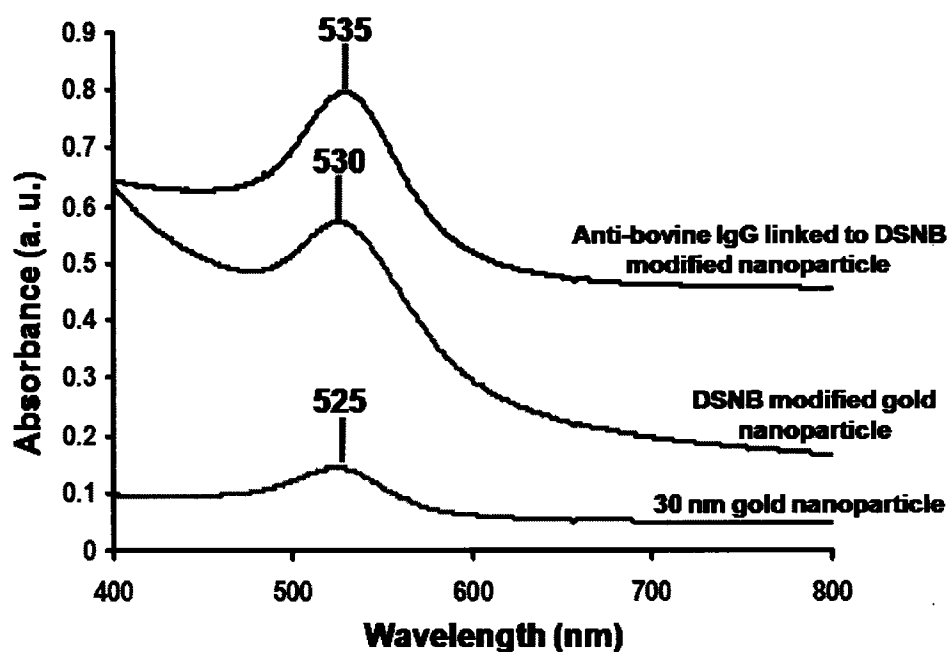


Figure 3.05. UV-Vis characterization of nanoparticle labeling procedure. UV-Vis spectra of: 30 nm unmodified gold nanoparticles; DSNB-modified gold nanoparticles and adsorption of anti-bovine IgG conjugated to DSNB modified gold nanoparticles.

maxima upon anti-bovine IgG adsorption to gold nanoparticles. Figure 3.05 shows the UV-Vis spectra of the anti-bovine IgG-labeled gold nanoparticles at different stages of preparation. The UV-Vis measurements repeatedly gave the same results for each step, indicating reproducibility of the labeling procedure. The unmodified 30 nm gold particle shows a strong absorption at 525 nm. The attachment of DSNB reporter molecules to the nanoparticle resulted in a red shift of 5 nm. Subsequent adsorption of anti-bovine IgG to the DSNB modified nanoparticle also led to broadening and red shifting of the band to 535 nm indicating nanoparticle surface modification. The extinction maximum of the gold nanoparticle is dependent on the properties of the surrounding environment. Hence, a wavelength shift in its absorption maximum is attributed to adsorption-induced changes in the medium surrounding the nanoparticle^{6, 50}.

SERS. In order to gain further insight into the adsorption-induced differences, the modified gold nanoparticles were probed with Raman spectroscopy. Raman spectrum of powdered DSNB is presented in Figure 3.06A. Characteristic bands in the spectrum are the strong symmetric nitro stretch at 1332 cm^{-1} , aromatic ring mode at 1558 cm^{-1} and succinimidyl N-C-O stretch at 1079 cm^{-1} .²³ The band at 851 cm^{-1} is assigned to the nitro scissoring vibration. Adsorption of DSNB onto 30 nm gold nanoparticles results in about a 9-fold increase in signal which is attributable to the SERS effect as shown in Figure 3.06B. Subsequent addition of 7 μL anti-

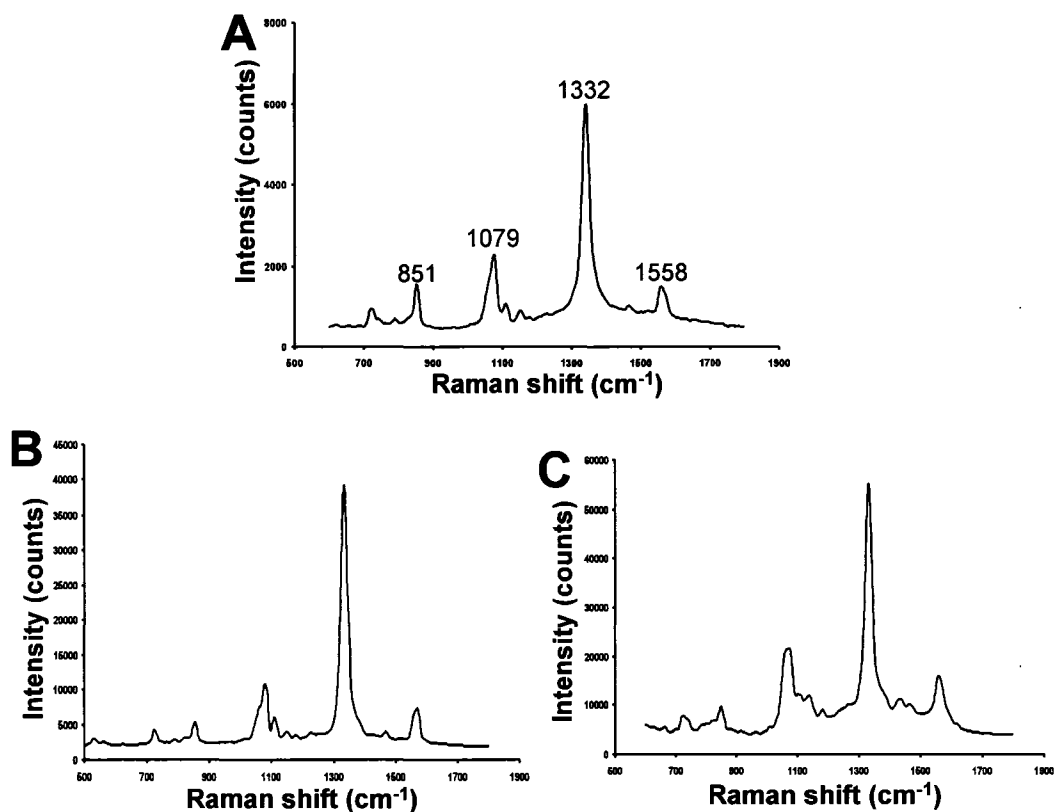


Figure 3.06. Raman spectroscopic stepwise characterization of nanoparticle labeling procedure. (A) Spectrum of powdered DSNB molecule. (B) SERS spectrum of DSNB-modified nanoparticles. Optical image of patterned nanoparticle-labeled target arrays on modified gold surface. (C) Spectrum showing abIgG adsorption to DSNB-modified gold nanoparticles. SERS spectra were obtained using 785 nm laser and integration time of 10 s.

bovine IgG to the DSNB-labeled nanoparticles is presented in Figure 3.06C. Figure 3.06C shows that attachment of the antibody to DSNB labeled nanoparticles does not influence the SERS spectrum. Simple geometrical calculations showed that there are approximately 6,000 – 7,000 DSNB molecules per gold nanoparticle indicating that antibodies were indeed conjugated to the nanoparticles. The Raman results presented in this section shows the effectiveness of our modification scheme and further confirms that shifts in adsorption maxima of the nanoparticles were attributable to adsorption-induced changes.

We could not use SERS to verify the presence of anti-bovine IgG (abIgG) in the labeling scheme due to the reasons stated earlier in this chapter. Hence, IRRAS was employed to investigate the attachment of the anti-bovine IgG to the DSNB via an amide linkage within the spectral region of 2100 to 900 cm^{-1} . In this spectral range, proteins and peptides exhibit characteristic amide bands. The amide I band (C=O stretch) appears in the region from 1650 to 1680 cm^{-1} and amide II band (combination of C-N stretch and N-H bend) is generally located at 1550 cm^{-1} . Amide III bands also occur in the vicinity of 1240 cm^{-1} resulting from N-H bending and are weakly absorbing compared to the amide I and amide II bands. Conditions used for the nanoparticle modification were maintained for sample preparation for the IRRAS. Figure 3.07 shows a monolayer on a planar gold substrate of DSNB formed from a solution of

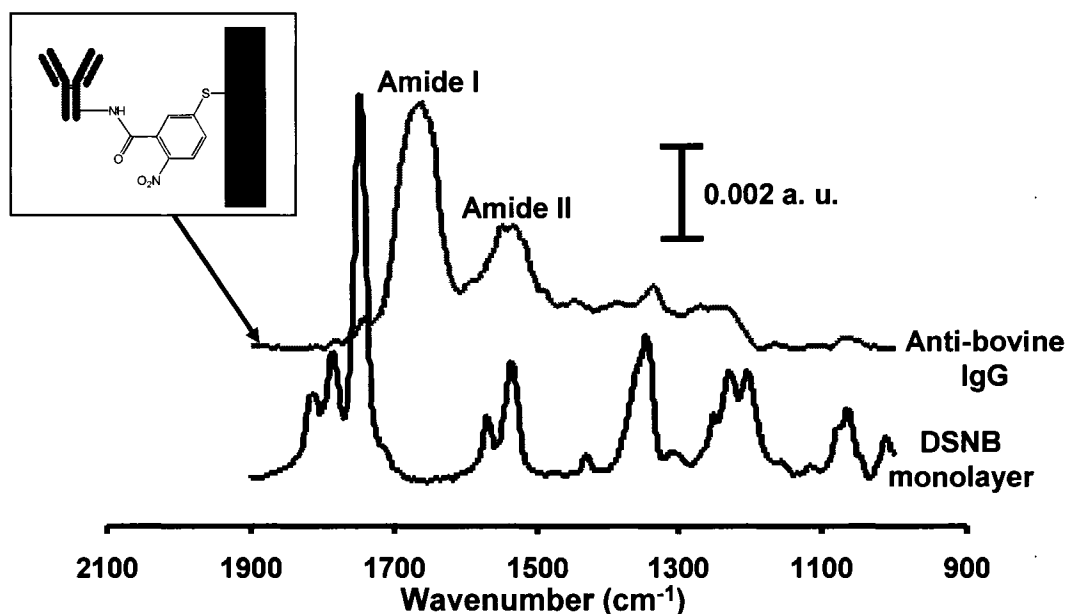


Figure 3.07. IRRAS investigation of anti-bovine IgG (ablgG) adsorption to DSNB-modified planar gold substrate. IRRAS spectra showing the adsorption of DSNB film to planar gold substrate and that of anti-bovine IgG adsorbed onto DSNB-modified gold substrate. Amide I and II indicate the presence of ablgG adsorption. Inset is a cartoon presentation of adsorption of DSNB moiety to planar gold substrate and subsequent attachment of the antibody. IRRAS resolution used was 2 cm^{-1} .

2.5 mM. Strong carbonyl stretches were observed at 1814, 1788 and 1748 cm^{-1} as well as symmetric and asymmetric nitro stretches at 1342 and 1534 cm^{-1} respectively. 2 h adsorption of a 160 $\mu\text{g/mL}$ solution of anti-bovine IgG to DSNB-modified planar gold substrate resulted in the aBlgG spectrum in Figure 3.07. The presence of amide I and II bands at positions 1662 and 1543 cm^{-1} respectively indicates the adsorption of anti-bovine IgG. The disappearance of DSNB monolayer bands in the aBlgG spectrum shows complete coverage of the protein. These results collectively confirm the effectiveness of our labeling scheme. After the confirmation of the attachment scheme, we then proceeded to address the question of the number of antibodies per particle.

Quantitative Determination of Nanoparticle-Bound Antibodies. The objective was to chemically disassemble the labeled structure by etching out the gold nanoparticle core followed by analysis of the protein left behind. The procedure for the determination of the number of anti-bovine IgG molecules attached to each nanoparticle was adopted from published reports based on the use of gold nanoparticles as templates for the synthesis of hollow polymeric capsules.^{12, 52-55} Addition of 100 μL of 0.072 M KCN solution to 1 mL of aBlgG-modified nanoparticle solution (10^{10} particles/mL) led to color transition from red to brown. The brown coloration indicates the formation of a gold-cyanide complex ($\text{Au}(\text{CN})_2^+$). Repeated dialysis followed by centrifugation was necessary for the

purification of the anti-bovine IgG protein. Spectroscopic determination based on Bradford assay was performed on both anti-bovine IgG standards and samples. Figure 3.08 shows the calibration curve obtained from five (5) standard anti-bovine IgG solutions. The absorbance measurement for the anti-bovine IgG sample was 0.341 ± 0.002 a.u. The extrapolation and calculation of resulting antibody sample concentration gave the number of antibodies as 37 ± 3 ($n = 3$) per nanoparticle.

Spectroscopic Reading of Protein Microarrays. An array of protein antigens was prepared by introduction of bIgG solutions of different concentrations (67, 134, 333, 667 and 1340 nM) through PDMS channels interfaced to an AUT modified gold substrate (Figure 3.03). Surface plasmon resonance imaging has shown that the surface density of adsorbed IgG can be controlled by the concentration of protein in solution.⁴⁶ The array surface between the antigen lines was blocked with 0.1 % BSA for 1 h. Solutions of aBlgG labeled nanoparticles (10^{10} particles/mL) were delivered to the antigen lines through a set of perpendicular microfluidic channels. The reading of the arrays was carried out by examining the individual spots on the chip. Figure 3.09 shows an optical image of the array and Raman spectra collected at different spots on the array surface. Figure 3.09B is a spectrum collected from the space between two spots on the array and no appreciable signal was recorded. The intense spectrum measured in the regions where the antibody delivery

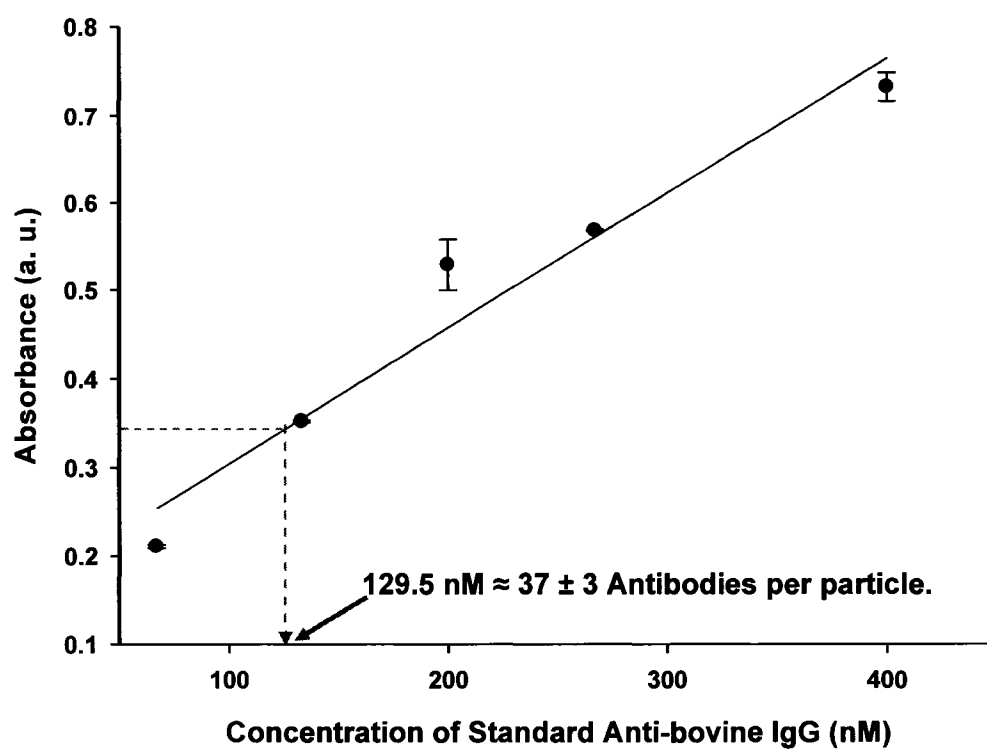


Figure 3.08. Quantitation of the number of antibodies per nanoparticle.

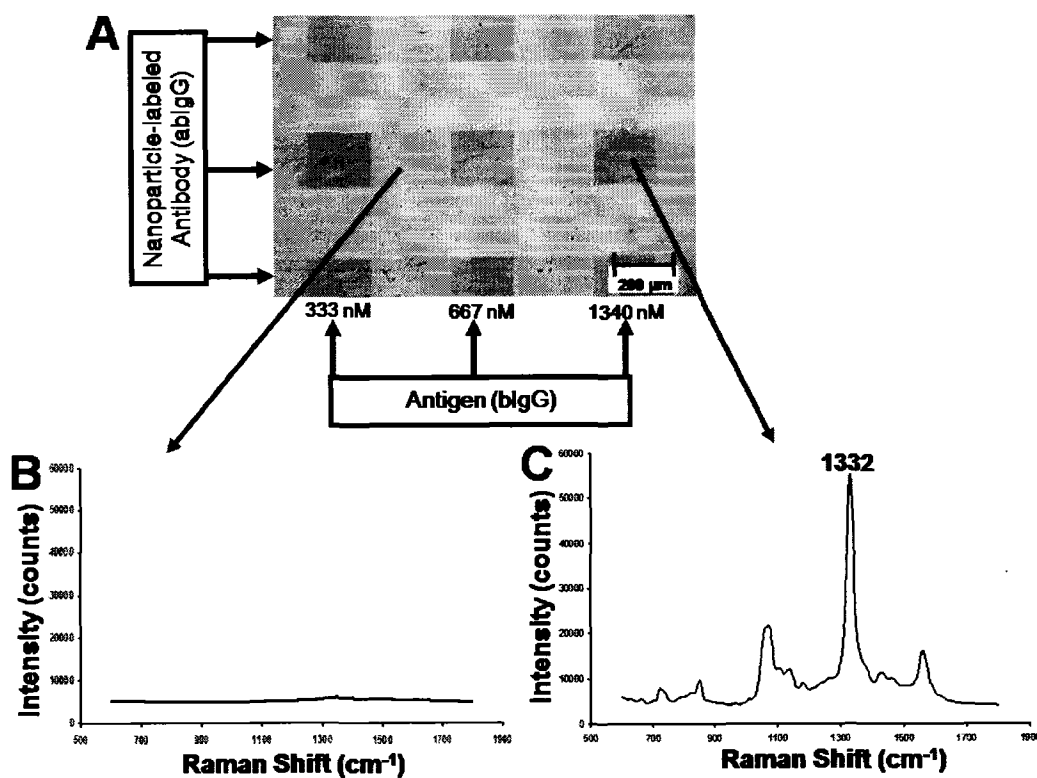


Figure 3.09. Spectroscopic reading of protein microarrays. (A) Optical image showing protein microarrays obtained after patterning of both antigen and nanoparticle-labeled antibody on modified planar gold substrate via μ FCs. Surface density of antigen varied by concentration in solution. concentration and a fixed antibody concentration used to form patterns. (B) SERS spectrum of region outside spots. (C) SERS spectrum collected from a region inside a spot. All spectra collected at integration time of 10 s.

microchannels intersected with the patterned antigen lines corresponds to the SERS spectrum of DSNB shown in Figure 3.09C. Thus, each spot represents a specific site for an antigen-antibody recognition event. Parallel reading of the arrays was accomplished using Raman mapping as described next.

Mapping of Protein Microarrays. Raman mapping provides a two dimensional readout of the two-dimensional array. For the array in Figure 3.09, mapping was employed to investigate the effect of antigen surface concentration on the SERS signal intensity. Raman maps have been used in a number of studies to reveal chemical contrast involving varying samples especially pharmaceutical products.⁵⁶⁻⁵⁹ Figure 3.10A is a SERS map generated using the intensity of the symmetric NO₂ stretch (1332 cm⁻¹) of the DSNB reporter molecule to generate the contrast. As noted above, the surface density of the antigen was varied by delivering different solution concentrations of bovine IgG to the chip surface. Concentrations indicated below the map were those used to pattern the antigens on the chip surface. The lighter pixels indicate regions where more intense Raman scattering at 1332 cm⁻¹ was recorded. The dark background is an indication of high surface selectivity of our array fabrication method. This observation situates Raman mapping as a useful tool for biomolecule array reading. Figure 3.10B is the horizontal cross-sectional profile of antigen-antibody binding spots in Figure 3.10A. This result illustrates that the

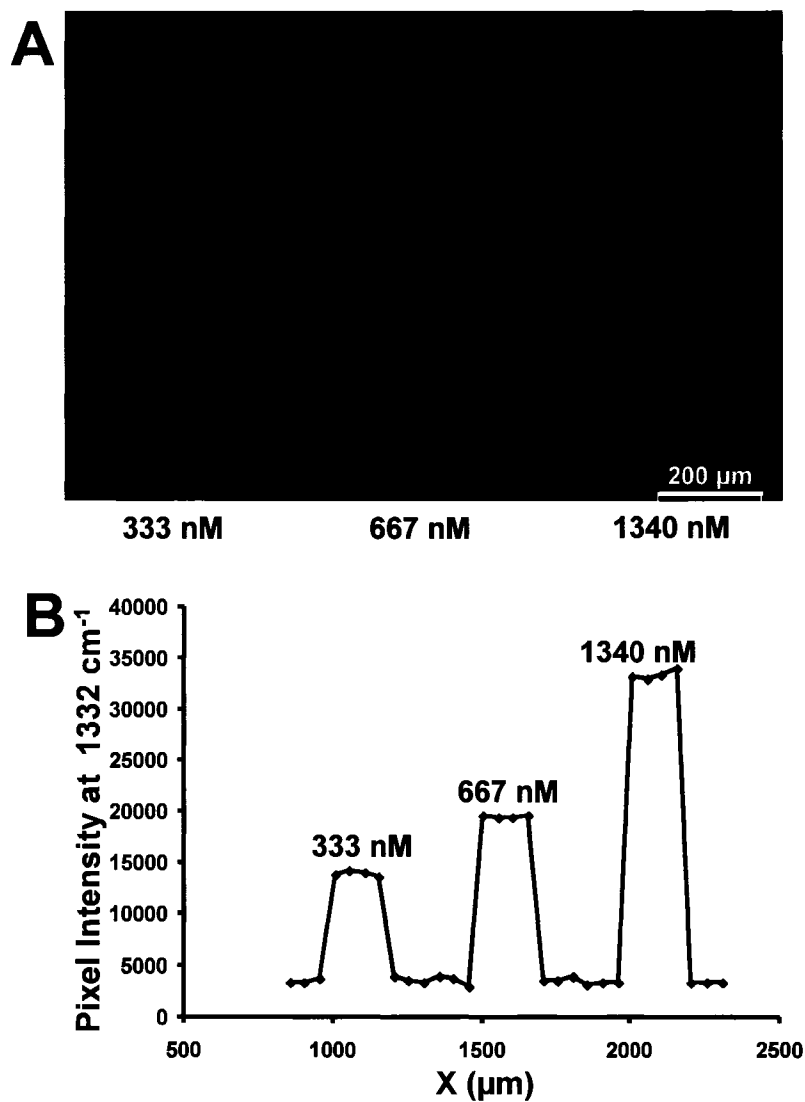


Figure 3.10. Spectroscopic reading of protein microarrays. (A) Raman map showing intensity at 1332 cm^{-1} band with $50\ \mu\text{m}$ step size. Variation in intensity due to differences in antigen concentration. (B) Horizontal cross-sectional profile of antigen-antibody binding from (A).

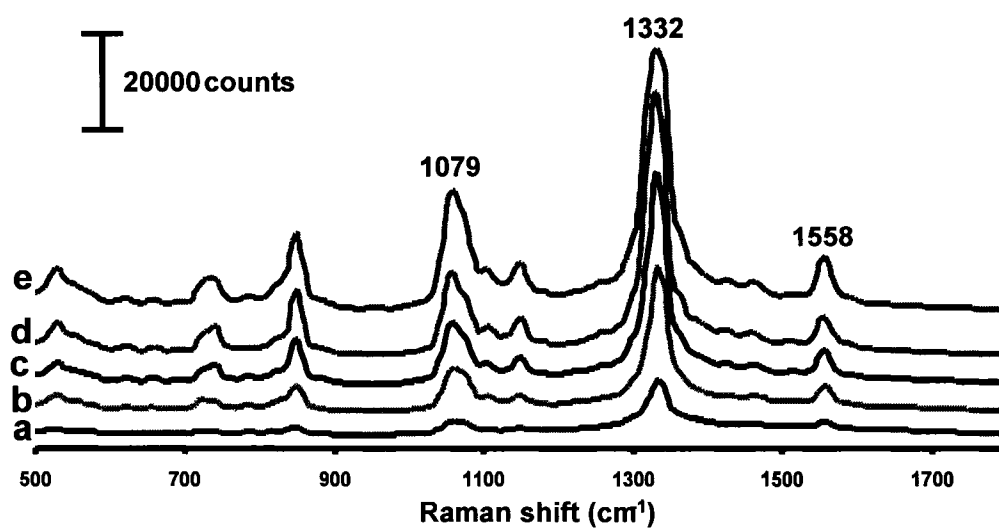


Figure 3.11. SERS investigation of the effect of antigen surface concentration. (A) SERS spectra for different immobilized antigen concentrations of (a) 67 nM, (b) 134 nM, (c) 333 nM, (d) 667 nM and (e) 1340 nM. All spectra collected at 10 s integration time.

[IgG] (nM)	Intensity at 1332 cm⁻¹ (counts)	Particle Count within 300 nm x 300 nm area
67	9.86 ± 0.10 x 10 ³	21 ± 2 ^b
134	2.91 ± 0.01 x 10 ⁴	24 ± 2
333	4.29 ± 0.02 x 10 ⁴	25 ± 2
667	5.33 ± 0.04 x 10 ⁴	28 ± 2
1340	5.72 ± 0.05 x 10 ⁴	30 ± 2

a: For intensity measurements, the average value and standard deviation for 5 measurements is reported in all cases.

b: Reported values are average values and standard deviations of 10 measurements each within 300 nm x 300 nm area for each SEM micrograph.

Table 3.1. Spectroscopic measurements of the intensities of 1332 cm⁻¹ band of DSNB-labeled immunogold nanoparticle on different antigen surface densities.

measurement is quantitative with antigen surface density.

The individual SERS spectra collected from spots with different antigen concentrations ranging from 67 to 1340 nM after adsorption of nanoparticle-labeled anti-bovine IgG on the chip are presented in Figure 3.11. The measured peak intensities at 1332 cm^{-1} for the different immobilized antigen concentrations are presented in Table 3.1. The plotted intensities versus antigen solution concentration in Figure 3.13A show that antigen concentration correlates with the SERS intensity. Also shown in the table are the corresponding particle densities obtained from SEM images collected from the same spots where SERS spectra in Figure 3.12 were taken. SEM images of the lowest and highest antigenic concentrations are presented in Figures 3.12A and 3.12B respectively. On the average of 8 to 10 SEM images were collected for each spot and particles counted from twelve $300 \times 300\text{ nm}^2$ areas demarcated on each image. Visual inspection suggests that there are more clusters on Figure 3.12A than 3.12B.

Nanoparticle clusters have been shown to produce regions of intense electric field known as “hot-spots” which are responsible for an increase in observed SERS intensities.^{60, 61} That is, aggregation of nanoparticle into larger clusters leads to an increase in the magnitude of the dipole induced in each component of the multi-component nanoparticle system (that is amplification of polarization). Focusing light of an

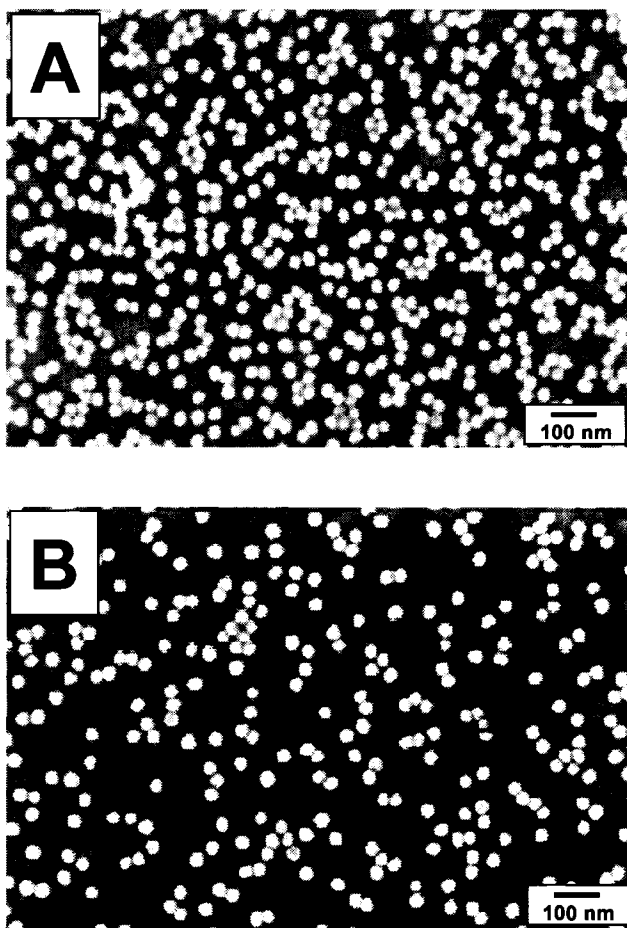


Figure 3.12. SEM investigation of the effect of antigen surface concentration. (A) SEM image of substrate with highest antigen concentration (1340 nM). (B) SEM image showing substrate with the least antigen concentration (67 nM).

appropriate wavelength at the interstitial sites, the exciting electric field vector becomes polarized along the interparticle axis. Thus, fractal clusters formed from nanoparticles by aggregation provides very high SERS enhancement levels. The particle counts presented in Table 3.1 are the averages of ten measurements. Results presented in Figure 3.13B shows that nanoparticle density scales with SERS intensity. Together, these results indicate that as antigen concentration increases, the interaction between the nanoparticle surface bound antibodies and the immobilized antigens maximizes, more nanoparticle clusters are formed which enhance the SERS signals.

Selectivity in SERS Measurements. To further test our array procedure, we examined the selectivity in our antigen-antibody system. The selectivity of the antibody labeled nanoparticles was probed with two experiments. In the first experiment, two different proteins were initially patterned on the array: bovine IgG and lysozyme. Figure 3.14A is an optical image of the array following nanoparticle delivery. Superimposed on the optical image is the Raman map of the 1332 cm^{-1} band. The maps show that lysozyme spots yield darker contrast compared to bovine IgG spots. The spectra of Figure 3.14 B and C provide further evidence for selectivity. The spectrum on the lysozyme line (Figure 3.14B) exhibits bands that are 79% less than on the bovine IgG lines (Figure 3.14C). Thus, the anti-bovine IgG conjugated to the gold nanoparticles maintains

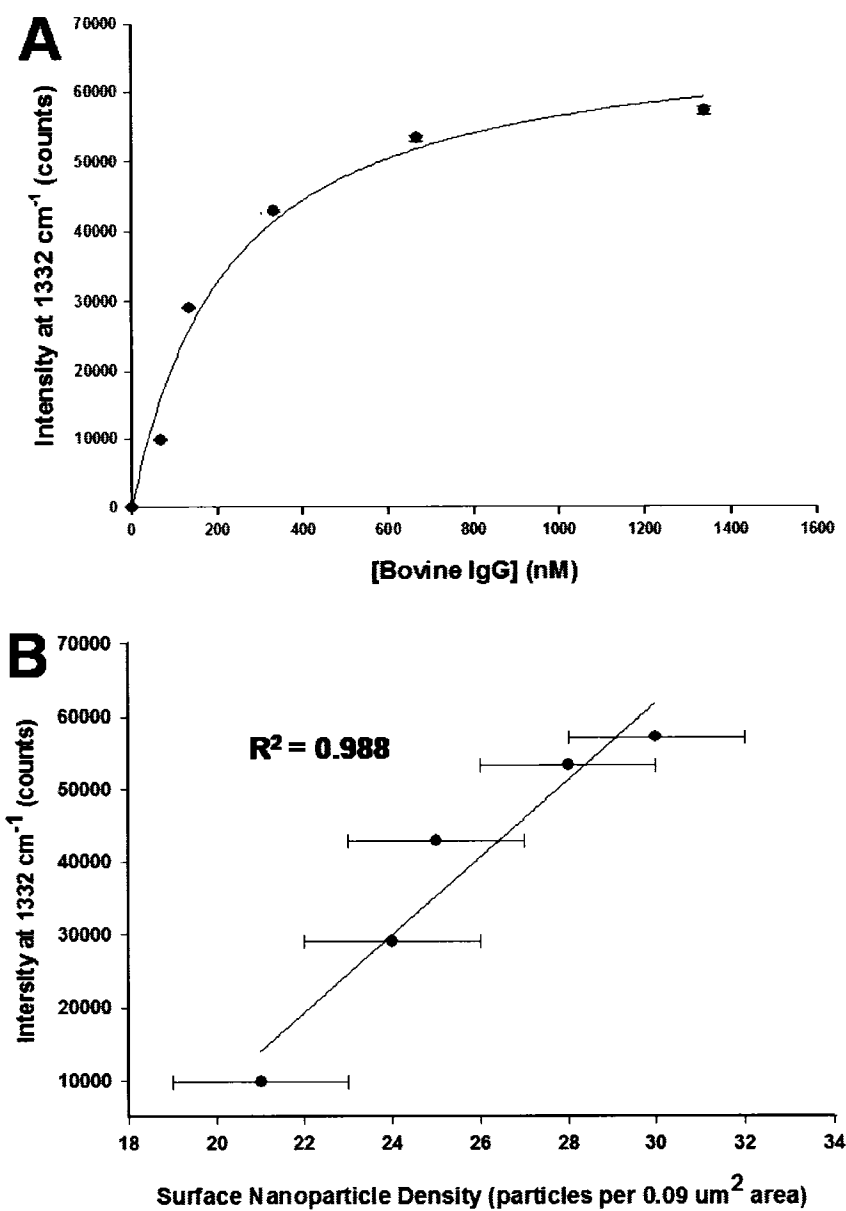


Figure 3.13. Plots showing variations of: (A) concentration of antigen concentration; and (B) nanoparticle surface density with the intensity of 1332 cm⁻¹ band. Plotted values are those shown in Table 3.1.

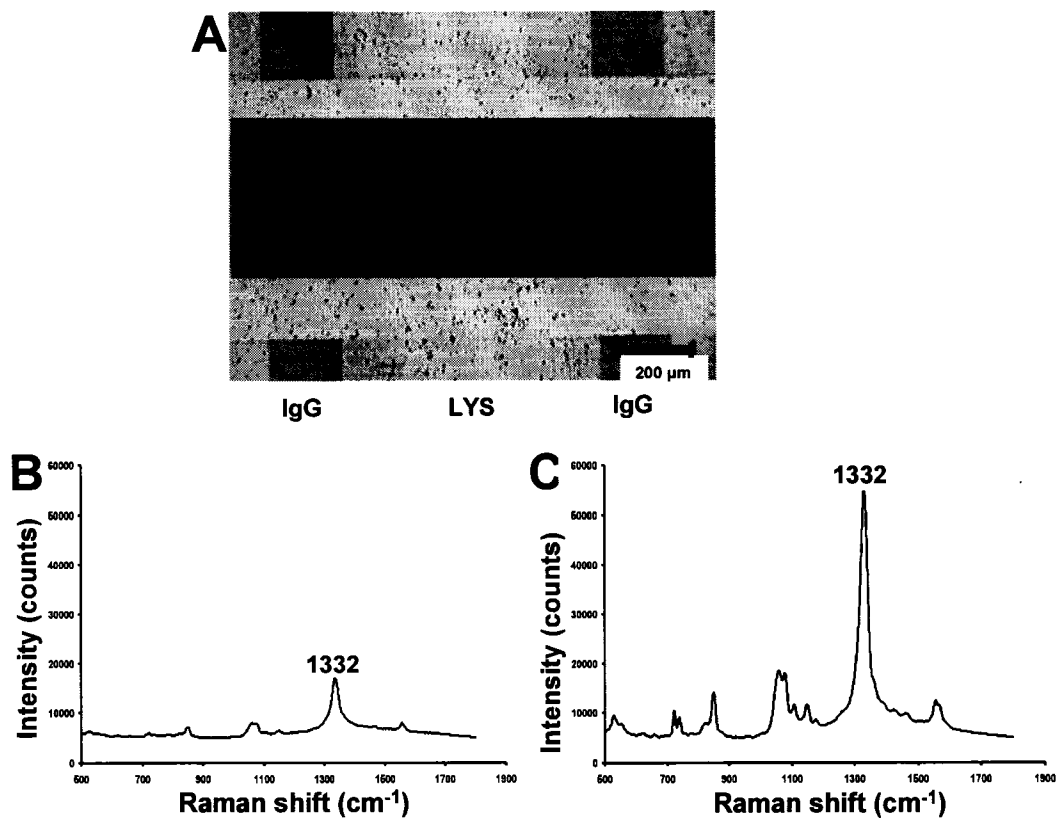


Figure 3.14. Demonstration of selectivity in measurements using different immobilized antigens. (A) Optical image and Raman map of bovine IgG and lysozyme (LYS) arrays. (B) SERS spectrum from LYS spot. (C) SERS spectrum of IgG spot in the array. The dark nature of the LYS region on the map indicates that selectivity is governed by specific antigen-antibody interaction. Map was generated using the 1332 cm^{-1} symmetric nitro band. SERS spectra were obtained using 785 nm laser and integration time of 10 s.

its specificity to its antigen. The low detectable signal from lysozyme clearly demonstrates that specific antigen-antibody interactions govern the selectivity in our detection scheme.

Further evidence of selectivity in the array fabrication was provided by using nanoparticles modified with different antibodies: anti-bovine IgG and anti-SMA. Anti-SMA is an antibody to disaccharide salmonella epitope. Figure 3.15A shows both the optical image and Raman map for nanoparticles delivered to an bovine IgG array. The darker contrast of the anti-SMA spot on the map suggests minimal non-specific binding to the antigenic bovine IgG. SERS spectra collected from both anti-blgG spot (spectrum 2) and that of anti-SMA (spectrum 1) are shown in Figure 3.15B. Negligible SERS signal recorded on the anti-SMA spot further confirms the selectivity of the probe bovine IgG towards the target anti-bovine IgG. These results also show that microarrays with high specificity for biomolecular interactions can be fabricated using PDMS microfluidic networks and read with SERS. The unique advantage of this biomolecule array in discriminating against non-specific interactions is manifested by the affinity between the immobilized blgG and its antibody.

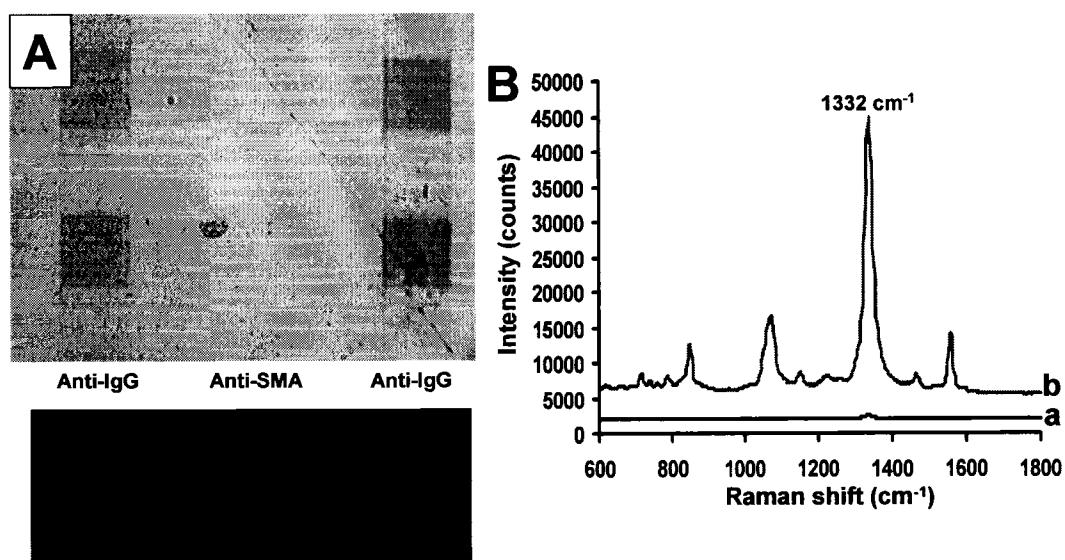


Figure 3.15. Further evidence of selectivity in antigen-antibody measurements using different immobilized antibodies. (A) Optical image and Raman line map of anti-SMA and anti-bovine IgG arrays generated from 1332 cm⁻¹ band. (B) SERS spectra from anti-SMA line (spectrum a) and anti-bovine IgG line (spectrum b). SERS spectrum was obtained using 785 nm laser and integration time of 10 s.

Conclusion

We have shown a simple but highly specific approach to the fabrication and reading of protein microarrays based on the use of microfluidic channels formed in PDMS and SERS detection. To the best of our knowledge, this is the first time SERS-based protein microarray of this nature has been fabricated using μ FC in PDMS. 100 protein arrays were fabricated in this study but given the enormous capabilities of our fabrication procedure, it has the potential of producing well above 150 or more spots. Raman reporter molecules can be combined with nanoparticles for sensitive SERS detection of biological binding. In addition, the use of Raman mapping as a viable readout method for array chips has been demonstrated with interesting quantitative binding events observed with the nanoparticle system. The use of extrinsic Raman labeling in our protocol provided spectral features with minimal overlap which enable the reading of the protein arrays and easy detection of protein-protein interactions. Raman mapping combined with SEM provided both quantitative and qualitative analysis of labeled antibody-antigen complex on modified gold surface.

References

- (1) Fleischmann, M; Hendra, P. J.; McQuilla, A. J. *Chemical Physics Letters* **1974**, *26*, 163-166.

- (2) Kneipp, K.; Kneipp, H.; Itzkan, I.; Dasari, R. R.; Feld, M. S. *Current Science* **1999**, *77*, 915-924.
- (3) Nabiev, I.; Chourpa, I.; Manfait, M. *Journal of Raman Spectroscopy* **1994**, *25*, 13-23.
- (4) Vo-Dinh, T.; Stokes, D. L.; Griffin, G. D.; Volkan, M.; Kim, U. J.; Simon, M. I. *Journal of Raman Spectroscopy* **1999**, *30*, 785-793.
- (5) Vo-Dinh, T.; Yan, F.; Wabuyeke, M. B. *Surface-Enhanced Raman Scattering: Physics and Applications* **2006**, *103*, 409-426.
- (6) Suh, J. S.; Moskovits, M. *Journal of the American Chemical Society* **1986**, *108*, 4711-4718.
- (7) Nabiev, I. R.; Savchenko, V. A.; Efremov, E. S. *Journal of Raman Spectroscopy* **1983**, *14*, 375-379.
- (8) Podstawka, E.; Ozaki, Y.; Proniewicz, L. M. *Applied Spectroscopy* **2004**, *58*, 570-580.
- (9) Xiao, Y. J.; Chen, Y. F.; Wang, T.; Gao, X. X. *Langmuir* **1998**, *14*, 7420-7426.
- (10) Zhao, H. Y.; Yi, N.; Wei, J.; Luo, P. P.; Huang, M. Z.; Yin, G. Z.; Dou, X. M. *Science in China Series B-Chemistry* **2005**, *48*, 240-245.
- (11) Carey, P. R. *Journal of Raman Spectroscopy* **1998**, *29*, 7-14.
- (12) Caruso, F.; Schuler, C. *Langmuir* **2000**, *16*, 9595-9603.
- (13) Deckert, V.; Zeisel, D.; Zenobi, R.; Vo-Dinh, T. *Analytical Chemistry* **1998**, *70*, 2646-2650.
- (14) Caswell, K. K.; Mahtab, R.; Murphy, C. J. *Journal of Fluorescence* **2004**, *14*, 407-415.

- (15) El Amri, C.; Baron, M. H.; Maurel, M. C. *Spectrochimica Acta Part a-Molecular and Biomolecular Spectroscopy* **2003**, *59*, 2645-2654.
- (16) Jung, Y. M.; Sato, H.; Ikeda, T.; Tashiro, H.; Ozaki, Y. *Spectrochimica Acta Part a-Molecular and Biomolecular Spectroscopy* **2004**, *60*, 1941-1945.
- (17) Wu, Y. Q.; Zhao, B.; Xu, W. Q.; Li, B. F.; Jung, Y. M.; Ozaki, Y. *Langmuir* **1999**, *15*, 4625-4629.
- (18) Weldon, M. K.; Zhelyaskov, V. R.; Morris, M. D. *Applied Spectroscopy* **1998**, *52*, 265-269.
- (19) Weldon, M. K.; Morris, M. D. *Applied Spectroscopy* **2000**, *54*, 20-23.
- (20) Rohr, T. E.; Cotton, T.; Fan, N.; Tarcha, P. J. *Analytical Biochemistry* **1989**, *182*, 388-398.
- (21) Dou, X.; Takama, T.; Yamaguchi, Y.; Yamamoto, H.; Ozaki, Y. *Analytical Chemistry* **1997**, *69*, 1492-1495.
- (22) Driskell, J. D.; Kwart, K. M.; Lipert, R. J.; Porter, M. D.; Neill, J. D.; Ridpath, J. F. *Analytical Chemistry* **2005**, *77*, 6147-6154.
- (23) Grubisha, D. S.; Lipert, R. J.; Park, H. Y.; Driskell, J.; Porter, M. D. *Analytical Chemistry* **2003**, *75*, 5936-5943.
- (24) Kim, J. H.; Kim, J. S.; Choi, H.; Lee, S. M.; Jun, B. H.; Yu, K. N.; Kuk, E.; Kim, Y. K.; Jeong, D. H.; Cho, M. H.; Lee, Y. S. *Analytical Chemistry* **2006**, *78*, 6967-6973.
- (25) Moreno-Bondi, M. C.; Alarie, J. P.; Vo-Dinh, T. *Analytical and Bioanalytical Chemistry* **2003**, *375*, 120-124.
- (26) Ni, J.; Lipert, R. J.; Dawson, G. B.; Porter, M. D. *Analytical Chemistry* **1999**, *71*, 4903-4908.

- (27) Xu, S. P.; Ji, X. H.; Xu, W. Q.; Li, X. L.; Wang, L. Y.; Bai, Y. B.; Zhao, B.; Ozaki, Y. *Analyst* **2004**, *129*, 63-68.
- (28) Vo-Dinh, T. *Trac-Trends in Analytical Chemistry* **1998**, *17*, 557-582.
- (29) Lyon, L. A.; Keating, C. D.; Fox, A. P.; Baker, B. E.; He, L.; Nicewarner, S. R.; Mulvaney, S. P.; Natan, M. J. *Analytical Chemistry* **1998**, *70*, 341r-361r.
- (30) Lee, P. C.; Meisel, D. *Journal of Physical Chemistry* **1982**, *86*, 3391-3395.
- (31) Kneipp, K.; Kneipp, H.; Manoharan, R.; Hanlon, E. B.; Itzkan, I.; Dasari, R. R.; Feld, M. S. *Applied Spectroscopy* **1998**, *52*, 1493-1497.
- (32) Shipway, A. N.; Lahav, M.; Gabai, R.; Willner, I. *Langmuir* **2000**, *16*, 8789-8795.
- (33) Stuart, D. A.; Haes, A. J.; Yonzon, C. R.; Hicks, E. M.; Van Duyne, R. P. *IEE Proceedings - Nanobiotechnology* **2005**, *152*, 13-32.
- (34) Vo-Dinh, T.; Yan, F.; Wabuyele, M. B. *Journal of Raman Spectroscopy* **2005**, *36*, 640-647.
- (35) Bello, J. M.; Stokes, D. L.; Vodinh, T. *Applied Spectroscopy* **1989**, *43*, 1325-1330.
- (36) Bello, J. M.; Stokes, D. L.; Vodinh, T. *Analytical Chemistry* **1989**, *61*, 1779-1783.
- (37) Docherty, F. T.; Clark, M.; McNay, G.; Graham, D.; Smith, W. E. *Faraday Discussions* **2004**, *126*, 281-288.
- (38) Graham, D. J.; Price, D. D.; Ratner, B. D. *Langmuir* **2002**, *18*, 1518-1527.

- (39) Carey, P. R. *Journal of Raman Spectroscopy* **1998**, *29*, 861-868.
- (40) Pham, T.; Jackson, J. B.; Halas, N. J.; Lee, T. R. *Langmuir* **2002**, *18*, 4915-4920.
- (41) Angenendt, P.; Glöckler, J.; Konthur, Z.; Lehrach, H.; Cahill, D. J. *Analytical Chemistry* **2003**, *75*, 4368-4372.
- (42) MacBeath, G.; Schreiber, S. L. *Science* **2000**, *289*, 1760-1763.
- (43) Gillis, E. H.; Gosling, J. P.; Sreenan, J. M.; Kane, M. *Journal of Immunological Methods* **2002**, *267*, 131-138.
- (44) Gosling, J. P. *Clinical Chemistry* **1990**, *36*, 1408-1427.
- (45) Yakovleva, J.; Davidsson, R.; Lobanova, A.; Bengtsson, M.; Eremin, S.; Laurell, T.; Emneus, J. *Analytical Chemistry* **2002**, *74*, 2994-3004.
- (46) Kanda, V.; Kariuki, J. K.; Harrison, D. J.; McDermott, M. T. *Analytical Chemistry* **2004**, *76*, 7257-7262.
- (47) Disley, D. M.; Cullen, D. C.; You, H. X.; Lowe, C. R. *Biosensors & Bioelectronics* **1998**, *13*, 1213-1225.
- (48) Riboh, J. C.; Haes, A. J.; McFarland, A. D.; Yonzon, C. R.; Van Duyne, R. P. *Journal of Physical Chemistry B* **2003**, *107*, 1772-1780.
- (49) Xia, Y. N.; Whitesides, G. M. *Annual Review of Materials Science* **1998**, *28*, 153-184.
- (50) Stuart, D. A.; Haes, A. J.; Yonzon, C. R.; Hicks, E. M.; Duyne, R. P. V. *IEEE Proceedings- Nanotechnology* **2005**, *152*, 13-32.
- (51) Wang, Z. X.; Lee, J.; Cossins, A. R.; Brust, M. *Analytical Chemistry* **2005**, *77*, 5770-5774.

- (52) Gittins, D. I.; Caruso, F. *Advanced Materials* **2000**, *12*, 1947-1952.
- (53) Wu, M. L.; O'Neill, S. A.; Brousseau, L. C.; McConnell, W. P.; Shultz, D. A.; Linderman, R. J.; Feldheim, D. L. *Chemical Communications* **2000**, 775-776.
- (54) Marinakos, S. M.; Novak, J. P.; Brousseau, L. C.; House, A. B.; Edeki, E. M.; Feldhaus, J. C.; Feldheim, D. L. *Journal of the American Chemical Society* **1999**, *121*, 8518-8522.
- (55) Marinakos, S. M.; Shultz, D. A.; Feldheim, D. L. *Advanced Materials* **1999**, *11*, 34-37.
- (56) Yang, H. F.; Yang, Y.; Liu, Z. M.; Zhang, Z. R.; Shen, G. L.; Yu, R. Q. *Surface Science* **2004**, *551*, 1-8.
- (57) Sasic, S.; Clark, D. A.; Mitchell, J. C.; Snowden, M. J. *Analyst* **2005**, *130*, 1530-1536.
- (58) Pinzaru, S. C.; Pavel, I.; Leopold, N.; Kiefer, W. *Journal of Raman Spectroscopy* **2004**, *35*, 338-346.
- (59) Zhu, T.; Yu, H. Z.; Wang, J.; Wang, Y. Q.; Cai, S. M.; Liu, Z. F. *Chemical Physics Letters* **1997**, *265*, 334-340.
- (60) Xu, H. X.; Aizpurua, J.; Kall, M.; Apell, P. *Physical Review E* **2000**, *62*, 4318-4324.
- (61) Xu, H. X.; Kall, M. *ChemPhysChem* **2003**, *4*, 1001-1005.

CHAPTER IV

CONTROL OF PROTEIN DENSITY ON NANOPARTICLES FOR SERS-BASED IMMUNOASSAYS

Introduction

In Chapter III, a simple approach to fabrication and reading of protein microarrays based on the use of microfluidic channels in PDMS and SERS detection was developed. The assay consisted of anti-bovine IgG which was tethered to the nanoparticle via a bifunctional coupling agent and surface bound bovine IgG. The Raman spectral intensity of the symmetric nitro stretch of the DSNB-modified nanoparticle was used as a diagnostic for biomolecular interactions. The work described herein seeks to probe the binding event and also addresses the possible causes of the higher signals observed in Chapter III. It is also a contribution to an on-going investigation into the effect of Raman reporter labels on the observed signals in immunoassays which use SERS as the readout technique.

Antibodies commonly employed in immunological studies are the immunoglobulin G (IgG) molecules. IgG, the major antibody in serum, can be cleaved into three 50 kD fragments by the proteolytic action of papain (an enzyme that cleaves specific peptide bonds).¹ Two of these fragments bind antigen. They are called F_{ab} (F stands for fragment, ab for antigen binding). The other fragment, called the crystalline fragment (F_c) because it

crystallizes readily, does not bind antigen, but it has other important biological activities. Within each antigenic site, the variable region of the antibody "arm" interacts through weak non-covalent forces with antigen at numerous sites.

Quantitative analyses of antibody-antigen interaction which constitute a type of biochemical binding permit the estimation of measurable quantities such as the concentration of bound antigen as well as binding constants.^{2, 3} The general principle is to measure the concentrations of free and/or bound antigen for a series of antibody-antigen mixtures that have reacted and reached reaction equilibrium. The resulting data are then treated graphically or statistically to determine the desired parameters. Immunoassay binding curves are inherently nonlinear, and require nonlinear curve fitting algorithms for best description of experimental data.⁴⁻⁶ Models used to fit the binding data, including the frequently applied Langmuir equation, usually assume that the number of bound antigen molecules exactly matches the number of bonds created in antibody-antigen complexes.⁶ However, the complex nature of the antibody-antigen interaction raises questions regarding affinity and avidity in immunoassays.⁷ Affinity describes the strength of interaction between antibody and antigen at single antigenic sites.⁸ Avidity is perhaps a more informative measure of the overall stability or strength of the antibody-antigen complex. It is controlled by three major factors: antibody epitope

affinity, the valences of both the antigen and antibody and the structural arrangement of the interacting parts.^{9, 10} Ultimately, these factors define the specificity of the antibody.

Within the past decade, metal nanoparticle-labeled immunoassays have found widespread use.¹¹⁻¹³ Among the metal nanoparticles, gold nanoparticles have attracted attention because of their easy synthesis and their well established thiols and disulfides modification chemistry. For instance, Porter's group has utilized labeled immunogold in a range of applications from pathogen detection to DNA-based immunosensing.¹⁴⁻¹⁷ Recently, they attempted to optimize the experimental conditions of their SERS-based immunogold assays aimed at minimizing nonspecific binding of Raman reporter labels to the captured antibodies.¹⁶ In immunogold assays, for example, the labels used provide high specific binding sites for the capturing biomolecules. Hence, the surface density of the binding sites on the gold nanoparticle likely represents an important determinant of the sensitivity of the immunoassay. This is particularly critical in a multi-analyte sandwich immunoassay that utilizes a single address and SERS as a readout technique. Yet, no systematic evaluation of reporter and nanoparticle surface densities has been conducted to date. In developing immunoassays, prior to validation, all pertinent variables that affect both the sensitivity and selectivity of the assay need to be evaluated.

In this study, the density of antibodies on the surface of nanoparticles was varied by using mixed self-assembled monolayers (SAMs) and varying the nanoparticle solution concentration. Mixed monolayers were formed from two components: one with the ability to bind covalently to the anti-blgG and the other without any interaction with the antibody. By varying the ratio of the SAM component we were able to vary the captured antibody surface density. Quantitative analysis of the binding of the nanoparticle labeled antibodies with immobilized antigens is presented as well as investigation into multivalency of the binding event.

Experimental

Reagents and Materials. All aqueous solutions were prepared using water from a Nanopure (Barnstead, Dubuque, IA) purification system. Gold nanoparticles (30 nm, BBI International, UK) were purchased and used as received. Various aqueous dilutions of the gold nanoparticle solutions from 10^6 to 10^{11} particles/mL were prepared from the stock solution. Buffer solution employed salts from Fisher Scientific Company (Ottawa, ON). Phosphate buffered saline (PBS, pH 7.4) was prepared with reagent grade 1.4 mM KH_2PO_4 and 4.3 mM Na_2PO_4 , 137 mM NaCl and 2.7 mM KCl. 1 mM PBS was used to prepare all protein solutions. Bovine IgG (blgG) and anti-bovine IgG (ablgG) were purchased from ICN Biomedicals (Aurora, Ohio). ablgG and blgG were diluted with PBS to achieve concentrations of

1067 nM and 1340 nM respectively. Bovine serum albumin (BSA) (fraction V, 99% protein) was obtained from Sigma (St. Louis, MO) and prepared to a concentration of 1 mg/mL. 11-amino-1-undecanethiol (AUT) was purchased from Dojindo Laboratories (Kumamoto, Japan). 4-mercaptophenol (4-MP) (97%) was purchased from Sigma-Aldrich (St. Louis, MO) and used as received. 5,5'-Dithiobis(succinimidyl-2-nitrobenzoate) (DSNB) was synthesized following the procedure published by Grubisha et al with slight modifications.¹⁷ An outline of the detailed synthetic procedure was presented in Chapter III.

Substrate Preparation and Fabrication of PDMS Device. Glass slides (Dow Corning, 0211, 18 mm x 18 mm x 1 mm) substrates used were pre-cleaned in piranha solution (1:3 H₂O₂:H₂SO₄) at 90°C for 15 min, rinsed several times with deionized water and dried with argon. All Au coated slides were prepared as discussed in Chapter III. The 10-channelled microfluidic Poly(dimethyl)siloxane (PDMS) stamps were fabricated according to published procedure and cleaned as outlined in Chapter III. Inlet and outlet holes were through-bored in the PDMS device to allow fluid access to the channels when in conformal contact with the substrate. Fluid flow was driven by applying vacuum suction to the outlet while connecting the inlet to a reservoir of solution.

Preparation of Raman Reporter-Labeled Gold Nanoparticles. The procedure and preparation of Raman reporter-labeled gold nanoparticles

with bound antibodies were adopted from Grubisha et al.¹⁷ Details of this procedure given in Chapter III were strictly followed in the studies presented in this chapter. DSNB-modified nanoparticles conjugated to antibodies were patterned on planar gold substrates as indicated in Chapter III using PDMS microfluidic network.

2 mM concentration of thiol solutions of 4-MP was prepared using acetonitrile as solvent. 100 μ L of the thiol solution was added to 1 mL of gold nanoparticles solution at room temperature for 3 - 5 h. After the incubation period, the solution was centrifuged at 10000 rpm for 7 min, resuspended in acetonitrile and centrifuged again. These Raman reporter-labeled nanoparticles were then spotted on planar gold substrates for SERS characterization. 4-MP was used as diluent for DSNB to control the Raman reporter nanoparticle surface density. 2.5 mM concentration of DSNB solutions were used in all experiments involving DSNB.

Substrate Modification and Patterning. The array fabrication and microfluidic patterning methods used has been described in Chapter III. The method relied on the use of gold nanoparticle labeling procedures for the detection of binding affinity. Detailed description of the construction of the protein arrays which involved a three-step process using polydimethylsiloxane (PDMS) microfluidic network was shown in Figure 3.03 of Chapter III. The only difference in the procedure as employed in

this chapter was the use of single antigenic concentration of 1340 nM blgG solution.

Instrumentation: (1) *Surface-Enhanced Raman Scattering (SERS) Measurements.* SERS spectra were recorded with a Renishaw inVia Raman Microscope equipped with high-performance near-IR (HPNIR) diode (785 nm, 1200 V/mm) laser, and a CCD detector. Radiation of 785 nm from air-cooled diode laser was used for excitation. Laser power at the sample was 10 mW. All reported spectra were the results of 10 s accumulations.

(2) *Scanning Electron Microscopy (SEM) Measurements.* SEM images were collected using a Hitachi S4800 FE-SEM system (Hitachi Scientific Equipment, Japan) equipped with ultrahigh resolution, low voltage 10 kV SEM inspection with advanced sample navigation package. The samples were mounted on a sample holder using conductive carbon tape. Uncoated portions of the substrate were painted with carbon glue to minimize charging.

Results and Discussion

Modified Nanoparticle Patterning Scheme. Figure 4.01 shows the patterning procedure employed in this chapter for obtaining binding curves for immobilized antigen proteins and nanoparticle labeled antibodies. This procedure is similar to the steps given in Figure 3.03 of Chapter III. First,

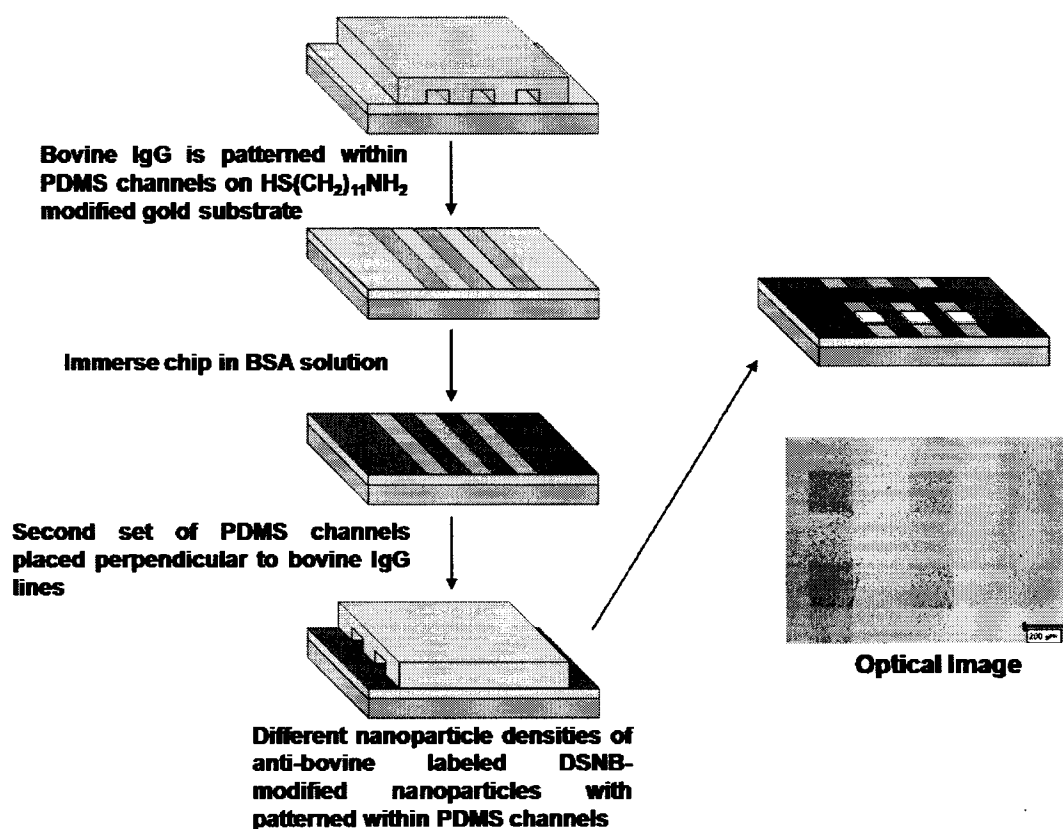


Figure 4.01. Cartoon showing the stepwise microfluidic patterning of different particle densities of anti-bovine IgG labeled DSNB-modified binding possibilities of anti-bovine IgG labeled gold nanoparticle with surface bound antigens.

thin gold film substrates were modified through self-assembly of NH₂-terminated thiol (AUT). Second, the PDMS stamp with microchannels was brought into conformal contact with the AUT-modified planar gold substrate. Solutions of the antigen, bovine IgG (bIgG), in buffer were introduced into the channels for 2 h. During this time the bIgG adsorbed to the NH₂-terminated monolayer. The channels were rinsed with 1 mM PBS buffer and then the PDMS stamp was removed, resulting in a pattern of 200 μ m bovine IgG lines. Next, the entire chip was immersed in a 0.1 % BSA in 1 mM PBS buffer solution for 1 h to block non-specific adsorption. Finally, a second set of μ FCs was placed perpendicularly to the bovine IgG lines and solutions of the antibody labeled nanoparticle with varying particle densities were then delivered across the bovine IgG lines. Solutions were left in the channels for about 12 h but typically the antigen-antibody interaction required only 1-2 h to complete. The interaction between the antibody and antigen caused the nanoparticles to bind to the surface at the intersection of the microfluidic channels and immobilized antigen lines. This results in an array of square spots as shown in the optical image in Figure 4.01.

Effect of Modified Nanoparticle Density. In this investigation, a series of concentrations of nanoparticles labeled with anti-bovine IgG were patterned as discussed in the preceding section. Maximum antigen, bovine IgG, solution concentration of 1340 nM was used since it has been

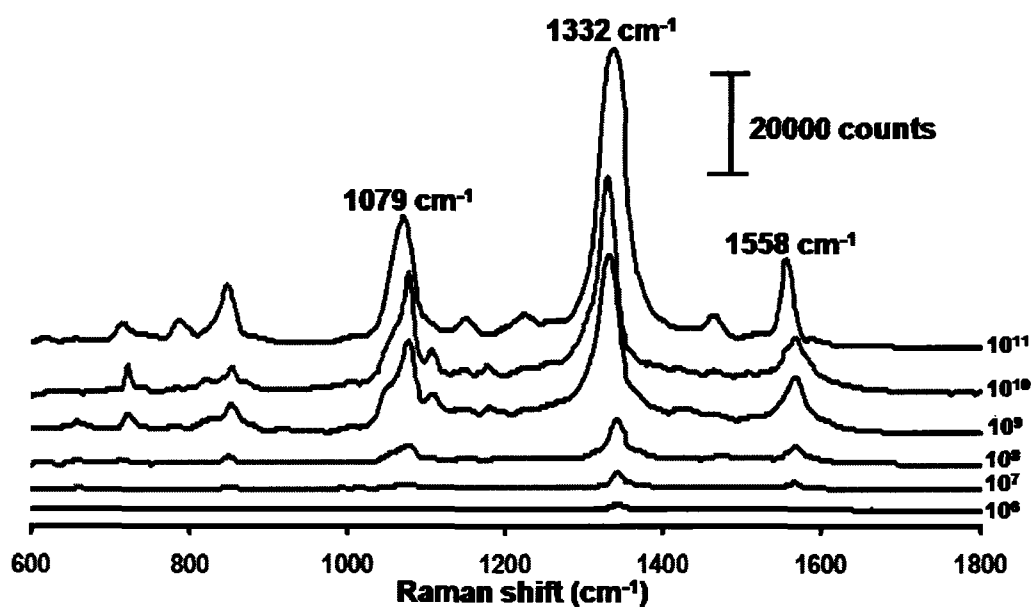


Figure 4.02. SERS spectra for serially diluted anti-bovine IgG bound DSNB-labeled gold nanoparticles with particle concentrations of: (1) 10^6 , (2) 10^7 , (3) 10^8 , (4) 10^9 , (5) 10^{10} and (6) 10^{11} particles/mL. All spectra collected at 10 s integration time.

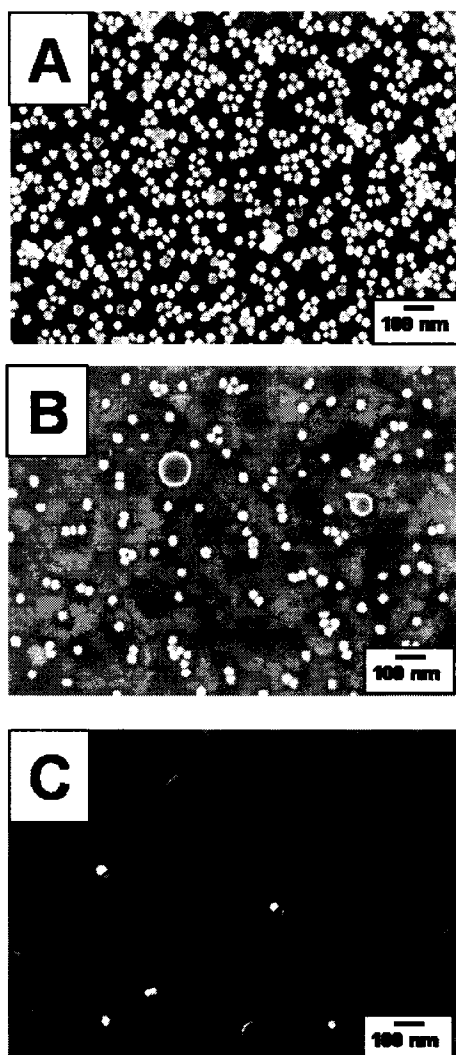


Figure 4.03. Investigation of the effects of DSNB dilution and nanoparticle density. (A) – (C) are scanning electron micrographs showing serial dilutions of 100% DSNB-modified nanoparticles bound to anti-blgG with nanoparticle densities of 10^{11} , 10^9 and 10^7 particles/mL respectively.

Au Particle Density (particles/mL)	Peak Intensity at 1332 cm⁻¹ band (counts)	Particle Count (300 nm x 300 nm)
10¹¹	52582 ± 457^a	60 ± 6^b
10¹⁰	34547 ± 416	41 ± 2
10⁹	25084 ± 225	26 ± 3
10⁸	7189 ± 839	11 ± 2
10⁷	2693 ± 233	4 ± 1
10⁶	875 ± 27	1 ± 0.4

a: For intensity measurements, the average value and standard deviation for 5 measurements is reported in all cases.

b: Reported values are average values and standard deviations of 10 measurements each within 300 nm x 300 nm area for each SEM micrograph.

Table 4.1. Spectroscopic measurements of the intensities of 1332 cm⁻¹ band of serially diluted 100 % DSNB-labeled gold nanoparticles with bound antibody.

previously shown to yield complete surface coverage.¹⁸ Nanoparticle solution concentrations examined in this study range from 10^6 to 10^{11} particles/mL. Figure 4.02 shows the individual SERS spectra collected from spots resulting from the interaction with nanoparticle solutions with concentrations varying from 10^6 - 10^{11} particles/mL. Similar to Chapter III, we will use the intensity of the band for the symmetric NO_2 stretch at 1332 cm^{-1} as a quantitative diagnostic of binding. The measured SERS intensities at 1332 cm^{-1} for the different particle solution concentrations are summarized in Table 4.1. It is apparent that the Raman signal tracks the solution concentration of nanoparticles. This implies that higher solution concentrations result in more particles bound to the surface. This is investigated quantitatively using SEM. Figure 4.03 shows examples of SEM images of regions of spots from the binding of nanoparticles from solutions at concentrations of 10^{11} , 10^9 and 10^7 particles/mL. Visual inspection of the images shows that the particle surface density tracks the solution concentration. Ten images from several spots were analyzed and particle surface densities were determined. These results are also listed in Table 4.1.

The Langmuir adsorption isotherm provides a simple way of determining binding constants for immunoassays by way of fitting the adsorption signal changes to a range of concentrations. A standard Langmuir-type antibody-antigen binding curve would plot the signal for the

amount of antigen bound to the surface versus the solution concentration of the antibody. To calculate the adsorption coefficient, K_{ads} , from the binding curve the x-axis is usually plotted in molar units. The K_{ads} is a parameter that measures the antibody-antigen binding strength. Higher K_{ads} values imply stronger antigen-antibody binding. For our SERS-based immunoassay, we can consider binding curves plotted in two ways with respect to the x-axis. First, we can consider each nanoparticle as a discrete binding entity and calculate the molar concentration of particles in solution. For example, a 10^{11} particles/mL solution is equivalent to 1.67×10^{-10} M or 167 pM.

Figure 4.04 shows binding curves constructed by plotting SERS intensities of the 1332 cm^{-1} band for the varying diluted modified particle solutions versus the nanoparticle solution concentration in pM (comparable to “free antibodies in solution”) and its corresponding logarithmic plot. The data is a fit based on a single site binding model (Langmuir isotherm) shown in equation 4.1 below:

$$y = \frac{K_{ads} B_{max} x}{1 + K_{ads} x} \quad (4.1)$$

where y is the intensity of the symmetric nitro stretch at 1332 cm^{-1} , x is the nanoparticle solution density (“free antibody concentration”), B_{max} is the saturation binding and K_{ads} is the adsorption coefficient. Fitting parameters

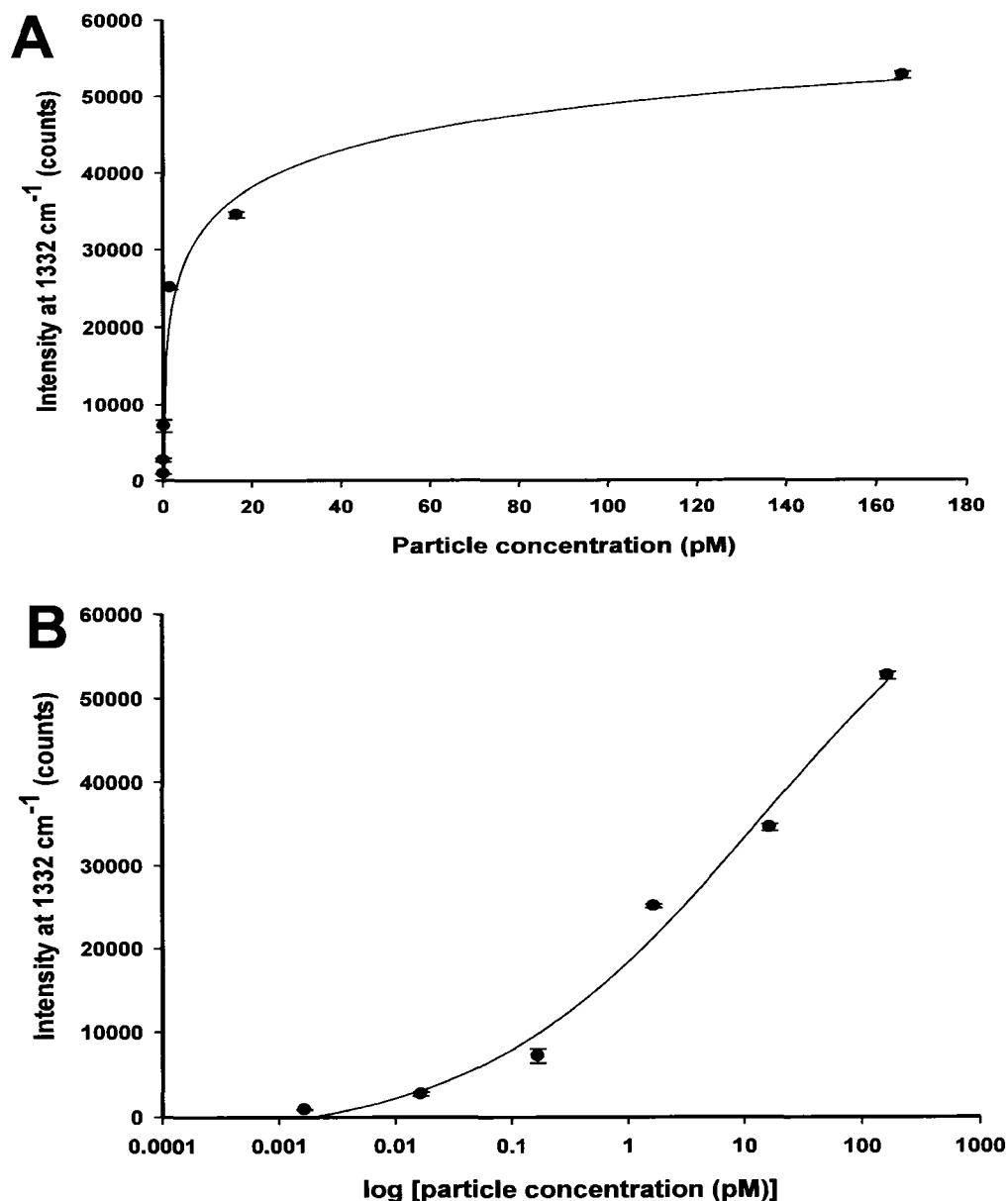


Figure 4.04. Quantitative binding curves showing peak intensity of 1332 cm⁻¹ band of DSNB-modified antibody as a function of (A) nanoparticle solution concentration and (B) log of particle concentration. These are fits with a single-site binding model (Langmuir isotherm) with the use of band intensity as quantitative measure of binding.

% DSNB	B_{max} (counts)	K_{ads} (M⁻¹)	R²
100	46601 ± 352	2.3 ± 0.2 × 10 ¹⁰	0.998

Table 4.2. Curve fitting and calculated parameters for anti-blgG bound DSNB-modified nanoparticles with a series of solutions of increasing particle density exposed to a chip having antigen adsorbed to its surface.

for the binding curve are listed in Table 4.2. In addition, Figure 4.04 also shows a high $R^2 = 0.998$ value indicating a good agreement between the fit and the data.

Although the incomplete binding curve in Figure 4.04B introduces a significant uncertainty in the fitting parameters, we will use the K_{ads} value determined from the fit in the following discussion. The adsorption coefficient, K_{ads} , is a measure of the binding strength of a surface interaction and is often related to the homogeneous association constant (K_a). The interaction between the immobilized bovine IgG and the solution bound anti-bovine IgG was previously investigated in our group in a label-free experiment using SPR imaging. The K_{ads} determined in that study was $1.1 \times 10^7 \text{ M}^{-1}$. The K_{ads} value in Table 4.2 is 10^3 larger than the label-free value. This apparent higher binding constant may be due to the fact that we are considering a single nanoparticle containing about 37 antibodies as equivalent to a single antibody. We can correct the x-axis in Figure 4.04 to express the concentration of antibody in our experiment. This yields a K_{ads} value of $2.3 \times 10^{10} \text{ M}^{-1}$.

The binding curve for this system can also be evaluated by particle counting. SEM images of the chip were collected for each nanoparticle concentration. The surface particle density was calculated and plotted against the log of solution particle concentration. This plot is shown in Figure 4.05B along with the binding curve derived from SERS intensity

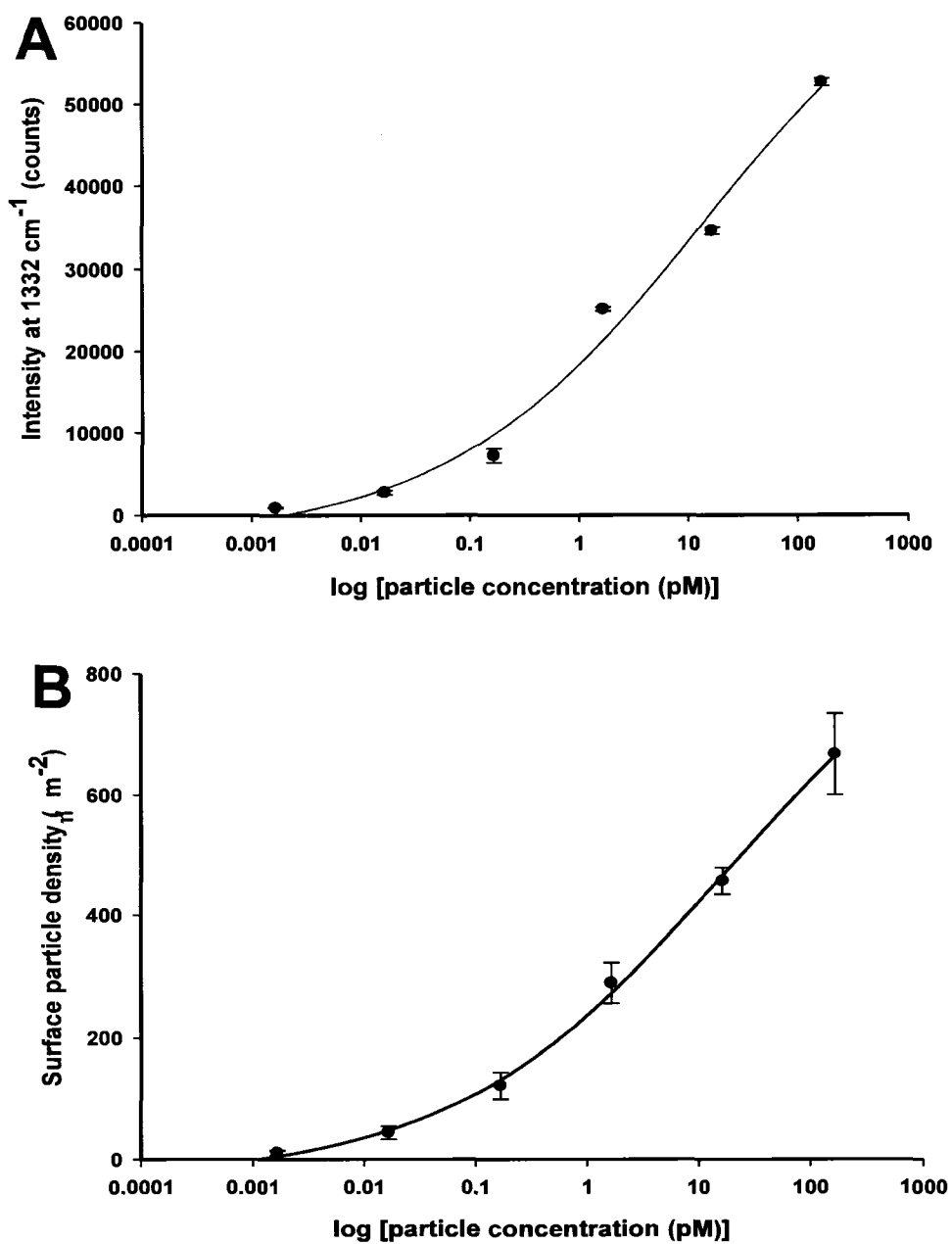


Figure 4.05. Plots of: (A) peak intensity of 1332 cm⁻¹ band of DSNB-modified antibody (filled circles) and (B) surface particle density (filled rectangles) as a function of the log of nanoparticle concentration. These are fits with single-site binding model (Langmuir isotherm).

Plot	B_{\max}	K_{ads} (M^{-1})	R^2
A	46601 ± 352 (counts)	$2.3 \pm 0.2 \times 10^{10}$	0.998
B	604 ± 28 (μm^{-2})	$2.0 \pm 0.4 \times 10^{10}$	0.999

Table 4.3. Curve fitting and calculated parameters for anti-blgG bound DSNB-modified nanoparticles with a series of solutions of increasing particle density exposed to a chip having antigen adsorbed to its surface.

(Figure 4.05A). A closer look at Figure 4.05B reveals that the SEM plot also does not reach saturation. Fitting parameters for the isotherms presented in Figure 4.05 are listed in Table 4.3. The surface particle density and SERS intensity plots gave K_{ads} values of 2.0×10^{10} and $2.3 \times 10^{10} \text{ M}^{-1}$ respectively. Despite the uncertainty in K_{ads} from the incomplete binding curves shown in Figure 4.05, these two analyses still give higher values than label-free SPR method.

Considering our gold nanoparticle labeled system, as nanoparticle surface density increases, regions with higher particle clusters become obvious (Figure 4.06A). The interaction of light of appropriate frequency with these regions of higher particle clusters creates what is known as hot spot.¹⁹ Regions with hot spots have been shown to further enhance the Raman intensity above its expected value. Hence, we have a situation where hot spots can exist. Thus, the observed higher binding constants measured for our SERS system may therefore be affected by signal enhancements inherent from the hot spot regions. However, results presented in Figure 4.04 suggest that the signal response in our system is mainly governed by the specific antibody-antigen interaction. Hence, hot spots do not play a major role in the intensity of our SERS-based immunoassay. The observed higher signals could as well as originate from multivalent interaction (as depicted in Figure 4.06B) which is very predominant in immunoassays. Hence, the higher binding constants for

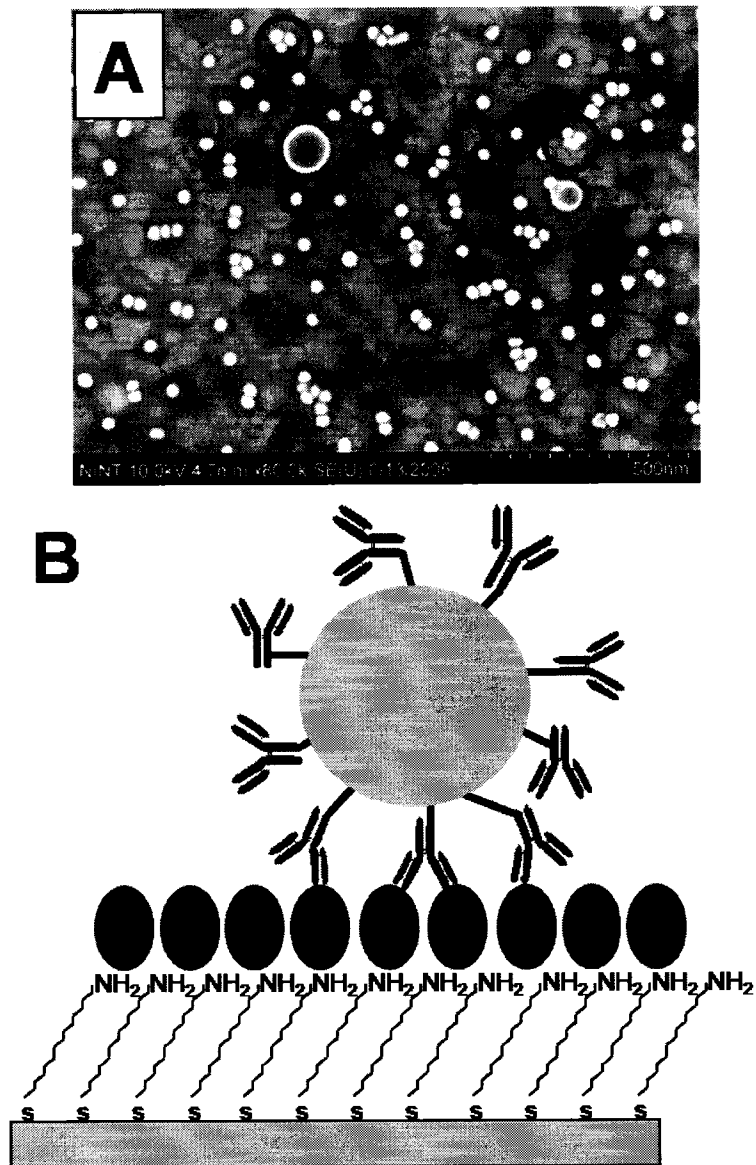


Figure 4.06. (A) SEM image showing regions of particle aggregation (some “hot spots” enclosed by red circles). (B) Cartoon depicting multivalent interactions in an antigen-antibody binding event.

our SERS measurements suggest that multivalent effect originating from multiple antibodies conjugated to each nanoparticle in the antigen-antibody binding might be the major factor responsible for the observed higher signals. Takae et al. have also observed multivalency in their lactose-labeled gold nanoparticles/lectin system.²⁰ However, the approach adopted in this study provides a straightforward way of examining SERS-based binding events. Multivalent interactions, a possible cause of the observed higher binding in our immunoassay, would be further alluded to in the remaining sections of this chapter.

To efficiently probe the antibody-antigen binding interaction, there is the need to control the capture antibody coverage. Surface antibody density was controlled by using a mixed self-assembled monolayer (SAM). The mixed monolayer was prepared from 50:50 percent volumes of DSNB and 4-mercaptophenol (4-MP). The mixed SAM provides a good model for controlling antibody surface density and consequently the antibody-antigen interactions. For example, Dong *et al.* have used mixed monolayers formed from two different components, one with the ability to couple the antibody and the other without specific interaction with antibody, and showed that by varying molar ratio between the two components, antibody coverage could be varied.²¹ However, they observed some nonspecific adsorption in their system because the butanethiol used could not effectively resist protein adsorption.

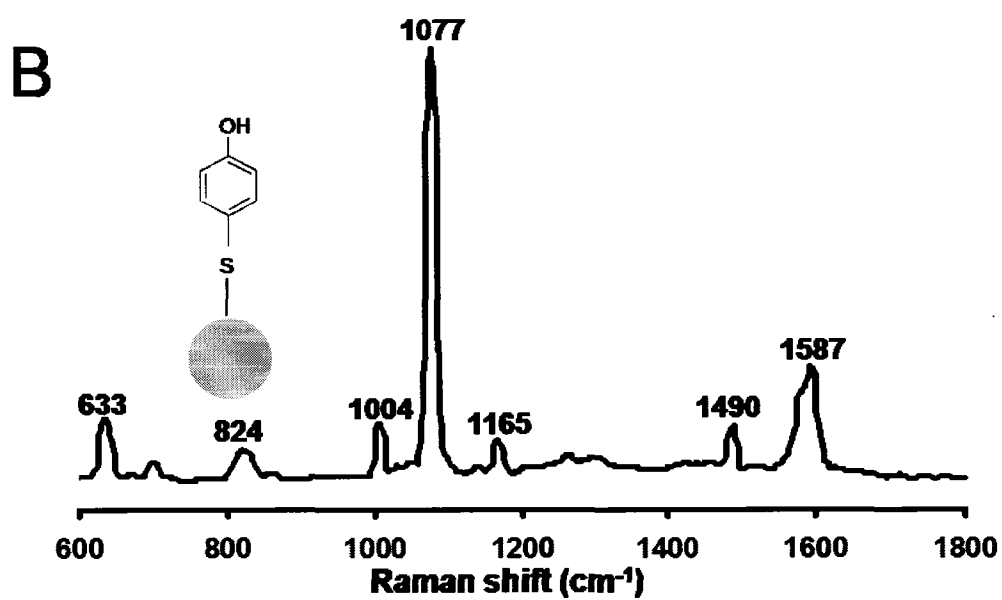


Figure 4.07. SERS spectrum of 4-mercaptophenol (4-MP). 4-MP was used to dilute DSNB based on its spectral features and protein resistance capability.

In this study, 4-MP was chosen because of its capability to resist protein adsorption. Moreover, its aromatic structure compares well with the DSNB moieties. Also, it causes minimum spectral interference with the diagnostic 1332 cm^{-1} symmetric nitro stretch of the DSNB molecule. Figure 4.08 represents the SERS characterization of 4-MP bound to gold nanoparticles in the spectral region between 600 and 1800 cm^{-1} . Several strong aromatic and molecule-specific vibrational bands characteristic of the 4-MP molecule are present within this spectral region. For example, strong aromatic vibrations at 1587 and 1077 cm^{-1} dominate the spectrum. The band at 1490 cm^{-1} is attributable to the in-plane OH bending.²²

Control of Antibody Surface Coverage. The effect of 4-MP on the nanoparticle bound anti-bovine IgG was first examined by determining the number of antibodies bound to each nanoparticle following the nanoparticle etching procedure presented in Chapter III. UV-Vis spectroscopic analysis yielded a value of 16 ± 2 antibodies per gold nanoparticle. This value, although a little less than half of that determined for the undiluted DSNB, confirms that we can control the antibody surface coverage by controlling the DSNB reporter surface density.

Effect of Mixed Monolayer on Antibody Surface Density. To ascertain the influence of surface functionalities on the antibody coverage, a mixed monolayer consisting of solution volumes of 50% DSNB and 50% 4-MP were prepared and immobilized on gold nanoparticles. Nanoparticle

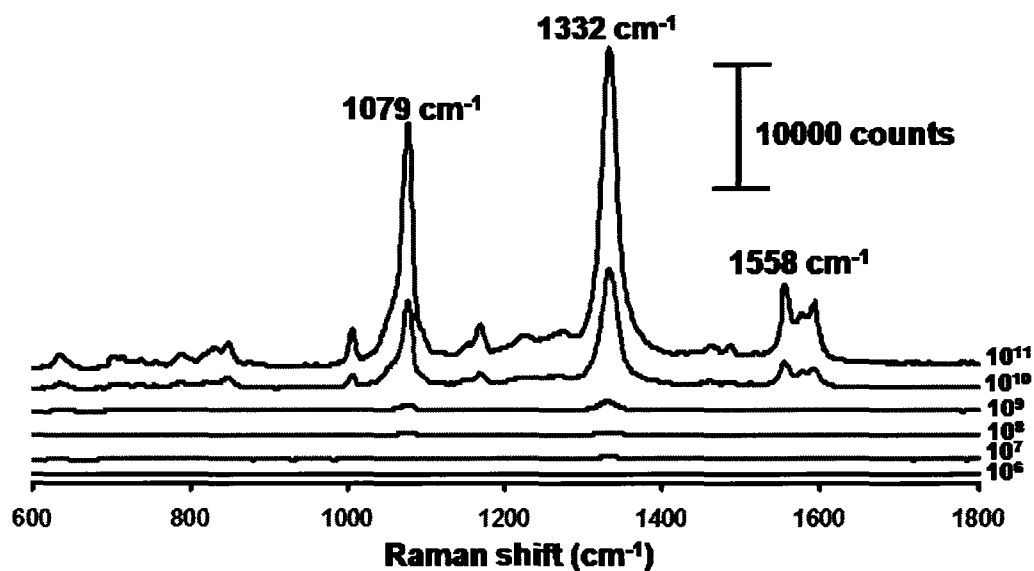


Figure 4.08. SERS analysis of antibody labeled nanoparticle modified with mixed thiols of 50:50 % 4-MP:DSNB and having different nanoparticle densities. SERS spectra indicate anti-bovine IgG labeled gold nanoparticles with particle solution concentrations of: (1) 10^6 , (2) 10^7 , (3) 10^8 , (4) 10^9 , (5) 10^{10} and (6) 10^{11} particles/mL. All spectra collected at 10 s integration time.

solution concentrations ranging from 10^6 to 10^{11} particles/mL were serially prepared as discussed earlier in this chapter. Figure 4.08 presents SERS results of anti-blgG binding on a 1:1 mixed monolayer of 4-MP and DSNB. Again, the SERS signal tracks the solution particle concentration. The Raman signal intensities observed in this case are far lower than those recorded for the undiluted DSNB presented in Figure 4.02 implying that controlling DSNB surface density directly impact the antibody surface coverage. Quantitative analysis of the results based on SEM is presented Figure 4.09. The SEM micrographs shown in Figure 4.09 were examples of images collected from spots resulting from the binding of nanoparticles from solution concentrations of 10^{11} , 10^9 and 10^7 particles/mL to help compare with results presented in Figure 4.03. Careful inspection of the images shows a good correlation between the particle surface density and the nanoparticle solution concentration. Both the SERS measurements and the SEM analysis based on particle surface densities from each spot are listed in Table 4.4. These results again confirm the fact that the number of anti-bovine IgG molecules bound to the nanoparticle surface can be controlled by varying the DSNB reporter surface density. More importantly, together these results further prove that the observed higher SERS signals are direct results of antibody-antigen interaction.

Binding curves similar to those shown in Figure 4.05 were constructed using a fit based on a single-site binding model (Langmuir

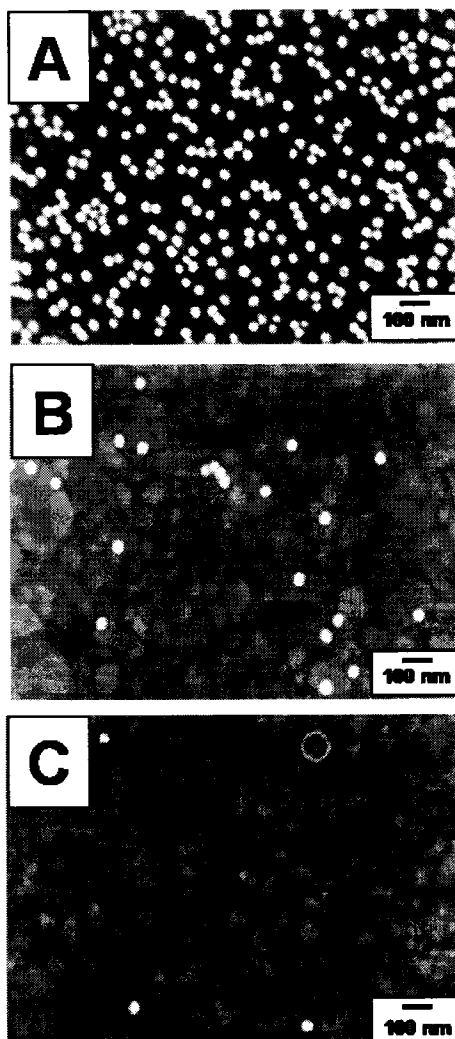


Figure 4.09. Investigation of the effects of DSNB dilution and nanoparticle density. (A) – (C) are scanning electron micrographs showing serial dilutions of 50% DSNB-modified nanoparticles bound to anti-blgG with nanoparticle densities of 10^{11} , 10^9 and 10^7 respectively.

Au Particle Density (particles/mL)	Peak Intensity at 1332 cm⁻¹ band (counts)	Particle Count (300 nm x 300 nm)
10 ¹¹	22043 ± 2627 ^a	47 ± 4 ^b
10 ¹⁰	8721 ± 900	34 ± 9
10 ⁹	773 ± 91	3 ± 2
10 ⁸	253 ± 37	1 ± 0.5
10 ⁷	221 ± 24	0
10 ⁶	44 ± 14	0

a: For intensity measurements, the average value and standard deviation for 5 measurements is reported in all cases.

b: Reported values are average values and standard deviations of 10 measurements each within 300 nm x 300 nm area for each SEM micrograph.

Table 4.4. Spectroscopic measurements of the intensities of 1332 cm⁻¹ band of serially diluted DSNB-labeled gold nanoparticles with bound antibody.

isotherm based on equation 4.1). Figure 4.10A is a plot of the Raman intensity of the symmetric nitro stretch at the 1332 cm^{-1} band versus logarithm of nanoparticle solution concentration. Figure 4.10B, on the other hand, is a fit showing the calculated surface particle density plotted against the solution particle concentration to compare its adsorption coefficient to will be obtained from Figure 4.10A. Fitting parameters for the isotherms presented in Figure 4.10 are listed in Table 4.5.

A number of observations are noteworthy from the logarithmic plots in Figure 4.10. First, the curves presented for the 50% DSNB reach more closely to saturation compared to those obtained from 100% DSNB. The higher R^2 values also indicate a good agreement between the data and the Langmuir fit. Secondly, both the SERS intensity and the surface particle density scale with the solution particle concentration implying that the signal response shows good correlation between amount of bound antibody and the solution concentration of antibody. Thirdly, the surface particle density and SERS intensity plots gave K_{ads} values of 6.2×10^9 and $3.8 \times 10^9\text{ M}^{-1}$ respectively. These K_{ads} values are about ten times magnitude less than those obtained for the undiluted system presented earlier in this chapter but a hundred times higher than the label-free SPR method. This suggests that the stronger antibody-antigen binding in our SERS-based immunoassay and further confirms the fact that the observed higher SERS intensities are mainly governed by these biomolecular

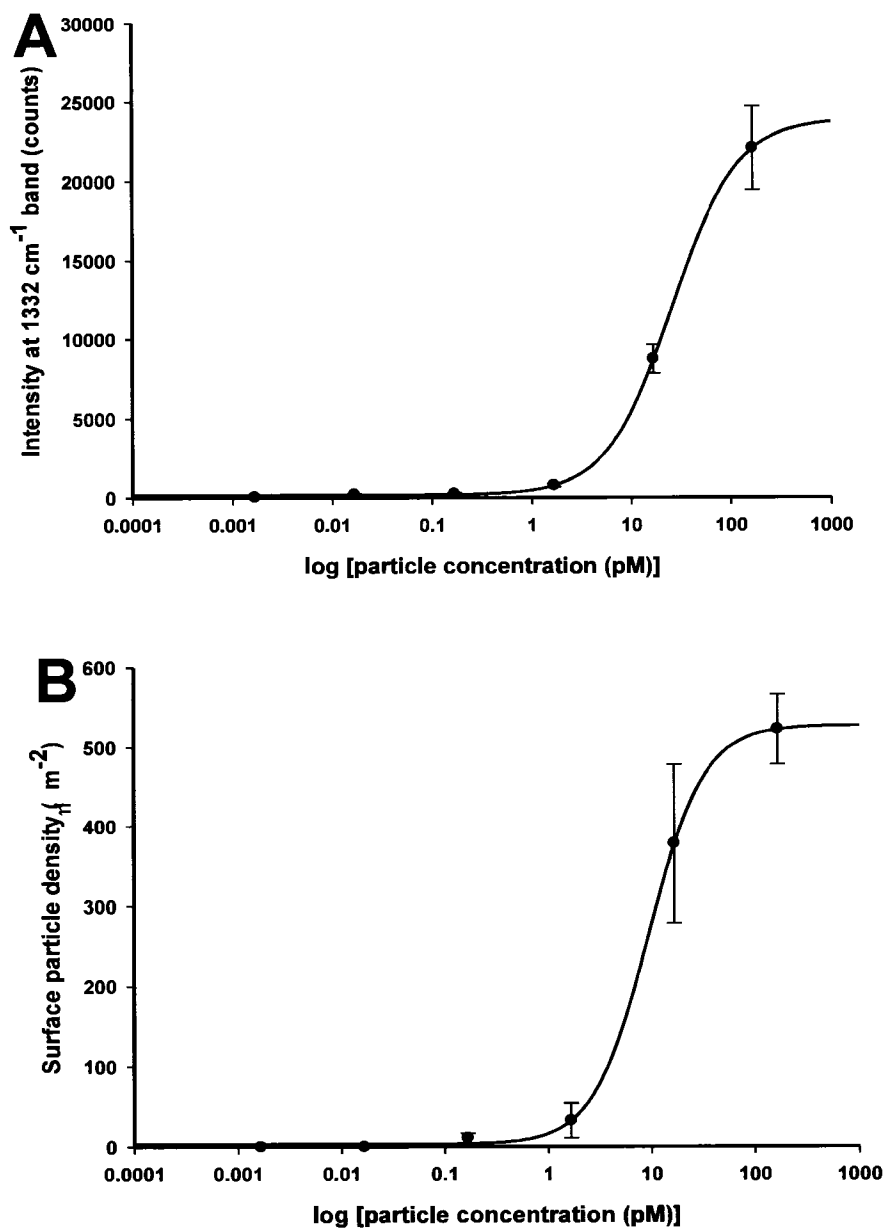


Figure 4.10. Isotherms of antibody labeled nanoparticle of varying nanoparticle solution concentrations and modified with mixed thiols of 50:50 % 4-MP:DSNB. Plots of: (A) peak intensity of 1332 cm⁻¹ band of DSNB-modified antibody (filled circles) and (B) surface particle density (filled rectangles) as a function of the logarithm of nanoparticle concentration. These are fits with single-site binding model (Langmuir isotherm).

Plot	B_{\max}	K_{ads} (M^{-1})	R^2
A	26670 ± 497 (counts)	$3.8 \pm 0.1 \times 10^9$	1.000
B	565 ± 34 (μm^{-2})	$6.2 \pm 0.2 \times 10^9$	0.999

Table 4.5. Curve fitting and calculated parameters for anti-blgG bound DSNB-modified nanoparticles with a series of solutions of increasing particle density exposed to a chip having antigen adsorbed to its surface.

interactions. In summary, these results indicate that antibody molecules bound to the labeled nanoparticles play a crucial role in controlling these biorecognition events in our assay.

Conclusions

A systematic evaluation of a nanoparticle-based immunoassay has been presented. This work has further demonstrated that surface antibody coverage can be controlled by using a mixed self-assembled monolayer formed from DSNB and 4-MP. We have shown that the observed SERS signal might result partly from hot spots and mainly from the multivalent nature of the binding between the captured nanoparticle labeled antibody and the surface-bound antigen. The avidity between the immobilized blgG and its captured antibody increases with nanoparticle solution concentration and this has been demonstrated with interesting quantitative results using SEM. The use of both SERS and SEM surface-based techniques provided a fair assessment of our immunoassay; however, *in situ* Raman measurement needs to be carried out to assess the binding strength of the antibody-antigen complex.

References

- (1) Press, E. M.; Piggot, P. J.; Porter, R. R. *Biochemical Journal* **1966**, *99*, 356-366.

- (2) Lundstrom, I. *Biosensors & Bioelectronics* **1994**, *9*, 725-736.
- (3) Malmborg, A. C.; Michaelsson, A.; Ohlin, M.; Jansson, B.; Borrebaeck, C. A. K. *Scandinavian Journal of Immunology* **1992**, *35*, 643-650.
- (4) Findlay, J. W. A.; Smith, W. C.; Lee, J. W.; Nordblom, G. D.; Das, I.; DeSilva, B. S.; Khan, M. N.; Bowsher, R. R. *Journal of Pharmaceutical and Biomedical Analysis* **2000**, *21*, 1249-1273.
- (5) Haven, M. C.; Orsulak, P. J.; Arnold, L. L.; Crowley, G. *Clinical Chemistry* **1987**, *33*, 1207-1210.
- (6) Dudley, R. A.; Edwards, P.; Ekins, R. P.; Finney, D. J.; Mckenzie, I. G. M.; Raab, G. M.; Rodbard, D.; Rodgers, R. P. C. *Clinical Chemistry* **1985**, *31*, 1264-1271.
- (7) Soukka, T.; Harma, H.; Paukkunen, J.; Lovgren, T. *Analytical Chemistry* **2001**, *73*, 3511-3511.
- (8) Giovannoni, G.; Chapman, M. D.; Thompson, E. J. *Journal of Neuroimmunology* **2006**, *180*, 29-32.
- (9) Marchant, A.; Pihlgren, M.; Goetghebuer, T.; Weiss, H. A.; Ota, M. O. C.; Schlegel-Hauter, S. E.; Whittle, H.; Lambert, P. H.; Newport, M. J.; Siegrist, C. A.; Study, M. R. C. G. T.; *Journal of Infectious Diseases* **2006**, *193*, 1598-1605.
- (10) Hansen, K. R.; Nielsen, L. R.; Lind, P. *Journal of Applied Microbiology* **2006**, *100*, 144-152.
- (11) Seydack, M. *Biosensors & Bioelectronics* **2005**, *20*, 2454-2469.
- (12) Xu, S. P.; Ji, X. H.; Xu, W. Q.; Zhao, B.; Dou, X. M.; Bai, Y. B.; Ozaki, Y. *Journal of Biomedical Optics* **2005**, *10*, 1-15.
- (13) Vo-Dinh, T.; Yan, F.; Wabuye, M. B. *Surface-Enhanced Raman Scattering: Physics and Applications* **2006**, *103*, 409-426.
- (14) Park, H. Y.; Driskell, J. D.; Kwarta, K. M.; Lipert, R. J.; Porter, M. D.; Schoen, C.; Neill, J. D.; Ridpath, J. F. *Surface-Enhanced Raman Scattering: Physics and Applications* **2006**, *103*, 427-446.

- (15) Duhachek, S. D.; Kenseth, J. R.; Casale, G. P.; Small, G. J.; Porter, M. D.; Jankowiak, R. *Analytical Chemistry* **2000**, *72*, 3709-3716.
- (16) Driskell, J. D.; Kwarta, K. M.; Lipert, R. J.; Porter, M. D.; Neill, J. D.; Ridpath, J. F. *Analytical Chemistry* **2005**, *77*, 6147-6154.
- (17) Grubisha, D. S.; Lipert, R. J.; Park, H. Y.; Driskell, J.; Porter, M. D. *Analytical Chemistry* **2003**, *75*, 5936-5943.
- (18) Kanda, V.; Kariuki, J. K.; Harrison, D. J.; McDermott, M. T. *Analytical Chemistry* **2004**, *76*, 7257-7262.
- (19) Aravind, P. K.; Metiu, H. *Surface Science* **1983**, *124*, 506-528.
- (20) Takae, S.; Akiyama, Y.; Otsuka, H.; Nakamura, T.; Nagasaki, Y.; Kataoka, K. *Biomacromolecules* **2005**, *6*, 818-824.
- (21) Dong, Y. Z.; Shannon, C. *Analytical Chemistry* **2000**, *72*, 2371-2376.
- (22) Xia, L. X.; Kim, N. H.; Kim, K. *Journal of Colloid and Interface Science* **2007**, *306*, 50-55.

CHAPTER V

INVESTIGATION OF ADSORPTION CHARACTERISTICS OF FIBRINOGEN ON MODIFIED GOLD SUBSTRATES USING INFRARED REFLECTION ABSORPTION SPECTROSCOPY

Introduction

In the preceding chapters, SERS was used to study the interactions between the nanoparticle-labeled antibody and a surface bound antigen. This chapter will present results from our studies on the adsorption characteristics of human fibrinogen (HFG) on surfaces with well-controlled chemistries using infrared spectroscopy. The surfaces examined in this study provide the experimental basis for exploring fundamental non-covalent intermolecular forces that dominate protein adsorption processes. Comparison will be drawn between fibrinogen and non-specifically adsorbed bovine IgG (blgG) as well as structurally rigid lysozyme (LYS) on a positively-charged amine-modified surface to further understand surface-influence on protein surface coverage.

A complete study of protein adsorption is highly desirable not only for gaining insight into the protein-surface interaction but also for predicting the possibility of using the surface for short- and long-term biomaterial applications. Interaction of proteins with solid surfaces and its related interfacial phenomena have been studied for decades.¹⁻⁵ A lot of effort has gone into understanding the adsorption-desorption kinetics⁶ and

conformational changes associated with adsorbed proteins on solid substrates.^{1, 3, 5, 7} The desire to control and manipulate protein adsorption on surfaces therefore requires a detailed understanding of the adsorption process. Thus, protein adsorption characteristics are usually controlled by varying parameters such as surface chemistry, pH, ionic strength and substrate material.^{8, 9} However, the effect of these factors on the activity of the surface-bound proteins has not been fully understood. It is generally accepted that protein adsorption and subsequent conformational changes are greatly influenced by surface hydrophobicity.^{2, 10} The concomitant effect in the exposure of the interior hydrophobic groups drives attraction between neighboring adsorbed molecules.

Generally, adsorption of protein from solution to modified solid substrates is said to involve five processes.^{1, 3, 11, 12} These include: (1) protein transport to the surface; (2) interaction and attachment to the surface; (3) adsorption; (4) structural and/or orientational rearrangements; and (5) desorption of the protein from the surface. Several techniques including atomic force microscopy (AFM),¹³⁻¹⁵ surface plasmon resonance (SPR),¹⁶ ellipsometry,¹⁷ radioactive labeling and infrared (IR) spectroscopy have been employed to interrogate the adsorption behavior of proteins on surfaces. Although these techniques are powerful and provide valuable information on the state of the adsorbed protein, they are unable to distinguish between the individual protein molecules on the surface. For

example, AFM has been used to observe the morphology and dynamic events of the adsorption process on a molecular scale.^{14, 15, 18} Surface topography of AFM provides information about the surface chemistry of the protein, which correlates to conformational changes and coverage of the adsorbed protein. However, tip contamination, damage of samples and imaging of weakly adsorbed molecules in liquid environment are challenges that need to be addressed. Also, measuring the rate of protein folding has remained elusive. Fourier transform infrared spectroscopy (FTIR) has been used to probe the conformational response of amide groups to changes in their environment which reflect possible changes in the whole protein structure.¹⁹⁻²³ The ability to provide distinct spectral signatures for proteins (amide bands) coupled with information on coverage and conformation response make infrared spectroscopy suitable for the work presented in this chapter.

Among the numerous proteins investigated, fibrinogen has been studied most extensively due to its prominent role in coagulation and its ability to promote platelet adhesion.^{7, 15, 20, 24-28} Fibrinogen is a massive dimeric protein (MW = 340kD) with several molecular domains. The structurally distinguishable regions of the fibrinogen molecule are: a lone central E domain, two distal D domains, two α -helical coiled coils, two α C domains, and a pair of junctions between them.²⁴ At pH 7.4, the E and D domains are hydrophobic and negatively charged while the α C domain is

hydrophilic and positively charged. Thus fibrinogen can interact with surfaces through a variety of mechanisms. For example, although, the overall charge of the molecule is -10 , a negative surface may adsorb through the αC domain.⁷ Fibrinogen is therefore often referred to as a “sticky” protein due its ability to adsorb onto a variety of surfaces. The fibrinogen molecule has been found to exist in different possible orientations and/or conformations depending on the adsorption history and the surface chemistry of the substrate.^{7, 24, 26, 29} Previous studies have shown that, following attachment to a surface, fibrinogen begins to increase its coverage in a manner consistent with unfolding on hydrophobic surfaces and reorientation on hydrophilic substrates.^{20, 26} This suggests that fibrinogen may undergo either reversible or irreversible adsorption upon attachment depending on the substrate surface chemistry.

In the current study, the adsorption of HFG on neutral (polystyrene and 1-undecanethiol (UDT)), positively charged (11-amino-1-undecanethiol (AUT)) and negatively charged (11-mercapto-1-undecanoic acid (MUA)) surfaces was examined by infrared reflection absorption spectroscopy (IRRAS). Polystyrene modified and solution self-assembled thiol monolayer substrates were chosen to effect different surface interactions. Experiments conducted in this study were aimed at evaluating the effect of protein adsorption on solution self-assembled and adsorbed protein substrates. In the following sections, adsorbed protein substrates will be

referred to as pre-HFG substrates. In all cases, protein concentrations were chosen to allow formation of a complete protein film after 1 h.

IRRAS has been used by our group and others to provide information on the adsorbed state of the protein and also as means of quantifying protein adsorption to the surfaces.^{4, 22, 23, 27, 29, 30} Specifically, the intensity of amide II bands has been used to quantify the amount of protein present at the interface.²³ Also, peak shape analysis of amide I has also been used for assigning protein secondary structure or conformation.³¹ Hence, in this chapter, the amide II band intensity will be used as a measure of amount of protein adsorbed to the substrate.

Experimental

Reagents and Materials. All aqueous solutions were prepared using water from a Nanopure (Barnstead, Dubuque, IA) purification system. Buffer solution employed salts from Fisher Scientific Company (Ottawa, ON). Phosphate buffered saline (PBS, pH 7.4) was prepared with reagent grade 1.4 mM KH_2PO_4 and 4.3 mM Na_2PO_4 , 137 mM NaCl and 2.7 mM KCl. 1 mM PBS was used to prepare all protein solutions. All proteins were used as received without further purification. Fraction I 95% clottable human fibrinogen (HFG) was obtained from Sigma (St. Louis, MO). HFG solution concentrations were 14.7, 29.4, 58.8, 147, 294, 441 and 588 nM in 1 mM PBS. Bovine IgG (bIgG) was purchased from ICN Biomedicals

(Aurora, Ohio) and diluted with PBS to achieve concentrations of 14.7 and 588 nM. Chicken lysozyme (LYS) was obtained from Sigma (St. Louis, MO) and prepared to concentrations of 14.7 and 588 nM.

1-undecanethiol [$\text{HS}(\text{CH}_2)_{10}\text{CH}_3$] (UDT) 98% and 11-mercapto-1-undecanoic acid [$\text{HS}(\text{CH}_2)_{10}\text{COOH}$] (MUA) 95% were purchased from Aldrich (Milwaukee, WI) and used as received. 11-amino-1-undecanethiol [$\text{HS}(\text{CH}_2)_{10}\text{CH}_2\text{NH}_2$] (AUT) was purchased from Dojindo Laboratories (Kumamoto, Japan). 1 mM thiol solutions were prepared in anhydrous ethanol (Quantum Chemical Co., Newark, NJ). Polystyrene (PS) was purchased from Aldrich (MW = 45,000 D), dissolved in tetrachloromethane (CCl_4) and 1 mM concentrations were prepared.

Substrate Preparation. The glass substrates used were pre-cleaned in piranha solution (1:3 H_2O_2 : H_2SO_4) at 90°C for 15 min, rinsed several times with deionized water and dried with argon. All glass substrates used in this study were prepared by thermal evaporation of 15 nm adhesive layer of chromium and 200 nm of gold using a thermal evaporation system (Ion International Inc., New Windsor, NY). A vacuum of 4.6×10^{-6} mbar was used for evaporation at a rate of 0.2 Å/sec for Cr and 0.4 Å/sec for Au. Once prepared, the Au slides were rinsed using ethanol and water followed by drying with argon. The substrates were then cleaned in an ozone cleaner (UVO-Cleaner, Model No. 42, Jelight Company Inc., Irvine, CA) for 10 min prior to immersion in thiol solution.

Monolayer Formation and Substrate Modifications. Self-assembled monolayers (SAMs) of UDT, MUA and AUT on Au for infrared reflection absorption spectroscopic studies were prepared from 1 mM ethanolic solutions. Only homogeneous single component monolayers were prepared. UDT and AUT were adsorbed overnight and MUA for 1 h. After the specified assembly time, the slides were removed from solution and rinsed well with ethanol to remove unbound thiols from the surface, and then dried with a stream of argon. A thin film of polystyrene was spin-coated onto gold slide using PWM32 Series Photoresist Spinner (Headway Research, Inc., Texas, USA).

Protein films were formed by immersing the monolayer-modified Au slides in protein solution for 1 h. After the incubation period, the slides were removed from the protein solution, rinsed with 1 mM PBS to remove any unbound protein and dried with a stream of argon.

Infrared Spectra Measurements. IRRAS spectra were collected with a Mattson Infinity FTIR Spectrometer (Madison, WI) equipped with a low-noise mercury-cadmium-tellurium (MCT) detector cooled with liquid N₂ to about 77 K. A reflection accessory and a home-built sample holder housed in an external auxiliary bench were employed. Spectra for modified Au slides with UDT, MUA or AUT monolayer that has been immersed in HFG, LYS and IgG protein solutions were collected. Protein adsorption on a thin film of polystyrene modified gold substrate was also studied. Spectra were

taken at 2 cm^{-1} resolution with a glancing angle of 86° . A self-assembled deuterated octadecanethiol, a gift from Dr. John-Bruce Green (University of Alberta), was used as the background.

Results and Discussions

Surface Characterization. Characterization of a set of surfaces exhibiting systematic variations in surface chemistry is required to effectively determine chemical functionalities responsible for influencing protein adsorption to solid substrates. Infrared spectroscopy has been used in the past to probe the methylene C-H stretches of films formed on gold substrates.³²⁻³⁴ For example, Porter *et al.* observed asymmetric CH_2 stretch at approximately 2918 cm^{-1} for long chain thiols, indicative of crystalline monolayer.³² Shorter chain thiols exhibited a blue shift in their absorption energies. Therefore, IRRAS was employed in this study to ascertain the formation of spin-coated polystyrene film and solution self-assembled thiol monolayers of 1-undecanethiol, 11-mercapto-1-undecanoic acid and 11-amino-1-undecanethiol on gold. The C-H adsorption bands between 2700 and 3200 cm^{-1} spectral region were monitored.

Figure 5.01 shows the infrared spectrum of polystyrene molecules that have been spin coated on a planar gold substrate. Spectral features at positions 3078 , 3058 and 3024 cm^{-1} are characteristic C-H stretching

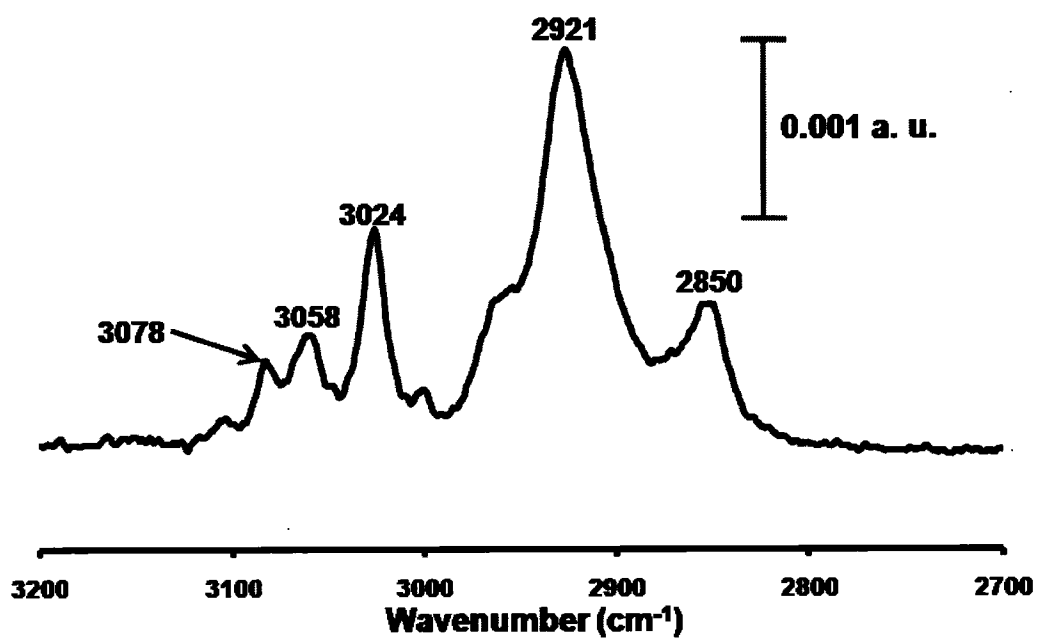


Figure 5.01. IRRAS spectrum of polystyrene on gold substrate. Bands shown are characteristic of C-H stretching modes for monosubstituted benzene ring and alkyl chain of the polymer.

modes for monosubstituted benzene ring.³⁵ The presence of these bands indicates that polystyrene is immobilized onto the gold substrate. Bands at 2921 and 2850 cm^{-1} are the C-H stretching modes for the symmetric and asymmetric CH_2 groups respectively on the alkyl chain of the polymer.

Molecular self-assembled techniques provide an effective means of fabricating organic surfaces with well-defined structure and chemistry. Spectra of Figure 5.02 were realized from substrates modified with 1-undecanethiol ($\text{HS}(\text{CH}_2)_{10}\text{CH}_3$, UDT), 11-mercapto-1-undecanoic acid ($\text{HS}(\text{CH}_2)_{10}\text{COOH}$, MUA) and 11-amino-1-undecanethiol ($\text{HS}(\text{CH}_2)_{10}\text{CH}_2\text{NH}_2$, AUT). These thiols have different chemistries but similar number of methylene units. The CH_2 stretching mode adsorption intensity is directly related to the number of CH_2 units per alkyl group. Assignment of the bands for UDT, MUA and AUT in the C-H stretching region (high frequency region, 2700 to 3200 cm^{-1}) is indicated in Table 5.1. The C-H region describes the chain structure of the monolayer. All the characteristic bands of the monolayers are indicative of crystalline (highly-ordered) chain structures. The values shown in Table 5.1 are indications of relatively dense alkyl chains in crystalline-like environments and are in good agreement with literature results.³² These SAMs were carefully chosen to eliminate the influence of the monolayer structure on the adsorption process whilst presenting varied surface chemistries for protein interaction.

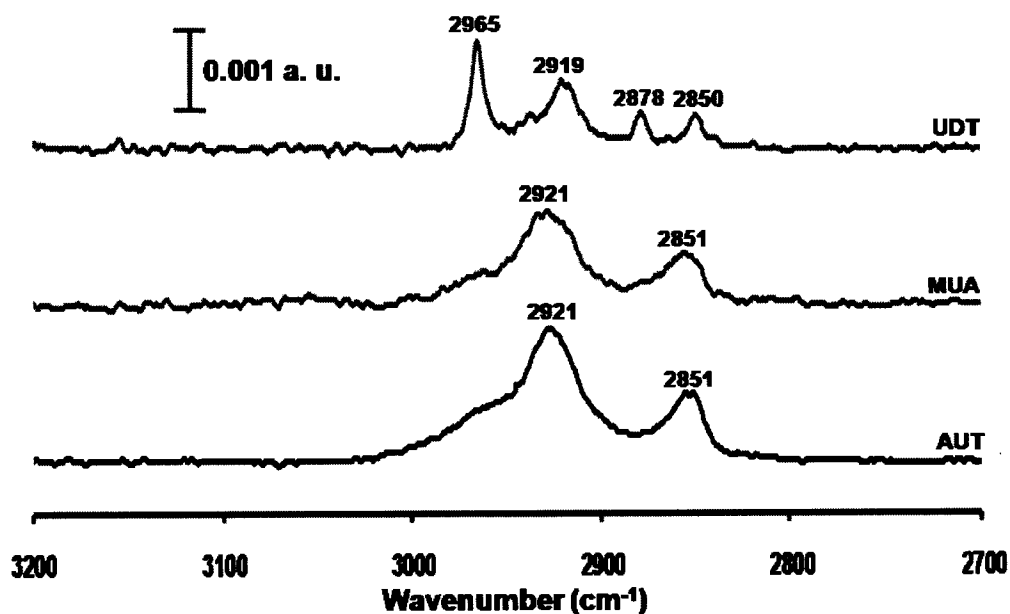


Figure 5.02. FTIR spectra of 1 mM solutions of self-assembled monolayers (SAMs) of UDT (CH₃-terminated), MUA (COOH-terminated) and AUT (NH₂-terminated) adsorbed on gold substrate. C-H stretching frequencies of UDT, MUA and AUT self-assembled monolayers on planar gold substrates are similar to those of polystyrene shown earlier.

Number of Methylene Units (n)	Monolayer	$\nu_s(\text{CH}_2)$ (cm^{-1})	$\nu_a(\text{CH}_2)$ (cm^{-1})	$\nu_s(\text{CH}_3)$ (cm^{-1})	$\nu_a(\text{CH}_3)$ (cm^{-1})
10	UDT	2850	2919	2878	2965
10	MUA	2851	2921	N/A	N/A
11	AUT	2851	2921	N/A	N/A

Table 5.1. C-H stretching frequencies of UDT [$\text{HS}(\text{CH}_2)_{10}\text{CH}_3$], MUA [$\text{HS}(\text{CH}_2)_{10}\text{COOH}$], and AUT [$\text{HS}(\text{CH}_2)_{10}\text{CH}_2\text{NH}_2$] self-assembled monolayers on gold. n denotes the number of CH_2 units that make up the alkyl chain of the monolayer. ν_s and ν_a represent the symmetric and asymmetric stretches respectively. The $\nu_s(\text{CH}_2)$ and $\nu_a(\text{CH}_2)$ are respectively due to the symmetric and asymmetric C-H stretching modes of the CH_2 group of the alkyl chain. However, $\nu_s(\text{CH}_3)$ and $\nu_a(\text{CH}_3)$ are the symmetric and asymmetric C-H stretching modes of the CH_3 group which are present in UDT but absent in both MUA and AUT. N/A means not applicable.

Adsorption of Human Fibrinogen on Modified Substrates. The

discussion in the following section will focus on the effect of surface chemistry on adsorption characteristics of proteins on solid substrates. In all cases, protein concentrations were chosen to allow formation of a complete protein film after 1 h. IRRAS spectra from 2100 to 900 cm^{-1} of adsorbed proteins will be presented. In this spectral range, proteins and peptides exhibit characteristic bands, which are the direct results of vibrations in the amide linkages. The amide I band (C=O stretch) appears in the region from 1650 to 1680 cm^{-1} and the amide II band (combination of C-N stretch and N-H bend) is generally located at 1550 cm^{-1} .^{23, 36-38} Amide I and amide II bands have been used respectively as diagnostic indicators for conformational changes and as a measure of the amount or coverage of adsorbed proteins.^{14, 36-38} Amide III band in the vicinity of 1240 cm^{-1} resulting from N-H bending is weakly absorbing as compared to amide I and amide II. Hence no discussion on this band will be presented.

The absorbance of the amide II band is linearly related to the amount of protein bound to the surface.³⁹ Thus, the intensities of amide II bands serve as useful indicators for protein coverage. Hence, amide II band intensity will be used in this study as a measure of amount of protein adsorbed to the substrate. In addition, adsorbed protein substrates will be referred to as pre-HFG substrates.

Figures 5.03 and 5.04 respectively show the IRRAS spectra collected after 1 h adsorption of 14.7 and 588 nM HFG on polystyrene, UDT, MUA and AUT modified Au substrates. All substrates were rinsed with 1 mM PBS and dried with argon to remove any unbound protein prior to IRRAS analysis. These spectra show two strong absorbances corresponding to the amide I and amide II bands. Table 5.2 presents the summary of the infrared spectroscopic measurements of the amide bands in Figures 5.03 and 5.04. The differences observed in the amide I bands were less than our spectral resolution. In addition, the peak positions of amide II bands for adsorbed HFG on the four surfaces are very similar. This is not surprising since it has been shown that the amide II peak positions are insensitive to the adsorbed state of the protein.²³ The presence of amide bands indicates adsorption of fibrinogen on these different surface chemistries.

The spectra describing the adsorption of 14.7 and 588 nM HFG solutions on a polystyrene/Au substrate are shown in Figures 5.03 and 5.04 respectively. The presence of ring stretching modes from the polystyrene film is an indication of incomplete protein coverage at both concentrations within the 1 h adsorption time used in this study. Analysis of these spectra shows a similar pattern of HFG adsorption on polystyrene and UDT substrates at the two HFG concentrations studied. The methyl and polystyrene substrates are expected to retain significant hydrophobic

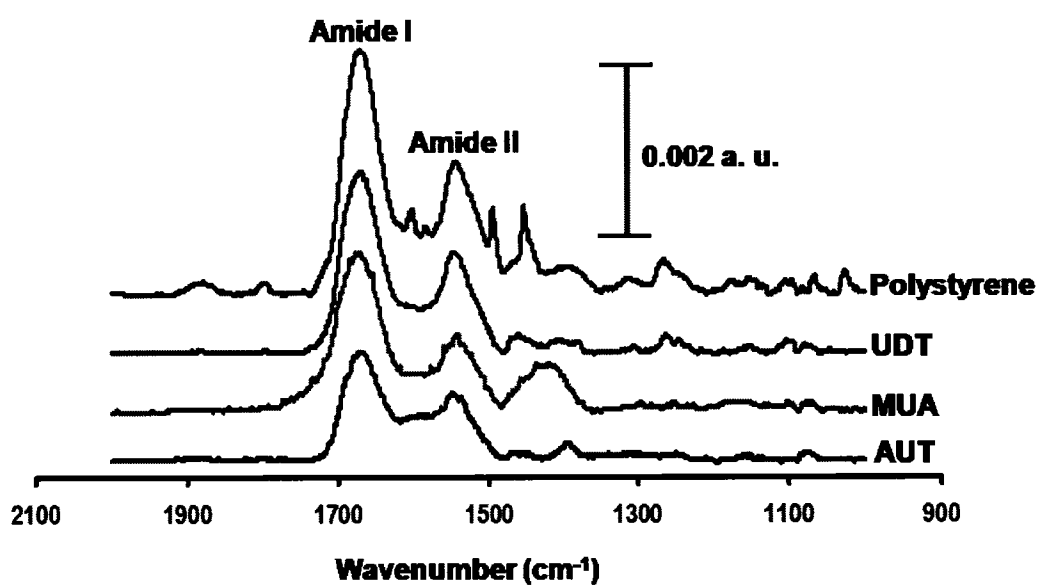


Figure 5.03. Spectra obtained following 1 h adsorption of 14.7 nM HFG onto polystyrene, UDT, MUA and AUT modified planar gold substrates. The presence of amide peaks in each spectrum indicates that HFG did adsorb to all these surfaces.

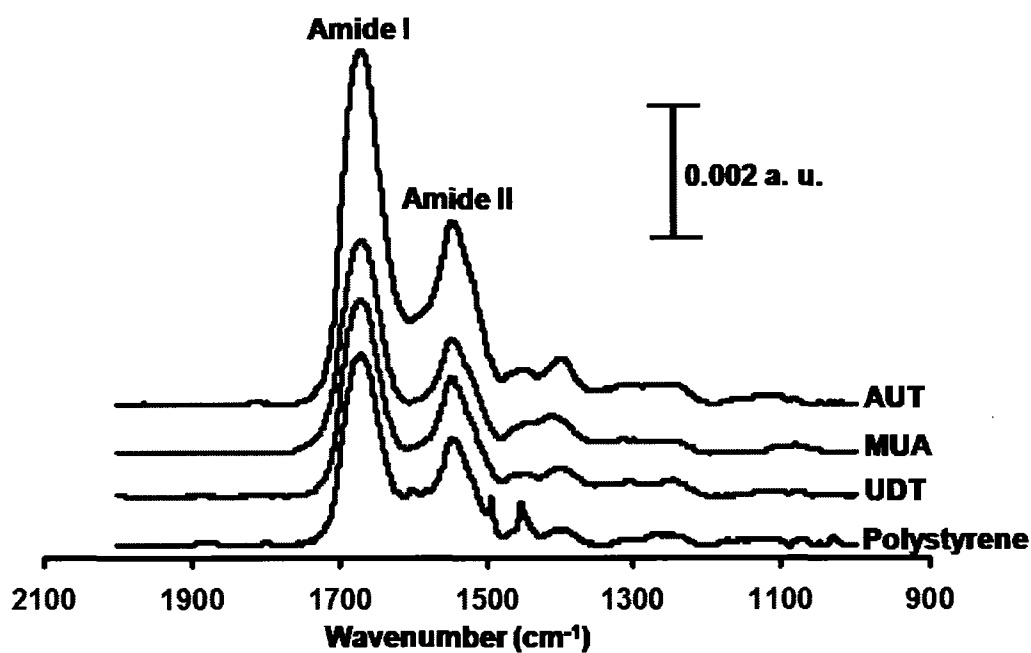


Figure 5.04. IRRAS investigation showing 1 h adsorption of 588 nM HFG on different chemistries of polystyrene, UDT, MUA and AUT modified planar gold substrates. Presence of amide bands indicates protein adsorption onto the substrates.

HFG adsorbed on	Peak Position (cm ⁻¹)			Absorbance (a.u.)	
	Amide I	Amide II 14.7 nM	Amide II 588 nM	Amide II 14.7 nM	Amide II 588 nM
Polystyrene	1669 ± 1	1543 ± 1	1545 ± 1	0.00147 ± 0.00002	0.00368 ± 0.00003
UDT	1670 ± 1	1543 ± 1	1545 ± 1	0.00121 ± 0.00001	0.00382 ± 0.00002
MUA	1670 ± 1	1543 ± 1	1545 ± 1	0.00091 ± 0.00003	0.00365 ± 0.00002
AUT	1669 ± 1	1543 ± 1	1546 ± 1	0.00080 ± 0.00001	0.00584 ± 0.00001

Table 5.2. Spectroscopic measurements of 14.7 and 588 nM concentrations of fibrinogen (HFG) adsorbed on different gold substrates which are modified with UDT, MUA and AUT self-assembled monolayers (SAMs). Adsorbed protein spectra were collected at resolution of 2 cm⁻¹. For band positions, the average value for 6 measurements is reported and the standard deviation of the average was lower than the resolution (2 cm⁻¹) of the measurement. Absorbance measurements shown are also average values and standard deviations of 6 spectral measurements.

character. As noted previously, it has been established by other groups that proteins denature to a greater extent on hydrophobic surfaces, a process that exposes interior hydrophobic groups and drives attraction between neighboring adsorbed molecules.^{4, 7, 40} These results imply that HFG adsorbs in a similar fashion on the neutral polystyrene and UDT surfaces as confirmed by their surface HFG coverage shown in Table 5.2.

In Table 5.2, a close examination of amide II peak intensities of 14.7 nM fibrinogen on MUA and AUT charged surfaces following 1 h adsorption show similar protein coverage. The amide II absorbance for the AUT modified surface is 0.00080 a.u. compared to 0.00091 a.u. for the carboxyl-terminated surface. The data indicate almost equal affinity for protein adsorption on the positively charged AUT SAM surface and its counterpart negatively-charged MUA SAM at lower solution concentrations. In addition, these values may reflect electrostatic repulsion from oppositely charged surface species at lower solution concentrations.

However, the amide II absorbance values measured on the AUT and MUA charged surfaces are lower than those recorded on both polystyrene and UDT hydrophobic surfaces. Higher quantities observed on polystyrene and UDT modified gold substrates at lower concentration might be a direct result of surface-induced conformation/orientation changes due to the high degree of protein denaturation on such surfaces. As noted previously,

denaturation serves to maximize interaction between the hydrophobic surface groups leading to greater protein coverage.^{4, 23, 26, 41}

A sharp increase in the amide II absorbance is noted in Figure 5.04 after the adsorption of a 588 nM HFG solution on AUT-derived substrate. The amide II band is linearly related to the amount of protein bound to the surface.^{23, 39} Thus, HFG adsorption on amine-modified gold substrate recorded the greatest protein surface coverage. Fibrinogen is a massive protein with regions of both negative and positive charges. The overall charge of the protein at physiological pH is -10 .⁷ Therefore, this highest observed coverage might have resulted from the electrostatic interaction between the negatively charged E and D domains of the HFG molecule with the amine substrate. This result is consistent with that reported by Evans-Nguyen *et al.* on fibrinogen adsorption amine surfaces.²⁵

Finally, Figure 5.04 comparatively illustrates the amide II peak intensities following the 588 nM HFG adsorption on polystyrene, UDT and MUA. The amide II absorbances measured on these three surfaces are not statistically different (based on t-test at the 95% confidence level) at the higher HFG concentration. This suggests that HFG has similar coverage on these surfaces. However, HFG is expected to exhibit different conformations on these surfaces with different chemistries. For systems where electrostatic interactions play an important role, the maximum adsorption will be affected by charges from both adsorbate and the

surface. Hence, the negatively charged fibrinogen molecule would experience electrostatic repulsion from the negatively charged carboxylate functionalities on the MUA substrate resulting in low protein coverage.

Desorption of Adsorbed Fibrinogen. It is expected that weaker electrostatic interaction would lead to more reversible interactions whilst hydrophobic effects would be largely responsible for irreversible protein adsorption. To ascertain this possibility, we investigated the possible fibrinogen desorption from the MUA-derived substrates using phosphate buffer at physiological pH. In order to investigate desorption and/or displacement of fibrinogen, and the influence of the underlying MUA monolayer, three sets of MUA-modified gold substrates were used. The substrates were simultaneously immersed in two sets of fibrinogen concentrations used in this study. After 1 h incubation period and thorough rinsing with PBS, three of the slides were analyzed using IRRAS. The other three slides were quickly transferred to freshly prepared 1 mM PBS solution, incubated for another 1 h and analyzed.

Figure 5.05 presents the spectra of pre-formed HFG substrates on MUA SAM before and after exposure to PBS. The positions of amide I and II bands recorded before and after 1 h exposure to PBS solution are very similar. This suggests that the adsorbed HFG is not perturbed by PBS solution. IRRAS measurements of both 14.7 and 588 nM HFG before and after incubation in PBS are given in Table 5.3. About 24% adsorbed HFG

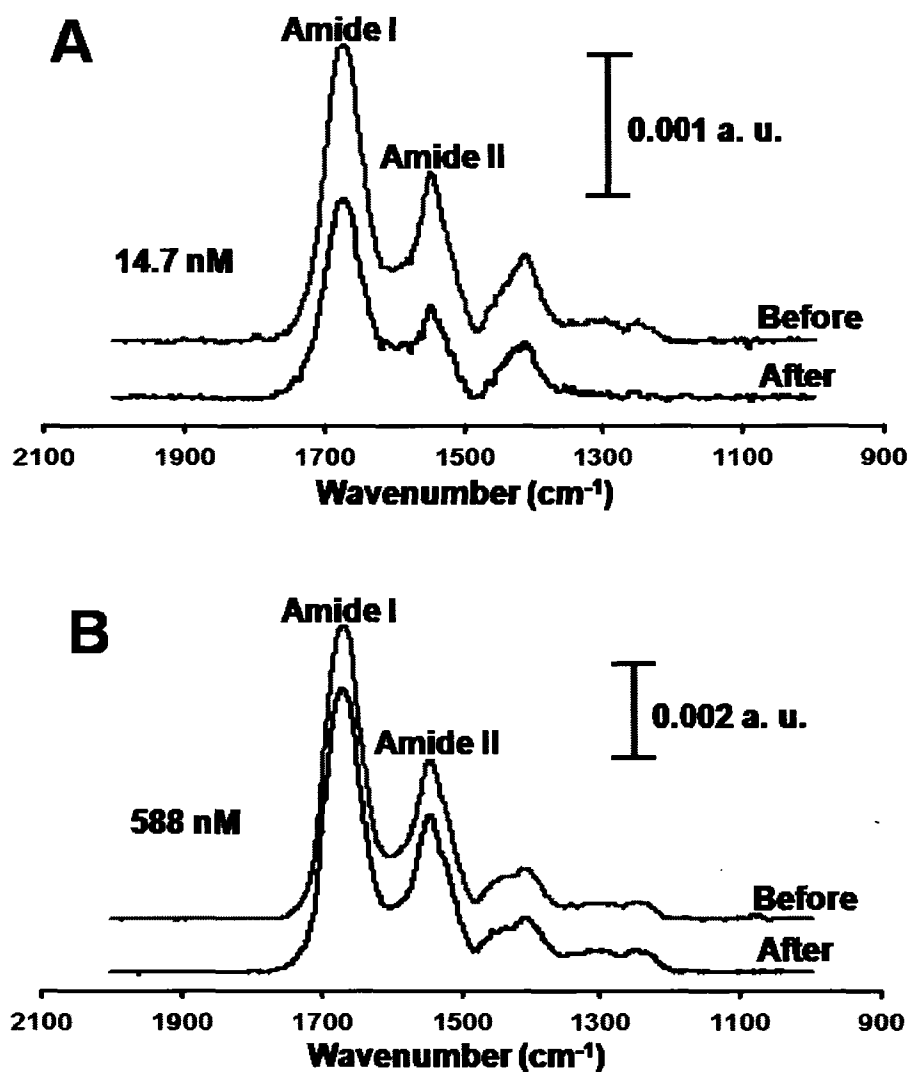


Figure 5.05. Investigation of possible desorption of HFG from MUA substrate. (A) Spectra showing adsorbed 14.7 nM HFG on MUA substrate before and after PBS displacement. (B) Before and after 588 nM HFG desorption by PBS from MUA-derived substrate.

HFG adsorbed on MUA	Peak Position (cm ⁻¹)			Absorbance (a.u.)	
	Amide I	Amide II 14.7 nM	Amide II 588 nM	Amide II 14.7 nM	Amide II 588 nM
Before PBS	1670 ± 1	1543 ± 1	1545 ± 1	0.00088 ± 0.00002	0.00367 ± 0.00001
After 1 h in PBS	1671 ± 1	1540 ± 1	1545 ± 1	0.00067 ± 0.00002	0.00324 ± 0.00001
% Change (after – before)				24	12

Table 5.3. Tabulated spectroscopic measurements for evaluation of binding strength of adsorbed 14.7 and 588 nM of fibrinogen (HFG) on MUA substrate. Amide II absorbance is a diagnostic indicator for the amount or coverage of adsorbed protein. For band positions, the average value for 3 measurements is reported and the standard deviation of the average was lower than the resolution (2 cm⁻¹) of the measurement. Absorbance measurements shown are also average values and standard deviations of 3 spectral measurements.

was displaced at lower concentration (Figure 5.05A) whereas only 12% was desorbed at higher concentration (Figure 5.05B). The significance of this result stems from a previous report which correlated the amount of fibrinogen eluted with sodium dodecyl sulfate with platelet binding.⁴² HFG that was more tightly bound to polymer surfaces exhibited a lower affinity for platelets than a loosely bound layer. Hence, since interfacial platelet aggregation is a key step in the formation of a blood clot, the biocompatibility of a surface may be influenced by how tightly it binds fibrinogen. Again, looking at the relatively small amounts of adsorbed HFG displaced, it can be deduced that there is no single interaction responsible for fibrinogen adsorption on modified substrates.

HFG Adsorption onto Pre-HFG Substrates. In the following sections, the adsorption of human fibrinogen to substrates having pre-formed HFG films will be examined. Pre-formed HFG substrates will be referred to as pre-HFG substrates. The sequential adsorption experiment will allow us to probe the effect of a pre-formed protein layer on the adsorption of subsequent HFG and examine any displacement or co-adsorption processes. According to Oscarsson, the structures of underlying substrates do not only influence the protein-covering the layer but also the adsorption characteristics and subsequent binding to other protein molecules.⁴³ Hence, the objective of this particular study is to evaluate the

influence of both SAM-modified and the pre-HFG substrates on subsequent HFG adsorption.

Figure 5.06 presents the adsorption of 588 nM HFG onto 14.7 nM pre-HFG substrates with underlying AUT, MHA and UDT self-assembled monolayers as indicated. The spectral measurements are shown in Table 5.4. Comparison between Figures 5.04 and 5.06 supply some interesting qualitative details about the state of adsorbed HFG at each functional group. First, the positions of the amide I bands of the adsorbed HFG to both SAM-modified and the pre-HFG substrates are very similar. This implies that the HFG molecule retains its conformation on the pre-HFG substrates at each functional group.

Secondly, the amount of HFG adsorbed on pre-HFG substrate with underlying methyl functionality is comparable to its counterpart recorded in Table 5.2. This might reveal the exerted influence of the underlying methyl functionality on the adsorption pattern of HFG on both substrates. Thirdly, visual inspection of the pre-HFG substrates for both MUA and AUT films seems to show differences in coverage compared those shown in Table 5.2. However, statistical analysis shows no difference in the amount of HFG coverage for the two methods. In summary, the details of the spectral analysis in this study suggest that the amount of adsorbed HFG is mainly influenced by the underlying thiol monolayer chemistry with barely any contribution from the pre-adsorbed protein film.

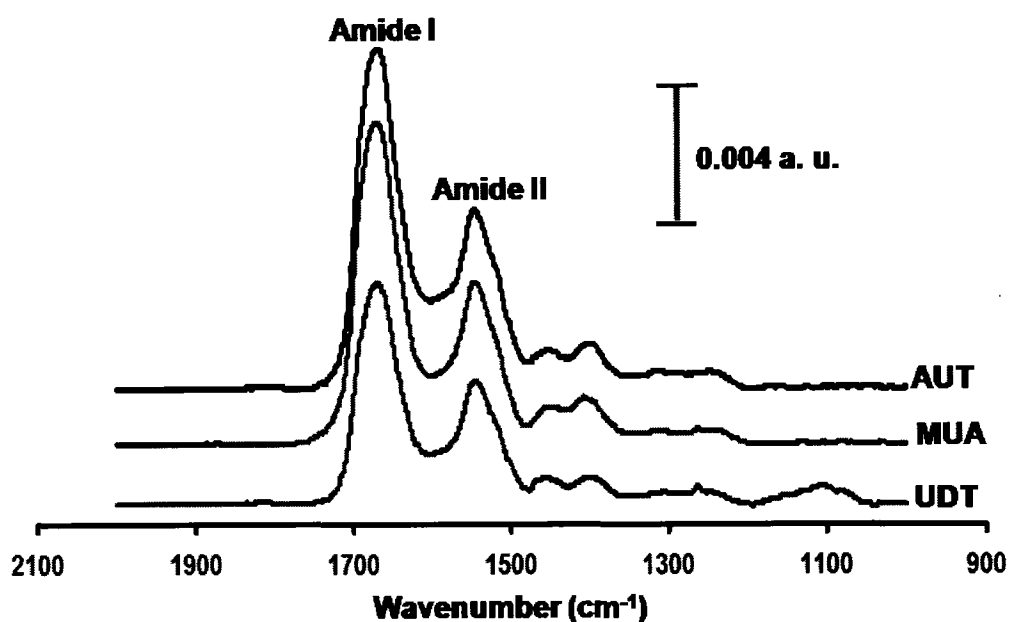


Figure 5.06. IRRAS spectra for 588 nM human fibrinogen (HFG) following 1 h adsorption time on 14.7 nM pre-HFG on planar gold substrates modified with AUT, MUA and UDT SAMs. The presence of amide peaks in each spectrum indicates that HFG did adsorb to all these surfaces.

Pre-HFG adsorbed on	Peak Position (cm⁻¹)			Absorbance (a.u.)	
	Amide I	Amide II 14.7 nM	Amide II 588 nM	Amide II 14.7 nM	Amide II 588 nM
UDT	1670 ± 1	1543 ± 1	1546 ± 1	0.00125 ± 0.00001	0.00361 ± 0.00002
MUA	1670 ± 1	1544 ± 1	1546 ± 1	0.00095 ± 0.00002	0.00464 ± 0.00001
AUT	1669 ± 2	1544 ± 1	1546 ± 1	0.00080 ± 0.00001	0.00513 ± 0.00001

Table 5.4. IRRAS measurements for 14.7 and 588 nM HFG adsorbed on the SAMs substrates with pre-formed HFG films. For band positions, the average value for 3 measurements is reported and the standard deviation of the average was lower than the resolution (2 cm⁻¹) of the measurement. Absorbance measurements shown are also average values and standard deviations of 3 spectral measurements.

Adsorption Isotherms of Fibrinogen on Modified Surfaces. The objective is to use infrared spectroscopy to model the HFG binding to different substrates. FTIR has been shown to have sufficient sensitivity to be used for studying protein adsorption in both solution and on solid support.^{20, 21, 27, 44} In the following section, the protein isotherms were constructed using substrates prepared in two different ways. The aim was to help further examine the influence of the SAM monolayer and that of the pre-formed protein film on the surface coverage of HFG.

First, single SAM modified substrate was exposed to various HFG solutions with concentrations ranging from 14.7 to 588 nM (as pre-HFG substrates). Substrates prepared this way mimic single channels that are widely employed to measure binding strengths of biological interactions.⁴⁵ The substrate was sequentially immersed in each solution for 1 h and IRRAS spectra were taken each time. The amide II bands spectral measurements on each substrate were recorded and plotted against each HFG solution concentration. Figure 5.07 shows adsorption isotherms constructed by plotting amide II absorbance for the pre-HFG substrates initially modified with UDT, MUA and AUT SAMs against various HFG solution concentrations. The binding constants of fibrinogen on the different substrates were determined by fitting the amount of HFG adsorbed (using amide II absorbance) to the range of solution concentrations using Langmuir-type equation 5.1 given below:

$$y = \frac{B_{\max} K_{\text{ads}} x}{1 + K_{\text{ads}} x} \quad (5.1)$$

where y is the amount of protein adsorbed to the modified gold substrate, B_{\max} is the adsorption capacity (maximum amount of protein adsorbed), K_{ads} is the adsorption coefficient and x is protein solution concentration. When $y = 0.5$, equation 5.1 can be solved for the solution concentration of adsorbate corresponding to half-maximal surface coverage. At this concentration, $x = K_{\text{ads}}^{-1}$, hence the value of the adsorption coefficient correspond to the inverse of the concentration at half-saturation coverage. The initial steep slopes of the plots shown in Figure 5.07 reflect high affinity of fibrinogen for the SAM-modified substrates. The amount adsorbed levels off as the adsorption sites are gradually filled.

The second approach involved the use of different SAM modified substrates for different HFG concentrations. Figure 5.08 shows adsorption isotherms constructed by plotting amide II absorbance for HFG adsorbed on UDT, MUA and AUT modified substrates against various HFG solution concentrations. The AUT-derived substrate shows a steeper slope compared to both MUA and UDT derived substrates. The fitting parameters of the HFG binding curves are given in Table 5.5. Since the adsorption phenomena appeared to follow a typical Langmuir isotherm, K_{ads} can be estimated from the binding curves. K_{ads} is a measure of the binding strength of the complex formed between the protein and the

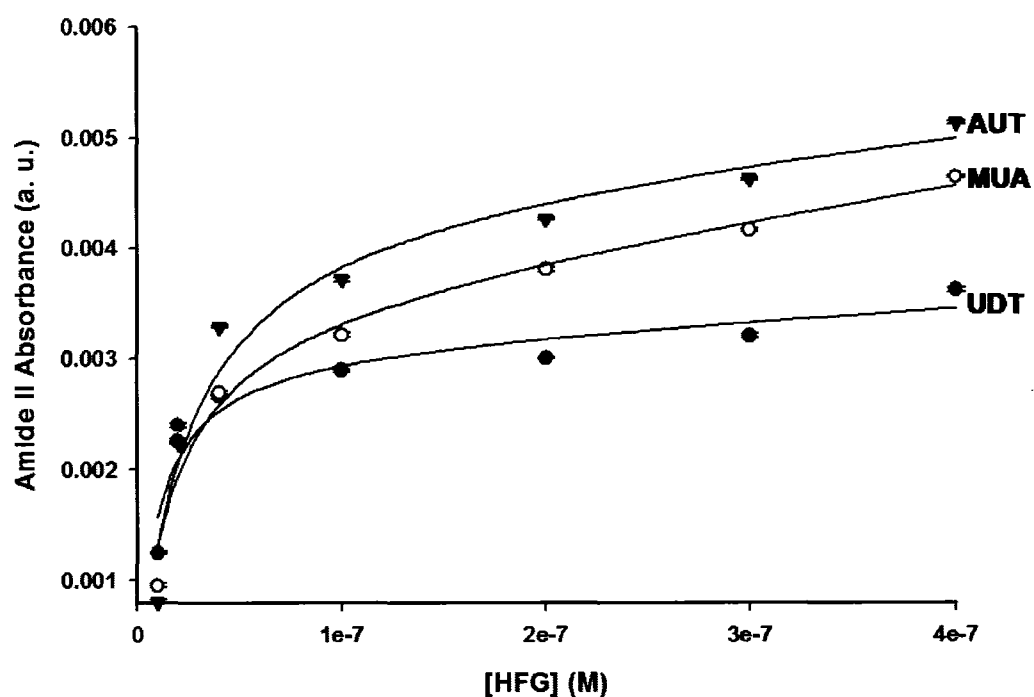


Figure 5.07. Binding curve showing HFG coverage on pre-HFG gold substrates modified with different chemistries. Amide II absorbance was used as a measure of the amount of adsorbed protein on the surface of the various self-assembled monolayers. Solution concentrations of HFG track its surface coverage. Plots indicate HFG adsorption on UDT (filled circles), MUA (open circles) and AUT (filled triangles).

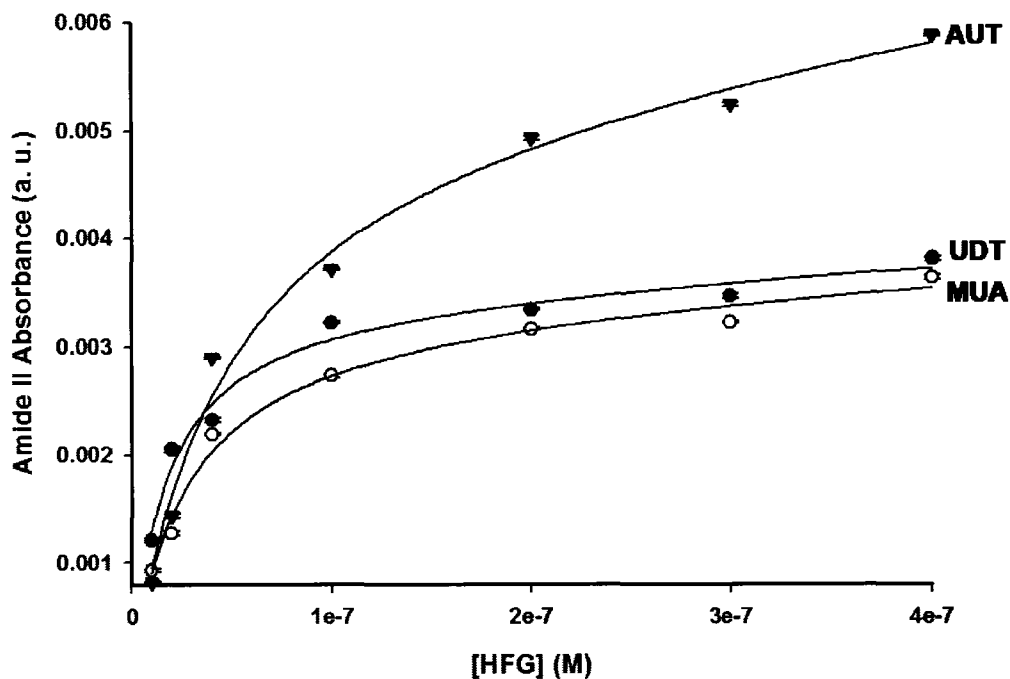


Figure 5.08. Binding curve showing HFG coverage on gold substrates modified with different chemistries. Amide II absorbance was used as a measure of the amount of adsorbed protein on the surface of the various self-assembled monolayers. Solution concentrations of HFG track its surface coverage. Plots indicate HFG adsorption on UDT (filled circles), MUA (open circles) and AUT (filled triangles).

SAM	Substrate	B_{max}	$K_{ads} (M^{-1})$	R^2
UDT	SAM modified	$3.5 (0.3) \times 10^{-3}$	$5.8 (0.24) \times 10^7$	0.98
	Pre-HFG	$3.1 (0.1) \times 10^{-3}$	$1.0 (0.22) \times 10^6$	0.95
MUA	SAM modified	$3.5 (0.2) \times 10^{-3}$	$3.6 (0.14) \times 10^7$	0.99
	Pre-HFG	$3.5 (0.2) \times 10^{-3}$	$5.7 (0.15) \times 10^7$	0.97
AUT	SAM modified	$5.3 (0.1) \times 10^{-3}$	$2.2 (0.62) \times 10^7$	0.99
	Pre-HFG	$4.5 (0.2) \times 10^{-3}$	$4.1 (0.88) \times 10^7$	0.96

Table 5.5. Curve-fitting parameters for HFG curves for both SAM-modified and the pre-HFG substrates. The SAM substrates consisted of UDT, MUA and UDT self-assembled monolayer (SAM) chemistries.

substrate. For example, a large K_{ads} value indicates that the protein has a high binding affinity for the substrate.

Three observations are noteworthy from the adsorption isotherms presented in Figures 5.07 and 5.08. First, Figure 5.07 shows better correlation coefficient (R^2) values compared to those obtained from Figure 5.08, indicating a better agreement between the fit and the data. Secondly, the adsorption capacity (B_{max}) values obtained for the fits are very similar for all the plots. This implies that the recorded amide II intensities are not solely due to surface-protein interactions but rather a combination of nonspecific adsorption and specific binding. Thirdly, K_{ads} values determined from the Langmuir fit varies with surface chemistry. All the K_{ads} values presented in Table 5.5 for both methods are very similar ($\sim 10^7 M^{-1}$), indicating that HFG has similar affinity towards all surfaces studied in this work. It must be noted that the distribution of hydrophobic and hydrophilic residues as well as charged groups on the protein surface are important determinants in protein complex formation on modified surfaces. These exposed surface functionalities predict the adsorption characteristics of the protein. As a rule, hydrophilic surfaces more weakly adsorb proteins than hydrophobic surfaces.¹ Our results do not clearly show any distinction based on K_{ads} for the different substrates. We might, in future, have to look at the affinity between immobilized anti-HFG and its HFG antigen at high HFG concentration to help address the effect of surface chemistry on

protein coverage. However, FTIR-based adsorption studies provide an interesting quantitative evaluation of fibrinogen binding SAMs functionalized gold substrates in a label-free format.

Evaluation of the Influence of Structure on Protein Coverage. A general overview of the structural differences in the three proteins studied is warranted for interpretation of their surface coverage. Lysozyme is a small (MW \approx 14 kD), rigid protein. For example, it has been demonstrated that LYS maintains its rigid native structure upon adsorption to different surfaces.⁴⁶ Bovine IgG has a Y-shaped structure with molecular weight of 150 kD. The IgG molecule is known to adopt orientations ranging between end-on and side-on and it usually adsorbs only through non-specific interaction to the amine-modified substrates.^{12, 47, 48} Fibrinogen is a very large (MW = 340 kD), dimeric protein with multiple charge making it very surface active. Given the differences in structure and the heterogeneous nature of protein surfaces generally, these proteins are expected to exhibit different adsorption characteristics on different surfaces.

Figures 5.09A and 5.09B respectively show IRRAS spectra following 1 h adsorption of 14.7 and 588 nM solutions of lysozyme (LYS), HFG and bovine IgG onto AUT modified gold substrates. Observance of amide bands in these three spectra proves that the proteins are indeed adsorbed on AUT self-assembled monolayers. Table 5.6 presents the summary of infrared spectroscopic measurements of amide bands in

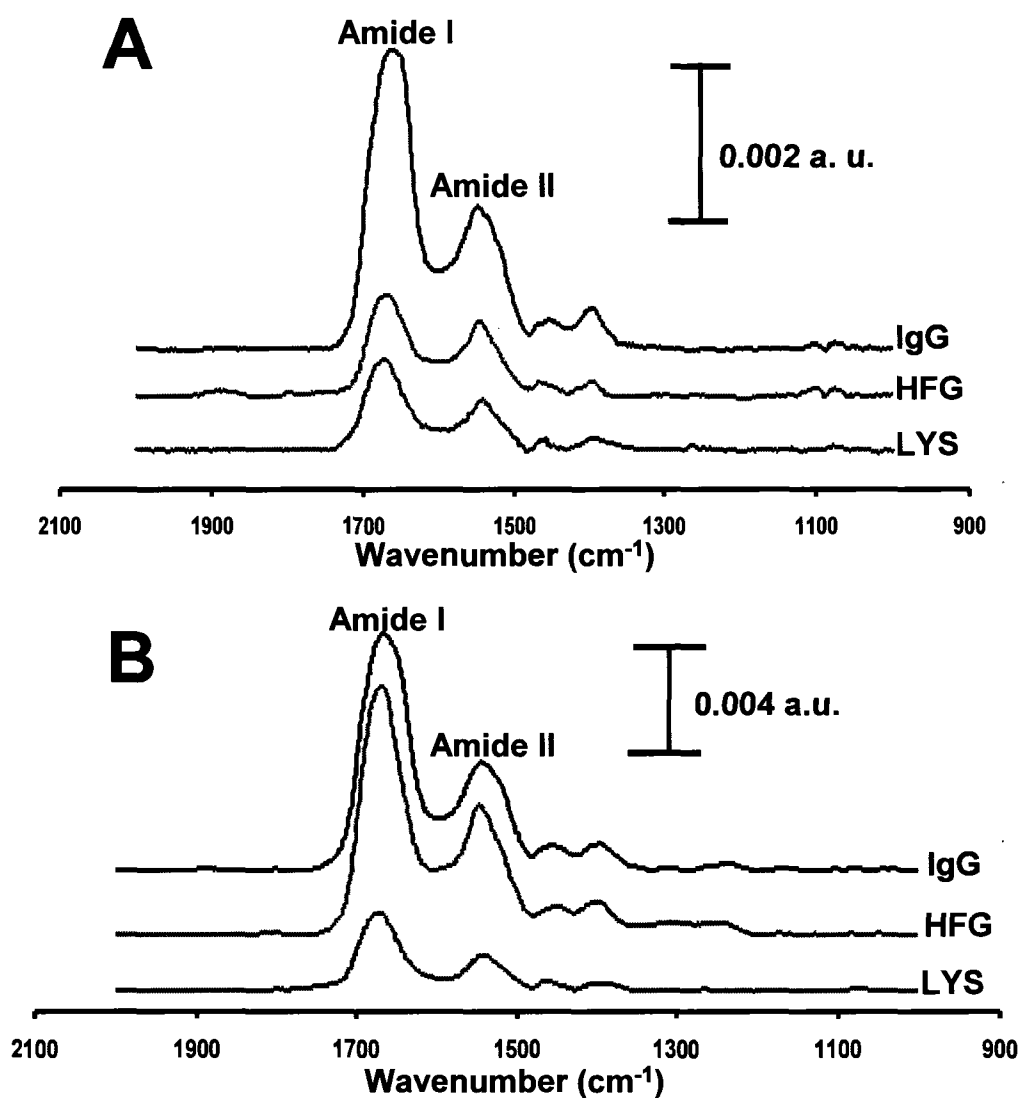


Figure 5.09. Comparison of adsorption characteristics of HFG, IgG and LYS adsorbed on AUT-patterned gold substrates. (A) IRRAS spectra of 14.7 nM LYS, HFG and blgG after 1 h exposure time. (B) Similar experiment on AUT using concentrations of 588 nM solutions of the proteins in (A).

Adsorbed Protein on NH ₂ Substrate	Peak Position (cm ⁻¹)			Absorbance (a.u.)	
	Amide I	Amide II 14.7 nM	Amide II 588 nM	Amide II 14.7 nM	Amide II 588 nM
HFG	1669 ± 2	1544 ± 1	1546 ± 1	0.00085 ± 0.00003	0.00583 ± 0.00001
Bovine IgG	1662 ± 1	1545 ± 1	1543 ± 1	0.00183 ± 0.00001	0.00434 ± 0.00001
LYS	1670 ± 2	1540 ± 1	1540 ± 1	0.00068 ± 0.00002	0.00137 ± 0.00002

Table 5.6. IRRAS measurements of the adsorption of HFG, IgG and LYS on AUT-patterned gold substrates. Amide I and amide II bands are used respectively as diagnostic indicators for conformational changes and as a measure of the amount or coverage of adsorbed proteins.

Figures 5.09A and 5.09B. There are small, but measurable, differences in both amide I and II peak positions for adsorbed proteins.

The surface coverage of the proteins for the concentrations studied is given in Table 5.6. As before, amide II absorbance was used as diagnostic for the amount of protein adsorbed on the AUT-modified gold substrates. An increase in the absorbance of the amide II band is noted for all the proteins in Figure 5.09B. This increase in the amide II intensity corresponds to an increase in the amount of protein adsorbed to the surface. Lysozyme is the smallest protein therefore recorded the lowest amide II band intensity for both concentrations. In contrast, fibrinogen showed the highest surface coverage (amide II intensity) among the three proteins by virtue of its molecular weight. The non-specifically adsorbed bovine IgG also showed substantially high surface coverage. These results suggest that, the amount of adsorbed protein to surface results from combined effects of surface chemistry, protein structure and lateral interactions between the adsorbed protein molecules.

Conclusion

The work presented in this chapter has demonstrated that FTIR is well suited for exploring the rich chemistries of alkanethiols as well as tracking the surface coverage of adsorbed proteins. Characterization of monolayers using IRRAS made it possible to examine the varied surface

chemistries employed. Polystyrene surfaces showed exposed adsorption sites after protein adsorption at both high and low concentration protein concentrations. The use of both direct SAM modified and pre-formed protein substrates provided further insight into the interaction between an adsorbed protein molecule and its solution species. In addition, Langmuir-type isotherms helped a measure of the binding strength of the adsorbed protein. Coverage of fibrinogen changed according to the surface chemistry and molecular weight of the adsorbed protein. The overall conclusion from the results presented in this chapter is that surface coverage of an adsorbed protein depends largely on the nature of the substrate and the protein structure.

References

- (1) Horbett, T. A.; Brash, J. L. In *ACS Symposium Series 343*; Horbett, T. A., Brash, J. L., Eds.; American Chemical Society, Washington, DC: Anaheim, CA, 1987; Vol. 1, pp 1-33.
- (2) Norde, W.; Fraaye, J. G. E. M.; Lyklema, J. *Acs Symposium Series 1987*, **343**, 36-47.
- (3) Norde, W.; MaCrichtie, F.; Nowicka, G.; Lyklema, J. *Journal of Colloid and Interface Science 1986*, **112**, 447-456.
- (4) Lu, D. R.; Park, K. *Journal of Colloid and Interface Science 1991*, **144**, 271-281.
- (5) Norde, W.; Giacomelli, C. E. *Macromolecular Symposia 1999*, **145**, 125-136.
- (6) Santore, M. M.; Wertz, C. F. *Langmuir 2005*, **21**, 10172-10178.

- (7) Feng, L.; Andrade, J. D. *Proteins at Interfaces II: Fundamentals and Applications*, San Diego, California, March 13-17 1995; American Chemical Society, Washington, DC; 67-79.
- (8) Roach, P.; Farrar, D.; Perry, C. C. *Journal of the American Chemical Society* **2006**, *128*, 3939-3945.
- (9) Kiaei, D.; Hoffman, A. S.; Horbett, T. A. In *Proteins at Interfaces II*, 1995; Vol. 602, pp 450-462.
- (10) Arai, T.; Norde, W. *Colloids and Surfaces* **1990**, *51*, 1-15.
- (11) Norde, W.; Haynes, C. A. *Proteins at Interfaces li* **1995**, *602*, 26-40.
- (12) Buijs, J.; vandenBerg, P. A. W.; Lichtenbelt, J. W. T.; Norde, W.; Lyklema, J. *Journal of Colloid and Interface Science* **1996**, *178*, 594-605.
- (13) Lin, J. N.; Drake, B.; Lea, A. S.; Hansma, P. K.; Andrade, J. D. *Langmuir* **1990**, *6*, 509-511.
- (14) Ta, T. C.; Sykes, M. T.; McDermott, M. T. *Langmuir* **1998**, *14*, 2435-2443.
- (15) Sit, P. S.; Marchant, R. E. *Thrombosis and Haemostasis* **1999**, *82*, 1053-1060.
- (16) Green, R. J.; Frazier, R. A.; Shakesheff, K. M.; Davies, M. C.; Roberts, C. J.; Tendler, S. J. B. *Biomaterials* **2000**, *21*, 1823-1835.
- (17) Ulman, A. *An Introduction to Ultrathin Organic Films: From Langmuir-Blogett to Self-Assembly*; Academic Press Inc.: New York, USA, 1991.
- (18) Sit, P. S.; Marchant, R. E. *Surface Science* **2001**, *491*, 421-432.
- (19) Puskas, J. E.; Dahman, Y.; Margaritis, A. *Biomacromolecules* **2004**, *5*, 1412-1421.
- (20) Tunc, S.; Maitz, M. F.; Steiner, G.; Vazquez, L.; Pham, M. T.; Salzer, R. *Colloids and Surfaces B-Biointerfaces* **2005**, *42*, 219-225.

- (21) Naidja, A.; Liu, C.; Huang, P. M. *Journal of Colloid and Interface Science* **2002**, *251*, 46-56.
- (22) Ta, T. C.; McDermott, M. T. *Analytical Chemistry* **2000**, *72*, 2627-2634.
- (23) Liedberg, B.; Ivarsson, B.; Hegg, P. O.; Lundstrom, I. *Journal of Colloid and Interface Science* **1986**, *114*, 386-397.
- (24) Marchant, R. E.; Barb, M. D.; Shainoff, J. R.; Eppell, S. J.; Wilson, D. L.; Siedlecki, C. A. *Thrombosis and Haemostasis* **1997**, *77*, 1048-1051.
- (25) Evans-Nguyen, K. M.; Tolles, L. R.; Gorkun, O. V.; Lord, S. T.; Schoenfisch, M. H. *Biochemistry* **2005**, *44*, 15561-15568.
- (26) Wertz, C. F.; Santore, M. M. *Langmuir* **2002**, *18*, 706-715.
- (27) Cheng, S. S.; Chittur, K. K.; Sukenik, C. N.; Culp, L. A.; Lewandowska, K. *Journal of Colloid and Interface Science* **1994**, *162*, 135-143.
- (28) Wertz, C. F.; Santore, M. M. *Langmuir* **1999**, *15*, 8884-8894.
- (29) Nsiah, F. MSc., University of Alberta, Edmonton, 2003.
- (30) Bohnert, J. L.; Horbett, T. A. *Journal of Colloid and Interface Science* **1986**, *111*, 363-378.
- (31) Servagent-Noinville, S.; Revault, M.; Quiquampoix, H.; Baron, M. H. *Journal of Colloid and Interface Science* **2000**, *221*, 273-283.
- (32) Porter, M. D.; Bright, T. B.; Allara, D. L.; Chidsey, C. E. D. *Journal of the American Chemical Society* **1987**, *109*, 3559-3568.
- (33) Snyder, R. G.; Maroncelli, M.; Strauss, H. L.; Hallmark, V. M. *Journal of Physical Chemistry* **1986**, *90*, 5623-5630.
- (34) Maroncelli, M.; Qi, S. P.; Strauss, H. L.; Snyder, R. G. *Journal of the American Chemical Society* **1982**, *104*, 6237-6247.
- (35) Pei, Z.; Busenlehner, L.; Worley, S. D.; Tang, Y.; Curtis, C. W. *Journal of Physical Chemistry B* **1997**, *101*, 10450-10454.

- (36) Liedberg, B.; Ivarsson, B.; Lundstrom, I.; Salaneck, W. R. *Progress in Colloid and Polymer Science* **1985**, *70*, 67-75.
- (37) Liedberg, B.; Ivarsson, B.; Lundstrom, I. *Journal of Biochemical and Biophysical Methods* **1984**, *9*, 233-243.
- (38) Barbucci, R.; Magnani, A. *Biomaterials* **1994**, *15*, 955-962.
- (39) Giacomelli, C. E.; Bremer, M. G. E. G.; Norde, W. *Journal of Colloid and Interface Science* **1999**, *220*, 13-23.
- (40) Prime, K. L.; Whitesides, G. M. *Science* **1991**, *252*, 1164-1167.
- (41) Horbett, T. A.; Brash, J. L. *Acs Symposium Series* **1987**, *343*, 1-33.
- (42) Kiaei, D.; Hoffman, A. S.; Horbett, T. A.; Lew, K. R. *Journal of Biomedical Materials Research* **1995**, *29*, 729-739.
- (43) Oscarsson, S. *Journal of Colloid and Interface Science* **1994**, *165*, 402-410.
- (44) Imamura, K.; Kawasaki, Y.; Awadzu, T.; Sakiyama, T.; Nakanishi, K. *Journal of Colloid and Interface Science* **2003**, *267*, 294-301.
- (45) Rich, R. L.; Myszka, D. G. *Journal of Molecular Recognition* **2003**, *16*, 351-382.
- (46) Su, T. J.; Green, R. J.; Wang, Y.; Murphy, E. F.; Lu, J. R.; Ivkov, R.; Satija, S. K. *Langmuir* **2000**, *16*, 4999-5007.
- (47) Buijs, J.; Lichtenbelt, J. W. T.; Norde, W.; Lyklema, J. *Colloids and Surfaces B-Biointerfaces* **1995**, *5*, 11-23.
- (48) Chen, S. F.; Liu, L. Y.; Zhou, J.; Jiang, S. Y. *Langmuir* **2003**, *19*, 2859-2864.

CHAPTER VI

CONCLUSIONS AND FUTURE WORKS

Overall Conclusions

The overall research objectives as set forth in Chapter I of this thesis were aimed at developing modified gold nanoparticle patterns and then using surface enhanced Raman spectroscopy (SERS) as a probing technique. In addition, it was set out to also examine the adsorption characteristics of proteins, mainly the influence of surface chemistry on the protein-protein interaction and their surface coverage, on modified gold nanoparticles and planar substrates. We believe that the work presented in the preceding Chapters have demonstrated that SERS and infrared reflection absorption spectroscopy (IRRAS) are powerful diagnostic techniques for monitoring protein adsorption characteristics at interfaces.

In Chapter II, the surface enhancement afforded by coupling metal nanoparticles to the extrinsic 4-mercaptobenzoic acid (4-MBA) Raman label was utilized to develop arrays of nanoparticle patterns. The MBANP patterning procedure employed relies on the use of microfluidic channels created in PDMS. The bifunctionality of the 4-MBA molecule helps to examine its interaction with different functional groups on the surface. SAMs of alkanethiols on gold substrate with the same chain length but different terminal functionalities were studied. Raman mapping helped to

provide spectral differences in the patterns. Mapping analysis was explored to reveal the potential application of SERS as a qualitative tool and for multicolor imaging. In effect, protocols developed in Chapter II provided the platform for SERS-based microarrays applications presented in Chapters III and IV.

Work presented in Chapter III demonstrated for the first time the fabrication of SERS-based protein microarrays. Development of simple microfluidic patterning methods and synthesis of nanoparticle labeling (DSNB) made the fabrication and reading of protein microarrays possible. The fabrication procedure utilized potentially produced 100 protein arrays indicating the enormous capabilities of our fabrication procedure. Selectivity in the array was governed by antigen-antibody interactions. Moreover, SERS signal intensities were found to be consistent with the DSNB reporter density which was investigated in Chapter IV. Quantitative analysis in the SERS-based protein microarray system was performed using SEM particle analysis.

Controlling both the reporter and surface antibody densities using mixed self-assembled monolayers (SAMs) provided the ability to optimize the assay platform (Chapter IV). The mixed SAMs were formed from thiolates consisting of one thiolate that covalently binds antibody to the nanoparticle and the other thiolate that resists protein adsorption. The results showed that the number of immobilized antibody increased with

increasing DSNB reporter density. Again, the increased SERS signal resulted mainly from multivalent antigen-antibody interactions and partly from hot spots.

Chapter V described the use of infrared reflection absorption spectroscopy (IRRAS) as a powerful quantitative diagnostic tool for analysis of the protein surface coverage on patterned SAMs. Surfaces examined had varied surface functionalities which helped to probe protein adsorption characteristics. Surface-induced effect on protein immobilization provided insight into both coverage and conformation/orientation of adsorbed proteins. IRRAS analysis revealed differences in the adsorbed state of fibrinogen based on underlying SAM chemistry.

Suggestions for Future Work

Recent advances in Raman instrumentation coupled with narrow, well-resolved SERS bands that allow simultaneous sensitive detection of multiple analytes make SERS a technique of choice for trace biological analysis and identification.¹⁻⁵ Methodologies developed in this study open the door to other applications such as sandwich SERS-based immunoassays. The effect of a larger particle size than the one used in this thesis on SERS signal can be explored in such assay format to draw a correlation between SERS signal and particle size. Using a particle size of

about 80 nm would produce a red shift to match the near-infrared (NIR) laser line of 785 nm used in the SERS experiments presented in this thesis. In addition, incorporation of different biomolecules assay into the sandwich immunoassay would be potentially useful for drug development.

Another area of investigation that can be explored on our array is the multiplexed detection of different protein targets with different Raman-labeled nanoparticle probes. Since our array can potentially create 100 different spots, 10 different antibodies can be easily patterned on an amine-modified gold substrate. The immobilized antibodies probes on the substrate will then be exposed to solutions containing different protein targets covalently linked to gold nanoparticles via dissimilar Raman-active labeling. SERS detection of the Raman-active labels would reveal the identity of each antibody probe. With this technique, multiplexed detection can be used to create bar-codes or biomarkers for the identification of pathogens and other biomedical applications. Specific interactions envisaged in this proposed method will help circumvent the irreproducibility in SERS. A similar idea has been explored by Mirkin and co-workers for the scanometric DNA detection.¹ Their method was limited to only one single-stranded DNA probe.

Currently, work underway in our lab is exploring detection of DNA aptamers on various nanofabricated structures. As an interesting extension of the work presented in this thesis, the aim is to develop both labeled and

label-free SERS detection of short-chain DNA molecules. The label-free SERS detection is designed to use substrates fabricated through the glancing-angle deposition (GLAD) method. The excellent properties of the GLAD substrates such as high porosity, tunability and robustness make them better alternative to the traditional electrochemically roughened SERS substrates.⁶ They are also designed to produce strong electromagnetic enhancement which is dependent on size, shape and nanoscale roughness of the substrate material. The labeled-SERS approach seeks to employ DNA aptamers instead of antibodies discussed in this thesis.

Overall, the two major vibrational techniques, SERS and IRRAS, employed in this dissertation have many advantages in bioanalytical applications. For example, SERS is capable of providing much more information about the molecular structure and the local environment in condensed phases than an electronic spectroscopy technique, such as fluorescence.

References

- (1) Cao, Y. W. C.; Jin, R. C.; Mirkin, C. A. *Science* **2002**, *297*, 1536-1540.
- (2) Grubisha, D. S.; Lipert, R. J.; Park, H. Y.; Driskell, J.; Porter, M. D. *Analytical Chemistry* **2003**, *75*, 5936-5943.

- (3) Driskell, J. D.; Kwart, K. M.; Lipert, R. J.; Porter, M. D.; Neill, J. D.; Ridpath, J. F. *Analytical Chemistry* **2005**, *77*, 6147-6154.
- (4) Park, H. Y.; Driskell, J. D.; Kwart, K. M.; Lipert, R. J.; Porter, M. D.; Schoen, C.; Neill, J. D.; Ridpath, J. F. *Surface-Enhanced Raman Scattering: Physics and Applications* **2006**, *103*, 427-446.
- (5) Vo-Dinh, T.; Stokes, D. L.; Griffin, G. D.; Volkan, M.; Kim, U. J.; Simon, M. I. *Journal of Raman Spectroscopy* **1999**, *30*, 785-793.
- (6) Seto, M.; Westra, K.; Brett, M. *Journal of Materials Chemistry* **2002**, *12*, 2348-2351.